uOttawa

Estimation of the Impacts of Climate Change on the Design, Risk and Performance of Urban Water Infrastructure

Fahad Alzahrani

Thesis submitted to the University of Ottawa
in partial Fulfillment of the requirements for the
Doctor of Philosophy

Civil Engineering
Faculty of Engineering
University of Ottawa

AUTHOR'S DECLARATION

I hereby declare that I am the sole author of this thesis. This is a true copy of the thesis, including any required final revisions, as accepted by my examiners.

I understand that my thesis may be made electronically available to the public.

Abstract

Changes in the temporal variability of precipitation at all timescales are expected due to global warming. Such changes affect urban water infrastructure by potentially influencing their performance and risk of failure. Unfortunately, there is considerable uncertainty about how hydrological variables will change in the future. While uncertainty is present at all timescales, the climate signal in the daily time series simulated by climate models, for instance, can be estimated with much greater certainty than in the simulated hourly time series. That is problematic as sub-daily precipitation time series are essential to solving specific water resource engineering problems, especially in urban hydrology, where times of concentrations are typically less than a day. For instance, hourly or sub-hourly precipitation time series are routinely used to design stormwater and road drainage systems. Rainfall variability at sub-daily time steps is often represented as Intensity-Duration-Frequency (IDF) curves, relating precipitation duration (of basin time of concentration) to return period and average precipitation intensity. Naturally, several researchers investigated the integration of climate change in IDF curves, leading to methods of variable complexity and variable performance.

This thesis aims to a) make a critical analysis of the most commonly used methods for IDF curves under climate change in Canada and b) identify the methods with optimal performance for a set of stations located in the South Nation watershed in Ottawa, Ontario, and c) perform a case study highlighting the effect of the choice of the temporal disaggregation method on the estimated risk of failure/performance of an urban water system.

The first part of the thesis examines Equidistant Quantile Mapping (EQM) used in the IDF_CC tool developed for the Canadian Water Network project. Two conceptual flaws in the method that led to a systematic underestimation of extreme events were discovered. Two corrections are proposed to the EQM, leading to the development of two new methods for IDF generation. The output of EQM and its improved version is a time series of annual maximum precipitation intensity for different durations that can be used to derive IDF curves.

These time series generated using the above approach are not appropriate for rainfall-runoff models for which continuous time series of precipitation (not only maximums) are required. The second part of the thesis tackles the issue, which examines a different approach to evaluating the risk of failure/performance of urban water systems under a changing climate. This second approach yields continuous time series of precipitation that can be fed in rainfall-runoff models used for IDF curve generation. The proposed method is applied in three steps:

i) projections of future daily precipitation are generated by downscaling the output of climate models; ii) the downscaled daily precipitation time series are temporally disaggregated to an hourly time step using various techniques; iii) finally, the disaggregated future precipitation time series are used as inputs to rainfall-runoff models or used to generate IDF curves. This approach relaxes several strong assumptions made to develop the EQM approach, such as the implicit (and strong) assumption that the annual maximum precipitation at two different time steps occurs during the same event. That assumption is not necessarily valid and can affect the realism of the generated IDF curves. The method's performance is obviously dependent on the temporal disaggregation technique used in step 3. In this thesis, a simple steady-state stochastic disaggregation model that generates wet/dry day occurrence using a binomial distribution and precipitation intensity using an exponential distribution is proposed and compared to widely used temporal disaggregation methods: the multiplicative random cascade model (MRC), the Hurst-Kolmogorov process (HKP), and three versions of the K-nearest neighbor model (KNN) using the nonparametric Kolmogorov-
Smirnov (KS) test. The six disaggregation techniques were assessed at four stations located in South Nation River Watershed located in Eastern Ontario, Canada.

The third part of the thesis is a case study of the impact of climate change on stormwater management. First, a stormwater management model (SWMM) of St. Catharines, Ontario, developed in a previous study, was selected to simulate its stormwater and sanitary system. The model was forced with downscaled and temporally disaggregated precipitation outputs of the Canadian Regional Climate Model at the Port Dalhousie station, simulated under emission scenario RCP8.5. The temporal disaggregation was done using the Fahad-Ousmane and the KNN (30) methods developed in the previous chapter. The impact of climate change on the frequency, volume, and quality of combined sewer overflows and other hydraulic parameters is examined. Results suggest an increase in the total volume, flow frequency percentage, maximum flow, and average flow in the stormwater system due to climate change. Therefore, adaptation measures should be implemented for the distribution network and wastewater treatment plant to convey and treat the wastewater resulting from wet and dry events.

Acknowledgments

All praises and thanks are for Allah, the Creator, and Lord of the Heavens and the Earth. “Indeed! He has power over all things.”

It has been a privilege to work closely with my supervisor, Dr. Ousmane Seidou; I have thoroughly enjoyed knowing and learning from him. I have gained much from all the knowledge, wisdom, and perspective that Dr. Seidou has taught me. I would also like to thank the committee members, Dr. Colin Rennie, Dr. Fateh Chebana, Dr. Majid Mohammadian, and Dr. Duminda Perera, for their constructive input and guidance.

Ahlam, my lovely wife, is the friend, philosopher, and guide who is always with me in all my ups and downs. At the very least, I must mention her dedication, sacrifices, and love, without which everything is meaningless. Thank you for your limitless supply of hugs to my three children, Ghosoun, Albatoul, and Abdulaziz. You always remind me of what is essential and teach me what life is all about. Also, I would not have accomplished this and many other goals without the guidance, unlimited support, and continuous encouragement from my beautiful parents, Saeed and Shamsah. I owe them a profound debt of gratitude. I will do my best to make them proud and try hard to meet their high expectations. Many thanks go to my brothers and sisters for their unlimited support, encouragement, and prayers.

Finally, I am grateful to my friends, Dr. Abdullah Aseri, Dr. Abdullah Aljanah, Dr. Hasan Alfaifi, Dr. Abdullah Alodah, Mr. Saeed Alharthi, and Mr. Hamza Alghamdi, and many others for their endless support throughout my journey.

Dedication

This thesis is dedicated to my father's soul. I hope you can see your son's Ph.D. success.

Table of Contents

Chapter 1. Introduction 1
1.1 Background 1
1.2 Problem statement 4
1.3 Thesis objectives 5
1.3.1 Specific goals 5
1.4 Thesis organization 6
1.5 Peer-reviewed Publications 7
1.6 References 9
Chapter 2 . Literature Review 11
2.1 Intensity-duration-frequency curves 11
2.2 The use of scale invariance in intensity-duration-frequency curve generation methods 14
2.3 Climate change impacts on the hydrological cycle 16
2.4 Climate models 17
2.5 Downscaling/bias correction 19
2.5.1 The Delta-change method 20
2.5.2 Multiple linear regression downscaling 20
2.5.3 Quantile mapping (QM) 21
2.5.4 Equidistant quantile mapping 22
2.6 Intensity-duration-frequency curves under climate change 25
2.6.1 IDF generation using the delta-change method 25
2.6.2 IDF curve generation using quantile mapping 27
2.7 Temporal disaggregation techniques 27
2.7.1 Uniform disaggregation models 27
2.7.2 The k-nearest neighbour disaggregation method 28
2.7.3 Random cascade disaggregation models 30
2.7.4 Hurst-Kolmogorov downscaling model 34
2.8 Conclusion 36
2.9 References 37
Chapter 3 . Assessment and Improvement of IDF Generation Algorithms Used in IDF_CC Tool 44
3.1 Abstract: 44
3.2 Introduction 45
3.3 Materials and Methods 48
3.3.1 Watershed and Data Description 48
3.3.2 Original IDF_CC algorithms 49
3.3.3 Definitions and notations 49
3.3.4 Flaws in the original EQM IDF_CC algorithm 50
3.3.5 Flaws in the QDM method 51
3.4 Improvements of IDF_CC algorithms 52
3.4.1 Improvements to the EQM method 52
3.4.2 Improvement to the QDM algorithm 53
3.5 Assessment of model performance 53

3.5.1 Sensitivity to future climate signal 54
3.5.2 Split-sample calibration and validation 54
3.5.3 Assessing the coherence between IDF generation methods 55
3.6 Results and Discussion 55
3.6.1 Comparison of the original and improved EQM method 55
3.6.2 Split-sample calibration and validation results 57
3.6.3 Coherence of the distributions of the downscaled annual maxima between downscaling methods 59
3.6.4 Comparison of IDF curves generated using different methods 60
3.7 Discussion 62
3.8 Conclusions 63
3.9 References 65
Chapter 4 . Assessing the Performance of Daily to Sub-Daily Temporal Disaggregation Methods for IDF Curves Generation under Climate Change 69
4.1 Abstract 69
4.2 Introduction 70
4.3 Materials and methodologies 73
4.3.1 General methodology 73
4.3.2 Study area and available data 75
4.3.3 Downscaling RCM outputs at the daily timescale 76
4.3.4 Temporal disaggregation techniques 77
4.3.5 Estimation of intensity-duration-frequency (IDF) curves 89
4.4 Model performance measure 89
4.4.1 The two-sample Kolmogorov-Smirnov test 89
4.5 Results 90
4.5.1 Comparison of the simulated and observed time series of each temporal downscaling method 91
4.5.2 Comparison of generated IDF curves using each temporal stochastic downscaling method 94
4.6 Discussion 96
4.7 Conclusion 101
4.8 References 103
Chapter 5 . Climate Change impact on a Municipal Water System with Combined Sewers. Case study of Port Dalhousie, Ontario, Canada 105
5.1 Abstract 105
5.2 Graphical Abstract: 106
5.1 Introduction 107
5.2 Material and methods 110
5.2.1 Study area 110
5.2.2 Wastewater treatment plant overview and overflows statistics 111
5.2.3 Data collection 112

5.2.4 Methodology ... 113
5.2.5 SWMM model development ... 115
5.2.6 RCM outputs downscaling ... 117
5.2.7 Temporal disaggregation techniques ... 118
5.3 Results ... 121
5.3.1 Validation of the simulated hourly time series ... 121
5.3.2 Water Quality Modelling ... 122
5.3.3 SWMM Model validation ... 124
5.3.4 SWMM Model performance under historical and future climate scenario ... 124
5.4 Discussion ... 129
5.5 Conclusions ... 130
5.6 References ... 132
Chapter 6 Conclusions and Recommendations ... 135
6.1 Conclusions ... 135
6.2 Recommendations ... 139
Appendix A ... 153
Appendix B ... 166

List of Figures

Figure 1.1 Major components of the thesis.. 7
Figure 2.1 The concept used in climate models (source: NOAA).. 18
Figure 3.1 Unsuccessful fit of the original equation proposed by Schardong *et al.* (2020) (Eq. S11) using quantiles of precipitation simulated with CanESM2.CanRCM4 and quantiles of observation............ 52
Figure 3.2 Differences between EQM_o and EQM_m at Russell station for the 1h precipitation datasets using scenario RCP 8.5 to force different climate models: A) GFDLESM2M RCM4, B) CanESM2 CanRCM4, C) EC-EARTH RCA4, and D) EC-EARTH HIRHAM5. 56
Figure 3.3 Evaluation of the effect of multiplying GCM (RCP 8.5) outputs for the future period at Russell station by 1.5 using: A) 1hr datasets and EC-EARTH HIRHAM5, B) 24hr datasets and EC-EARTH HIRHAM5, C) 1hr datasets and CanESM2 CanRCM, and D) 24hr datasets and CanESM2 CanRCM. 57
Figure 3.4 IDF curves generated for the period 2071-2100 at Russel station using model EC-EARTH HIRHAM 5 RCP8.5 and return periods of A) T=2years, B) T=5years, C) T=50years, and D) T=100years. 61
Figure 4.1 Flowchart of methodology. 74
Figure 4.2 The meteorological gauges in the South Nation watershed (Alodah and Seidou, 2019).... 75
Figure 4.3 A sketch of the disaggregation model steps at the level of k)Lombardo *et al.,* 2012). 80
Figure 4.4 Grouped boxplot for all disaggregation methods and different RCMs in the historical period using a) 1-hr precipitation data, and b) 24-hr precipitation data. The horizontal solid black lines represent the 25th and 75th percentiles while the horizontal solid red line represents the 50th percentile of the observed data. The dashed lines represent the whiskers (extended to the most extreme data points not considered outliers) of the observed data. The outliers are shown as '+' marker symbol.............. 94
Figure 4.5 IDF curves of Russel Station resulting from KNN30 and FO disaggregation methods, historical period (all climate models); for return periods T=2, 5, 50 and 100 years. 95
Figure 4.6 Grouped boxplot for KNN(30) and FO disaggregation methods and different RCMs in the future periods using a) 1-hr precipitation data in the short-term period, and b) 1-hr precipitation data in the medium-term period and c) 1-hr precipitation data in the long-term period. f) 24-hr precipitation data in the short-term period, and e) 24-hr precipitation data in the medium-term period, and d)24-hr precipitation data in the long-term period. The horizontal solid black lines represent the 25th and 75th percentiles while the horizontal solid red line represents the 50th percentile of the observed data. The dashed lines represent the whiskers (extended to the most extreme data points not considered outliers) of the observed data. The outliers are shown as '+' marker symbol.. 99
Figure 4.7. IDF curves of Russel Station curves resulting from KNN30 and FO disaggregation methods, long period (all climate models); for return periods T=2, 5, 50 and 100 years. 100
Figure 4.8 IDF curves at the Russel station for all disaggregation methods using different RCMs in the historical period for return period 2, 5, 50 and 100 years.. 101
Figure 5.1 Port Dalhousie wastewater treatment plant 110
Figure 5.2 Flowchart of the methodology.. 114
Figure 5.3 Representation of the network and catchments in SWMM.. 117

List of Tables

Table 3.1 Results of the two-sample Kolmogorov-Smirnov test for different models and precipitation 58
Table 3.2 Percentage of similarity between observed and downscaled AMP, calibration, and validation periods. 59
Table 3.3 Percentage of similarity between downscaled annual maxima for all periods. 62
Table 4.1 Weather station information. 76
Table 4.2 List of regional climate models used in the study. 76
Table 4.3 Descriptive statistics of observed and disaggregated hourly time series of Russell station. .92
Table 4.4 Percentage of similarity between observed and downscaled AMP in the calibration (Cal.) and validation (Val.) periods across all climate change models. 93
Table 4.5 Summary of results 97
Table 5.1 Influent characteristics of municipal wastewater treated by the WWTP. 111
Table 5.2 ECA effluent requirements of the PDWWTP (Water Environment Association of Ontario, 2020). 112
Table 5.3 Results of Calibration and validation of temporal disaggregation models. 121
Table 5.4 Initial effluent values for water quality modelling, commercial and residential development (Tavakol-Davani, 2016). 123
Table 5.5 Initial buildup values of effluent for water quality modelling commercial and residential development (Tavakol-Davani, 2016). 123
Table 5.6 Initial washoff values of effluent for water quality modelling, commercial and residential development(Tavakol-Davani, 2016). 123
Table 5.7 Summary of effluent discharge at Outfall Loading under historical climate scenario of each temporal downscaling model KNN(5, 15 and 30) and (FO). 126
Table 5.8 Summary of effluent discharge at Outfall Loading under historical and future climate scenarios, ...127
Table 5.9 Summary of effluent discharge at Outfall Loading under Historical and Future climate scenarios, KNN (5, 15 and 30) and FO models. 128
Table 5.10 water quality changes the percentage. 129

Chapter 1. Introduction

1.1 Background

There is broad consensus in the scientific community about the reality of human-induced global climate change. The Intergovernmental Panel on Climate Change (IPCC, 2007, 2015, 2022) has found that variations in temperature extremes can be partially attributed to increased carbon dioxide concentration in atmospheric layers. Industrial activities cause an increase in carbon dioxide concentration in the atmosphere, which traps the sun's radiation close to the Earth's surface and creates a hotter and more turbulent atmosphere. The increased energy in the atmosphere leads to extreme weather conditions such as floods, droughts, and heatwaves. Studies have found an increase in global mean temperatures of 0.3 °C to 0.6 °C in the last century and 0.2 °C to 0.3 °C through the previous four decades (Adamwoski *et al.,* 2010; Nicholls *et al.,* 1996). Zhang et al. (2000) and Nicholls et al. (1996) detected increases in the range of 0.5 °C to 1.5 °C in the annual average temperature over Canada.

Researchers have also observed significant warming in the spring and summer seasons in Canada's west, whereas Canada's northeast has experienced cooling (Adamwoski *et al.,* 2010). As the mean temperature and greenhouse gas emissions increase, hydrological variables such as precipitation are modified. Sun *et al.,* (2007) found that extreme precipitation is likely influenced by climate change and that wet regions might become moister while arid regions might become drier in the future. In Canada's northern areas, the total annual rainfall has changed (Zhang *et al*., 2000). Other studies have found similar increases in precipitation depth throughout the USA and Canada (Guttman *et al.,* 1992; Karl & Knight, 1998; Douville *et al*., 2002; Peterson *et al.,* 2008). In its fifth edition of the Assessment Report (AR5), the Intergovernmental Panel on

Climate Change examined the global extreme annual precipitation using emission scenarios and found that some areas, such as the northern hemisphere, have experienced heavy precipitation since 1950 (IPCC, 2015). The report also warns that increasing global mean temperature above 1.5 °C will substantially impact hydrological regimes worldwide. While the change in precipitation patterns is a certainty, many details about high spatial and temporal precipitation variations remain uncertain. For instance, rainfall intensity under climate change might increase in Europe even though seasonal summer rain might decrease (Christensen & Christensen, 2003; Khon et al., 2007; Kyselý et al., 2012).

Given that precipitation intensity is a design parameter for stormwater drainage systems, the safety of such systems in the future is at stake. Numerous researchers have examined the impacts of climate change on precipitation at scales ranging from decades to minutes. For instance, researchers have concluded that increasing daily precipitation has been observed in the Northern Hemisphere in mid-and high-latitudes for decades (Mekis & Hogg, 1999; Zhang et al., 2000; Groisman & Rankova, 2001; Alexander et al., 2006; Subash et al., 2011; Wang et al., 2013; Kuo et al., 2015; Simonovic, 2017; Schardong et al., 2020; Uruba et al., 2019). However, it is more common to find a study dealing with timescales that are larger than a day as the output of global climate models is usually provided at a daily time step.

The most common method of representing extreme precipitation for municipal infrastructure design is through intensity-duration-frequency (IDF) curves. IDF curves represent a mathematical relationship between precipitation intensity, return period, and event duration. Commonly utilized in hydrologic, hydraulic, and water resource systems, IDF curves are obtained through frequency analysis of observed precipitation time series. Many studies over the last decades have been conducted to estimate the impacts of global warming on IDF curves (Rodriguez et al., 2014, Kuo et al., 2015; Dore, 2005; IPCC, 2007, 2013). Rodriguez et al. (2014) applied the change factor method to determine the impact of climate change on extreme rainfall values in Barcelona, Spain. They assumed that the same change factor applies to all timescales, which is not necessarily realistic. IDF curves are sometimes generated using climate change projections at a daily time step generated using either climate model outputs or weather generators. The projected time series is then disaggregated at a sub-daily time step before generating IDF curves. For instance, Predrag and Simonovic (2009) and Soliman (2011) used the nearest neighbour disaggregation model to convert the output of a weather generator model from a daily time step to an hourly time step. The hourly time series was then used to generate IDF curves. De Paola et al. (2014) used the random cascade model to obtain hourly time series under climate change in Africa, which were then converted to IDF curves. Ganguli and Coulibaly (2019) applied a multiplicative random cascade model to the outputs of the fourth generation of the Canadian Regional Climate Model (CanRCM4) driven by the second generation of the Canadian Earth System Model (CanESM2) to assess the changes in future IDF curves of Southern Ontario. They used the Mann-Kendall test to detect the changes in the IDF curves. Kuo et al. (2015) used the Pennsylvania State University/National Center for Atmospheric Research numerical model regional climate model driven by four global circulation models to estimate the changes in IDF curves in central Alberta, Canada. They found that the intensity in IDF curves will likely increase due to climate change.

One of Canada's most widely used IDF generation methods in the recent years is the Equidistant Quantile Mapping (EQM) method proposed by Srivastav et al. (2014). In the EQM method, a statistical relationship or transfer function is fitted between precipitation quantiles calculated from climate models' outputs and quantiles of observed sub-daily precipitation time series. These relationships are applied to precipitation time series generated by climate models to create time series of sub-daily precipitation quantiles. The EQM is the basis of a program called the Computerized Tool for the Development of Intensity-Duration-Frequency Curves under a Changing Climate (IDF_CC tool), available online at https://www. idf-cc-uwo.ca. The EQM is highly cited in the literature, and several practitioners and researchers have used the program. The EQM was later replaced by the quantile delta method (QDM) in the IDF_CC tool. A close examination of the EQM and QDM methodologies led to the discovery of multiple issues that may lead to underestimating sub-daily extreme precipitation in the future. These flaws are likely to affect the design of municipal infrastructures, leaving municipalities vulnerable to climate change. Therefore, it is vital to investigate these flaws and either develop fixes or propose better methods for IDF generation. This endeavour is critical to the resilience of infrastructures which are the backbone of economic prosperity.

1.2 Problem statement

Climate change is a certainty, yet there is considerable uncertainty about how sub-daily precipitation intensities will change in the future. Various methods have been put forward in the literature and are being used in operational hydrology, often yielding different projections and leading to different adaptation decisions. For instance, in Canada, the IDF_CC tool is being used by several local Canadian municipalities, while its core algorithm has changed from EQM (Srivastav *et al.* 2014; Simonovic 2017) to QDM (Schardong *et al.* 2020). A critical analysis of these two methods and the development of potentially better methods for IDF generation under climate change are needed.

1.3 Thesis objectives

The main objectives of this thesis are to critically analyze different IDF generation methods and propose a simpler disaggregation method for IDF generation under climate change with an application case study on a local urban stormwater drainage system. Two approaches are investigated: 1) fixing the flaws in methods used by the IDF_CC tool and 2) generating climate change projections at a daily timescale and disaggregating the result at an hourly timescale. Various temporal disaggregation algorithms are considered, and their performances are assessed. The methods that were found to perform best are used to analyze the impact of climate change on the performance of the stormwater system of the city of St-Catharines, Ontario, Canada.

1.3.1 Specific goals

The specific goals of this thesis are to:

- Review and improve the equidistant quantile mapping (EQM) and quantile delta mapping (QDM) techniques proposed by Srivastav *et al.,* (2014) and Schardong *et al.,* (2020), respectively.
- Examine the performance of various temporal disaggregation methods applied to downscaled daily precipitation time series.
- Propose an improved IDF generation method based on the first two specific objectives.
- Evaluate the performance of temporal disaggregation methods for sub-daily precipitation time series under climate change.
- Implement the best disaggregation technique to generate hourly precipitation projections at the Port Dalhousie station in St. Catharines, Ontario.

- Use the projected precipitation time series to estimate the projected change in peak discharge and outfall loading volume in a changing climate conditions in the city's stormwater system.

1.4 Thesis organization

The thesis consists of six chapters, as illustrated in Figure 1.1. A list of under review works is provided at the end of this chapter and organized as follows: Chapter 1 introduces the topic, outlines the main objectives, and presents the thesis structure. Chapter 2 includes a literature review of related studies, including the work done to date. Chapters 3, 4, and 5 are written in paper format, each containing an introduction, materials, methodology, results, discussion, and conclusion. Chapter 3, titled "*Assessment and Improvement of IDF Generation Algorithms Used in IDF_CC Tool,*" discusses the EQM methods and proposes two improvements. Chapter 4, titled "*Assessing the Performance of Daily to Sub-Daily Temporal Disaggregation Methods for IDF Curves Generation under Climate Change*," introduces the Fahad-Ousmane model, a novel model for temporal downscaling of daily time series. The FO method is compared to alternative stochastic disaggregation models such as the k-nearest neighbours model, the Hurst-Kolmogorov model, and the multiplicative random cascade model. Chapter 5 is a case study titled "*Climate Change impact on a Municipal Water System with Combined Sewers. Case study of Port Dalhousie, Ontario, Canada.*" Finally, Chapter 6 provides a conclusion and recommendations for future work.

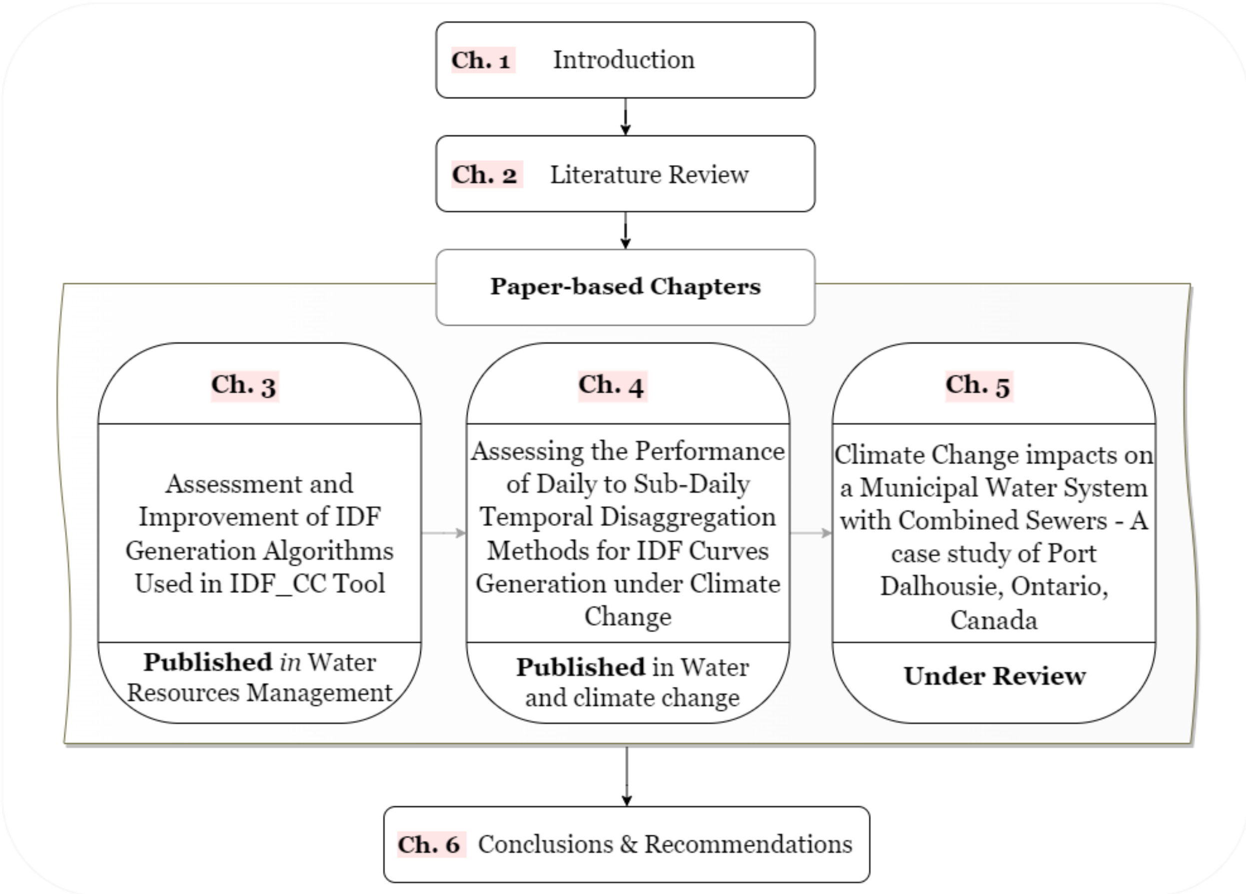

Figure 1.1 Major components of the thesis.

1.5 Peer-reviewed Publications

The following is a list of works prepared by the author during his Ph.D.:

- Alzharani, F., Seidou, O., & Alodah, A. (2022). Assessment and Improvement of IDF Generation Algorithms Used in IDF_CC Tool. Water Resources Management, published.
- Alzharani, F., Seidou, O., & Alodah, A. (2023). Assessing the Performance of Daily to Sub-Daily Temporal Disaggregation Methods for IDF Curves Generation under Climate Change.
- Alzharani, F., Seidou, O., & Alodah, A. (under review). Climate Change impact on a Municipal Water System with Combined Sewers. Case study of Port

Dalhousie, Ontario, Canada. Stochastic environmental research and risk assessment.

1.6 References

Adamowski, J., Adamowski, K., & Bougadis, J. (2010). Influence of trend on short duration design storms. *Water Resources Management*, *24*(3), 401–413.

Alexander, L. V., Zhang, X., Peterson, T. C., Caesar, J., Gleason, B., Klein Tank, A., Haylock, M., Collins, D., Trewin, B., & Rahimzadeh, F. (2006). Global observed changes in daily climate extremes of temperature and precipitation. *Journal of Geophysical Research: Atmospheres*, *111*(D5).

Christensen, J. H., & Christensen, O. B. (2003). Severe summertime flooding in Europe. *Nature*, *421*(6925), 805–806.

De Paola, F., Giugni, M., Topa, M. E., & Bucchignani, E. (2014). Intensity-Duration-Frequency (IDF) rainfall curves, for data series and climate projection in African cities. *SpringerPlus*, *3*(1), 1–18.

Dore, M. H. (2005). Climate change and changes in global precipitation patterns: What do we know? *Environment International*, *31*(8), 1167–1181.

Douville, H., Chauvin, F., Planton, S., Royer, J.-F., Salas-Melia, D., & Tyteca, S. (2002). Sensitivity of the hydrological cycle to increasing amounts of greenhouse gases and aerosols. *Climate Dynamics*, *20*(1), 45–68.

Ganguli, P., & Coulibaly, P. (2019). Assessment of future changes in intensity-duration-frequency curves for Southern Ontario using North American (NA)-CORDEX models with nonstationary methods. *Journal of Hydrology: Regional Studies*, *22*, 100587. https://doi.org/10.1016/j.ejrh.2018.12.007

Groisman, P. Y., & Rankova, E. Y. (2001). Precipitation trends over the Russian permafrost-free zone: Removing the artifacts of pre-processing. *International Journal of Climatology: A Journal of the Royal Meteorological Society*, *21*(6), 657–678.

Guttman, N., Wallis, J., & Hosking, J. (1992). *Regional temporal trends of precipitation quantiles in the US*. IBM Thomas J. Watson Research Division.

IPCC., A. S. (2007). Climate change 2007: Synthesis report. *Summary Fo r Policymakers*.

Karl, T. R., & Knight, R. W. (1998). Secular trends of precipitation amount, frequency, and intensity in the United States. *Bulletin of the American Meteorological Society*, *79*(2), 231–242.

Khon, V. C., Mokhov, I., Roeckner, E., & Semenov, V. (2007). Regional changes of precipitation characteristics in Northern Eurasia from simulations with global climate model. *Global and Planetary Change*, *57*(1–2), 118–123.

Kuo, C.-C., Gan, T. Y., & Gizaw, M. (2015). Potential impact of climate change on intensity duration frequency curves of central Alberta. *Climatic Change*, *130*(2), 115–129. https://doi.org/10.1007/s10584-015-1347-9

Kyselý, J., Beguería, S., Beranová, R., Gaál, L., & López-Moreno, J. I. (2012). Different patterns of climate change scenarios for short-term and multi-day precipitation extremes in the Mediterranean. *Global and Planetary Change*, *98*, 63–72.

Mekis, E., & Hogg, W. D. (1999). Rehabilitation and analysis of Canadian daily precipitation time series. *Atmosphere-Ocean*, *37*(1), 53–85.

Nicholls, N., Gruza, G., Jouzel, J., Karl, T., Ogallo, L., & Parker, D. (1996). *Observed climate variability and change*. Cambridge University Press Cambridge.

Peterson, T. C., Zhang, X., Brunet-India, M., & Vázquez-Aguirre, J. L. (2008). Changes in North American extremes derived from daily weather data. *Journal of Geophysical Research: Atmospheres*, *113*(D7).

Rodríguez, R., Navarro, X., Casas, M. C., Ribalaygua, J., Russo, B., Pouget, L., & Redaño, A. (2014). Influence of climate change on IDF curves for the metropolitan area of Barcelona (Spain). *International Journal of Climatology*, *34*(3), 643–654.

Schardong, A., Simonovic, S. P., Gaur, A., & Sandink, D. (2020). Web-Based Tool for the Development of Intensity Duration Frequency Curves under Changing Climate at Gauged and Ungauged Locations. *Water*, *12*(5). https://doi.org/10.3390/w12051243

Simonovic, S. P. (2009). *Updated rainfall intensity duration frequency curves for the City of London under the changing climate*.

Simonovic, S. P. (2017). Bringing future climatic change into water resources management practice today. *Water Resources Management*, *31*(10), 2933–2950.

Solaiman, T. A. (2011). *Uncertainty estimation of extreme precipitations under climate change: A non-parametric approach*. The University of Western Ontario (Canada).

Srivastav, R. K., Schardong, A., & Simonovic, S. P. (2014). Equidistance Quantile Matching Method for Updating IDFCurves under Climate Change. *Water Resources Management*, *28*(9), 2539–2562. https://doi.org/10.1007/s11269-014-0626-y

Stocker, T., & Qin, D. (Eds.). (2013). *Climate change 2013: The physical science basis: summary for policymakers, a report of working group I of the IPCC: technical summary, a report accepted by working group I of the IPCC but not approved in detail: and frequently asked questions: part of the working group I contribution to the fifth assessment report of the intergovernmental panel on climate change*. WMO, UNEP.

Subash, N., Singh, S., & Priya, N. (2011). Extreme rainfall indices and its impact on rice productivity—A case study over sub-humid climatic environment. *Agricultural Water Management*, *98*(9), 1373–1387.

Sun, Y., Solomon, S., Dai, A., & Portmann, R. W. (2007). How often will it rain? *Journal of Climate*, *20*(19), 4801–4818.

Wang, D., Hagen, S. C., & Alizad, K. (2013). Climate change impact and uncertainty analysis of extreme rainfall events in the Apalachicola River basin, Florida. *Journal of Hydrology*, *480*, 125–135. https://doi.org/10.1016/j.jhydrol.2012.12.015

Zhang, X., Vincent, L. A., Hogg, W., & Niitsoo, A. (2000). Temperature and precipitation trends in Canada during the 20th century. Atmosphere-Ocean, 38(3), 395–429.

Chapter 2. Literature Review

2.1 Intensity-duration-frequency curves

Intensity-duration-frequency curves (IDF) represent the mathematical relationship between precipitation intensity, return period, and event duration. Commonly utilized in hydrologic, hydraulic, and water resource systems, IDF curves are obtained through frequency analysis of observed precipitation time series. The increase of severe rainfall events at the daily scale has been widely studied, but less attention has been given to sub-daily scales. Recent studies on IDF curves have focused on generating the best fitting distribution and sampling techniques under climate change (e.g., Al-Amri and Subyani, 2017; Alzahrani, 2013; Elsebaie, 2012; Subyani and Al-Amri, 2015). According to multiple research such as Elsebaie (2012), Kuo *et el*., (2015), and Martel *et al*., (2021) found that the extreme rainfall scaling may rise as a length function with shorter-duration, while longer-return-period events expected to have the most significant rainfall increases in warmer environments.

Some gaps have been found in the relationship between extreme precipitation events and climate change, such as the resolution of climate models or detection of the climate change signal. Martel *et al*., (2021) have discussed some of these scientific gaps and provided technical advice, namely the climate change adaptation plan, to adjust IDF curves and increase climate resilience. Most studies seek alternative statistical downscaling methods by generating IDF curves rather than finding the best goodness-of-fit for distribution. For example, Ragno et al. (2018), Hurad *et al*., (2010), Cheng *et al*., (2014) and Mélèse *et al*., (2018) applied Bayesian analysis as a framework to estimate the uncertainty in IDF curves under climate change scenarios. They found that the uncertainty increases in the future climate period. Svensson *et al*., (2007) compared techniques for estimating IDF curves from fragmented data for Eskdalemuir, Scotland, and suggested using monthly maxima to estimate the return period while allowing up to 20% of missing data in each month. Although over a decade has passed since the publication of the article by Svensson *et al*., (2007), estimation of the IDF values has been conducted through hourly time series range 1970-1986 and investigating alternative techniques for curve creation. Studies on generating IDF curves that incorporate climate change are somehow scarce. Nguyen *et al*., (2007a, b) proposed a spatial-temporal downscaling approach that relies on scale invariance to generate future climate IDF relationships by employing output from two GCMs (HadCM3 A2 and CGCM2 A2). Temporal scaling was done for extreme value distribution variables based on historical rainfall distribution. The study revealed significant variations between these models in future IDF.

Prodanovic and Simonovic (2007) used a KNN-based weather generator to generate IDF curves for current and future climates for the city of London, Ontario. They found that the future rainfall generated from the wet (CCSRNIES B21) scenario predicted a 30% increase in rainfall magnitude for various durations and return periods. Simonovic and Peck (2009) developed IDF information under a wet climate change scenario using all available rainfall data for various periods. The maximum 24-hour precipitation events breaching the calendar-day limit were recreated using a moving window method. According to their research, IDF for the 2050s will alter by 10.7% to 34.9%. Coulibaly and Shi (2005) developed IDF curves for the Grand River and Kenora Rainy River basins in Ontario using the results from the CGCM2 B2 model. For all stations of relevance in the 2050s and 2080s, their analysis revealed a 24-35% increase in rainfall intensity for 24-hour and sub-daily periods. Chandra *et al*., (2015) estimated the uncertainty deriving from distribution parameters fitted to data and various GCM models. The posterior distribution of parameters is calculated using a Bayesian method. Scale invariance theory is used to derive short-term return levels from daily data. The uncertainty in short-term rainfall return levels is significant compared to longer periods.

Regional climate models (RCM) have been used as a tool to simulate localized IDF curves in a changing climate. The resolution of projected data is essential for further studies, as it is applied to determine any influence of climate variations. For instance, Mailhot *et al*., (2006) implemented RCMs to estimate IDF values over Quebec province by using regional frequency analysis. Their results showed a decrease of approximately 50% for durations of 2h and 6h and a decrease of 32% for durations of 12h and 24h, but the study is limited because the resolution scale of the grid box needs to be improved by using estimate points. Schardong *et al*., (2020), Srivastav *et al*., (2014), and Silva *et al*., (2021) generated IDF curves under climate change projection using climate model data of scenarios RCP 2.6, 4.5, and 8.5. The results found an increase in extreme events in each climate scenario. The IDF curves were also very sensitive to different climate models. These studies used the same global circulation model (GCM) resolution posted in the NA-CORDEX portal.

The limitations of the RCM resolution data are crucial to the projected time series. To obtain IDF values from hourly rainfall data, Onof and Arnbjeg-Nielsen (2009) utilized an hourly weather generator technique with disaggregation. For the 2050s, hourly data was gathered from the RCM A2 scenario with 10 km x 10 km resolution. The study's drawback is the stationarity assumption, which states that the ratio of area-to-point estimations will remain constant regardless of climatic change. A wide range of techniques has been used to generate IDF under climate change, among which i) the Delta-Change method (DC), ii) quantile-based algorithms such as equidistant quantile mapping (EQM) algorithm and quantile delta mapping (QDM) algorithm (e.g., Kuo *et al*., 2015; Switzman *et al*., 2017; Şen & Kahya, 2021), iii) techniques based on the temporal disaggregation of projected daily precipitation (Mirhosseini *et al*., 2014; Uraba *et al*., 2019; Wang *et al*., 2013) and finally iv) those based on the scale invariance theory (Innocenti *et al*., 2017; Langousis and Veneziano, 2007; Veneziano and Furcolo, 2002).

2.2 The use of scale invariance in intensity-duration-frequency curve generation methods

The multifractal analysis is an excellent approach for analyzing and modelling data series with substantial spatiotemporal variability, particularly regarding the phenomenon's non-uniform properties. It gives synthetic modelling of the variability of the processes under consideration. It introduces the notion of scale invariance, the relationship between a measurement and its scale (Bernardara *et al.*, 2007). The approach is applied to determine the data behaviour behind the observed data. The multifractal approach introduces scale invariance to detect the relationship between measurements and scales. According to Bougadis and Adamowski (2006), scale invariance is developed and used to create scaling IDF curves for disaggregation (or downscaling) of rainfall intensity from low to high resolution. These curves are created for gauged sites using the generalized extreme value (GEV) scaling and the Gumbel probability distribution. Furthermore, they discovered that the scaling technique is more efficient and produces more accurate estimates when compared to the total observed precipitation at all sites.

The multifractal approach is defined as follows: "a stationary multifractal measure is singular of order γ on a fractal set whose fractal dimension D (γ) depends on γ" (Frisch and Parisi, 1980). When the temporal precipitation is under multifractal theory, and the data statistics are unchanged, then the precipitation is multiplied by the positive random variable *Ar* (Langousis *et al.*, 2007). The introductory classes of random measures call the multifractal analysis to represent the rainfall extremes, and the singularity exponent γ at point *t* is absent.

The main objective of the scale invariance theory is to build a link between GCM and RCM data series and observed data (Nguyen, 2020). Scale-invariant fractal mathematics has been introduced and applied to various contexts. This concept, scale-inertia, is used to quantitatively characterize the link between annual maximum precipitations (AMPs) over different durations (Burlando and Rosso, 1996; Marta *et al.*, 2009; Menabde *et al.*, 1999;

Nguyen *et al.*, 2002). Prodanovic and Simonovic (2007) and Solaiman and Simonovic (2011) have also applied scaling-invariance to measure the similarity between the mean vector and mean of selected neighbours. This step is called Mahalanobis distance measurement. Then, the weight is generated based on the smallest distance to multiply the daily data series.

The scale invariance theory is generally applied in water resources engineering, especially in estimating annual extreme precipitation frequency. The theoretical finding of IDF estimation was beneficial in estimating IDF values using multifractal theory (Innocenti *et al.*, 2017; Langousis and Veneziano, 2007; Veneziano and Furcolo, 2002). The scaling invariance theory reduces the complexity of the Monte Carlo simulation. In other words, based on this theory, the estimation of IDF is straightforward (Langousis and Veneziano, 2007). When scaling is applied, the geographic and climatic features are also valid in the IDF estimation (Langousis *et al.*, 2013; Langousis and Veneziano, 2007).

Temporal downscaling scaling invariance is applied widely to estimate GEV distribution parameters. Furthermore, estimating the GEV parameters depends on non-central moments of probability weight moments. Proposed models in recent literature include the generalized extreme value distribution (GEV)/ non-central moments model (NCM) model (Nguyen *et al.*, 2007; Vu *et al.*, 2017) and GUM/PWM model (Nguyen and Nguyen, 2018; Nguyen, 2020; Yu *et al.*, 2004). The multiplicative cascade model considers scaling theory for disaggregating the data series from a daily scale to a sub-daily scale (Sunyer *et al.*, 2015; Soltani *et al.*, 2020). Olssen (1998) applied scale invariance to the random cascade model. Orsmbee (1989) applied the theory in numerous deterministic disaggregation models. The scale invariance theory is also applied to stochastic disaggregation models (Margulis and Entekhabi, 2001). Finally, scale invariance is utilized in the KNN disaggregation model (Chandra *et al.*, 2015).

2.3 Climate change impacts on the hydrological cycle

Precipitation results from a long series of physical processes that begin with the evaporation of water into the air as water vapour. This water vapour condenses by binding to nucleation sites (such as dust particles and aerosols) as an air parcel rises to form clouds from which rainfall eventually falls under gravity (Trenberth *et al.*, 2003). Depending on the many processes that contribute to the condensation of atmospheric water vapour, three types of precipitation can be generated (Trenberth *et al.*, 2003; Poujol *et al.*, 2020; Poujol *et al.,* 2021). First, orographic rainfall occurs when air is pushed to ascend due to the presence of a mountain. This causes water condensation by adiabatic cooling, resulting in clouds and periodic rainfall on the windward side of the mountain (Roe, 2005). Second, stratiform rainfall is caused by the ascent of huge air masses caused by weather fronts. Stratiform rainfall is frequently linked with long-distance moving meteorological systems that provide lengthy moderate showers over broad regions (Houze, 1997). Third, convective precipitation is generated by the rapid ascent of a local air mass in a conditionally unstable environment induced by local differential heating. This results in cumulonimbus clouds that deliver brief and locally heavy rains, occasionally in the form of hail (Houze, 1997). Recently, a method for separating these three forms of rainfall in climate model simulations was presented (Poujol *et al.*, 2020). Many studies contend that the hydrological cycle will continue accelerating due to global warming (Huntington, 2006; Trenberth, 2011); however, this theory is controversial (Koutsoyiannis, 2020). A greater volume of water vapour in the atmosphere in a future warmer world could increase the three forms of rainfall (Trenberth *et al.*, 2003). Convective rainfall, which is responsible for the majority of sub-daily rainfall extremes, is predicted to rise the most, according to a process in which fewer (but larger) storms producing higher rainfall events may occur in a warmer future (Dai *et al.,* 2020). Several studies have anticipated the future evolution of the continental hydrological cycle in France (Boé *et al.*, 2009, Chauveau *et al.*, 2013). These studies were developed using the previous generation of global climate models (GCMs) from the Coupled Model Intercomparison Project Phases 3 and 5 (CMIP3, Meehl *et al.*, 2007) and emission scenarios. These studies usually agree on a decline in river flows, which is noticeable in the summer and fall seasons. Some research on individual catchments has provided a more detailed description of the changes and associated uncertainty (Chauveau *et al.*, 2013; Hattermann *et al.*, 2017; Donnelly *et al.*, 2017; Habets *et al.*, 2013a; Lafaysse and Hingray, 2014). The studies on the impacts of climate change on the hydrological cycle are still ongoing aIPCC approves the novel climate models. For instance, CMIP 5 models' outputs have been applied in many studies and applications using different weather data sets or patterns.

2.4 Climate models

Climate change is defined as significant changes in global temperature, precipitation, wind patterns, and other measures of climate that occur over several decades or longer (typically 30 years). It is caused by various natural and anthropogenic factors, including volcanic eruptions, variation in the Earth's rotation axis inclination, variation in the Earth's orbit around the sun, and an increase in greenhouse gases such as CO_2 resulting from natural processes and human activities. Climate change is expected to significantly affect the regime of all hydroclimatic variables, including precipitation. Climate change primarily impacts water resources' security, demand, and management. Several studies have found a relationship between climate change and water resources (Coulibaly and Shi, 2005; Nguyen, 2020; Schardong *et al.*, 2020; Schardong and P Simonovic, 2019; Solaiman and Simonovic, 2011; Switzman *et al.*, 2017; Willems, 2013).

Climate models are created to help meteorologists and hydrologists solve complex cases and interpret the potential changes in climate phenomena; moreover, such models allow meteorologists and hydrologists to examine theories and solutions comprehensively. Using climate change models promotes a strong understanding of the potential climate variation over a long future period. Models would also be beneficial in establishing climate adaptation plans to mitigate the possible adverse effects of climate impacts (NOAA, https://www.climate.gov/maps-data/primer/climate-models).

The mechanism of climate models is based on several physical processes and built on a well-documented basis. Using climate models aims to mimic the transfer of energy and material through the climate system. Therefore, climate models are defined by global circulation. Climate models are a mathematical representation of the Earth's climate system built by physical laws and theories such as the conservation of mass, energy, and momentum. Climate models split the Earth's surface into atmosphere and ocean on three-dimensional grids. Finer spatial scales are used to model many physical processes such as precipitation, as seen in Figure 2.1. Climate models can then simulate the warming effect resulting from prescribed concentrations of greenhouse gases; thus, they are widely used to simulate the relationship between human choices, emissions, concentrations, and temperature changes.

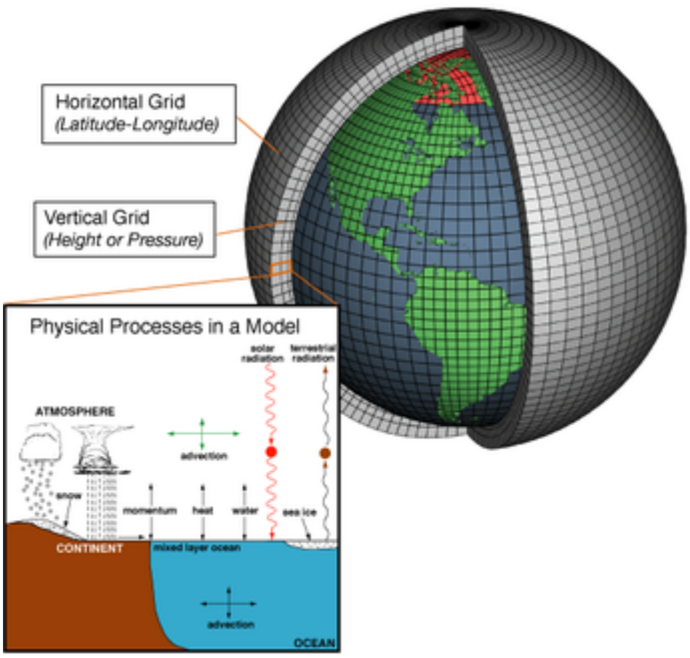

Figure 2.1 The concept used in climate models (source: NOAA).

Climate change model data such as global (GCM) and regional (RCM) are essential for the hydrological model to evaluate the vulnerability of climate variables to climate change conditions (Semenov and Bengtsson, 2002). The daily values of the precipitation variable have been extracted from the North American Domain of Coordinated Regional Climate Downscaling Experiment (NA-CORDEX), and they are driven by the Global Circulation Model (GCM) as part of the Coupled Model Inter-comparison Project Phase 5 (CMIP 5). The World Climate Research Program has introduced the CORDEX project, which predicts climate change regionally at a satisfactory level. The NA-CORDEX database is built especially for the North American continent, and the database has all climate variables modelled by different global climate change models and regional climate models for RCPs 2.6, 4.5, and 8.5. NA-CORDEX database has been used in many studies of climate change vulnerability in the water resources management sector. NA-CORDEX's resolution is essential because it influences the spatial downscaling of climate grid data. GCM resolution has been discussed in many studies, which have determined the possible limitations that could be addressed in further studies. Since climate change has garnered global interest in different sectors, many GCMs have been developed to link the impacts of greenhouse gas emissions to present and future periods with global and regional scales.

2.5 Downscaling/bias correction

Downscaling refers to the procedure of using large-scale information, such as air pressure or temperature on a GCM or RCM grid cell, to predict fine-scale information, such as precipitation or temperature at a station. Downscaling can be either dynamic (i.e., using an RCM to increase the spatial resolution of a GCM output) or statistical (i.e., using a mapping function to convert large-scale information into fine-scale information). There are several statistical downscaling methods. The most popular methods include the delta-change, multiple regression, and quantile mapping or quantile-quantile (Q-Q). Bias correction is correcting discrepancies between RCM/GCM outputs and observation. It uses the same equation as downscaling (downscaling can be seen as removing the bias caused by the coarse resolution of GCM/RCMs).

2.5.1 The Delta-change method

The delta-change method consists of adding (or multiplying) the difference (by the ratio) between the simulated future and the historical mean of a particular variable to a historical time series. By doing so, climate change is incorporated into the historical baseline period. The method does not require a higher computation, making a very high-efficiency downscale of the GCM and RCPs scenarios over centuries.

The method has been applied extensively in climate change assessment (Luo and Haung, 2018; Lafon *et al.*, 2013; Teutschbein and Seibert, 2012; Van Roosmalen *et al.*, 2007; Mpelasoka and Chiew, 2009; Diaz-Nieto & Wilby, 2005). In fact, several studies have shown that the delta-change factor could predict the exact future variability while maintaining the same historical temporal structure (Hayhoe, 2010; Lenderink and Van Meijgaard, 2007; Diaz-Nieto and Wilby, 2005; Seidou *et al.*, 2012).

2.5.2 Multiple linear regression downscaling

Regression analysis is a statistical downscaling method that is used to determine the relationship between predictors and predictands. This technique is most widely applied because it does not require a complex computational requirement; it has easy implementation (Hessami *et al.*, 2008; Giorgi *et al.*, 2001; Fowler *et al.*, 2007). Most studies have used various regression analysis methods for the last two decades. For instance, Murphy (2000) utilized multiple linear regression analysis techniques in the Statistical DownScaling Model (SDSM). SDSM uses multiple linear regression to build a relationship between predictors and predictions and then constructs local-scale climate variables for current and future periods. Seidou *et al.* (2012) investigated Automated Statistical Downscaling (ASD), developed by Hessami *et al.* (2008), and discovered that ASD could not estimate wet days correctly. The precipitation events had to be modified. The uncertainty in regression methods was expected because of the low predictability of local-scale amounts (Burger, 2002). This issue has been addressed by Burger and Chen (2005), who forced the regression model to retain the covariance value at a local scale. To conclude, regression methods were poor at estimating the hydrological extremes due to the low resolution of models.

2.5.3 Quantile mapping (QM)

The QM method consists of remapping the probability density function (PDF) of the uncorrected regional climate model series atop the probability of the observed data series. The following formula produces the corrected RCM to CDF:

$$X_{Corrected}=F^{-1}_{Observed}\,(F_{RCM}(X_{RCM})) \qquad \text{Eq (2.1)}$$

where $\boldsymbol{X_{RCM}}$ denotes the RCM data before projection. The limitation of this approach is its inability to predict values beyond the range of historical data. Bias correction is used to capture a source of climate model errors and to identify the climate change signal. In recent studies, significant effort has been made to investigate the various post-processing techniques, such as simple additive and scaling corrections and quantile mapping (Fowler and Kilsby, 2007; Wood *et al.*, 2002; Wood *et al.*, 2004; Maurer and Hidalgo, 2008; Wang and Chen, 2014). Eden *et al.,* (2012) attempted to classify a source of climate model errors, and they clarified that the corrected precipitation variable using a statistical approach is a beneficial predictor for the observed data series on a global scale. However, performance evaluation must be considered to assess the bias correction methods. Most studies have used performance evaluation to identify the model error. Teng *et al.,* (2015) assessed several bias correction techniques for precipitation time series; the impact on a runoff model was evaluated using a two-state gamma distribution mapping method. The authors concluded that quantile mapping based on two-gamma distribution performed exceptionally well. Most recent studies have shown that quantile mapping performance is superior to a more straightforward bias correction in estimating the mean and variance in the precipitation data set (Teutschbein *et al.*, 2012; Gudmundsson *et al.*, 2012; Chen *et al.*, 2013). The large amounts of quantiles have shown that quantile mapping leads to the best performance for precipitation (Themeßl *et al.*, 2011). Heo *et al.,* (2019) stated that stationary data would lead the quantile mapping to perform successfully; in contrast, non-stationary data would cause an unreliable output. An alternative technique overcomes the problem with the quantile mapping performance, especially when dealing with a non-stationary data set. Quantile delta mapping, which preserves the relative changes of the whole quantile in a distribution, performs better than quantile mapping (Heo *et al.*, 2019; Cannon *et al.*, 2015). The bias correction methods depend on the assumption of time-independent quantiles over the examined period; however, this could be misleading in the context of climate change (Passow and Donner, 2017). Therefore, Passow and Donner (2017) proposed a novel method that combines linear quantile regression with quantile mapping to bring consistency to time-independent and trend-preservation bias correction.

To sum up, the quantile mapping method has been used widely in studying water resources affected by climate change. Quantile mapping is a bias correction technique introducing the relationship between historical and future data models. The method's performance was a significant step in testing the output of the model. Some studies have found that sub-annual data leads to the best performance (e.g., Wang and Chen, 2014; Teng *et al.*, 2015; Cannon *et al.*, 2015).

2.5.4 Equidistant quantile mapping

Li *et al.* (2010) proposed the equidistant mapping method to improve the QM method, which was the traditional method for bias correction.

$$\boldsymbol{\tilde{x}_{m-p.adjst} = x_{m-p} + F_{o-c}^{-1}\big(F_{m-p}(x_{m-p})\big) - F_{m-c}^{-1}\big(F_{m-p}(x_{m-p})\big)} \quad \text{Eq (2.2)}$$

where F_{m-p} is the CDF of the model for a future projection period, and F_{o-c}^{-1} and F_{m-c}^{-1} are the inverse of the distribution functions for observations and models in the reference period, respectively. Li *et al.,* (2010) found that EQM is superior to traditional downscaling methods such as QM. The main differences between QM and EQM are tabulated in Table 2.1 below.

However, several researchers have pointed out flaws in EQM. One of the shortcomings highlighted by Wang and Chen (2014) is that the right side of Equation (2.2) can become negative when correcting the raw model precipitation data, while the right side of equation (2.2) is always positive. Wang and Chen (2014) proposed modifying Li *et al.,* (2010) using the multiplicative quantile mapping factor instead of the additive quantile mapping factor.

Table 2.1 Differences and similarities between quantile mapping and equidistant quantile matching.

Methods	Quantile Mapping (QM)	Equidistant Quantile Mapping (EQM)
Definition	Quantile mapping (QM) is a statistical downscaling method that adjusts the cumulative distribution of GCM data to the cumulative distribution of observed precipitation using an appropriate transfer function.	Equidistant quantile mapping or matching (EQM) is a statistical transfer function to bias-correct climate change model data by taking the difference between future and baseline values and then adding this difference to the observed value.
Advantages	• QM assumes that climate model biases to be corrected are stationary. This method preserves the predicted GCM change at each quantile (Li *et al.*, 2010; Pierce *et al.*, 2015). • It adjusts all moments in CDF. • This method is computationally less intensive than other methods.	• The method preserves the predicted GCM mean at each quantile additively or multiplicatively. • The method considers changes in the distribution of future climate, including the distribution tails.
Disadvantages	• The bias-corrected values are the same as the reference period values. • QM fails to discriminate between physical processes and short-term fluctuations.	• The problem of the EQM is that it produces negative values of precipitation. • The method does not preserve standard deviation and skewness except mean.
Similarities	• Neither approach requires complex computation. • Both approaches alter the magnitude of changes in the mean of projected GCM from the original GCM. • Both approaches assume that the historical model is an error in value for a given model in the future (Pierce *et al.*, 2015). • Both methods are very straightforward to use.	
Differences	• QM assumes that the weather variable distribution of future periods is like that of the control period (Wang and Chen, 2014). • If the climate model includes too much variability, QM might reduce the variability at all temporal scales (Pierce *et al.*, 2015).	• EQM is reduced to QM when bias-correcting a control period (GCM) model.

Pierce *et al.,* (2015) also demonstrated that QM and EQM could significantly alter the GCM's mean climate change signal. The authors introduced an extension of EQM to address the problem with negative values in projected precipitation. The extension, called PresRat, starts by setting a zero-precipitation threshold for the GCM precipitation, for which the number of dry days is the same in the GCM output as in the observations. Values below that threshold in the GCM output are set to zero, and then the algorithm developed by Wang and Chen (2014) is applied. In addition, Pierce *et al.,* (2015) demonstrated that the new method is better than QM and EQM at preserving the changes in mean precipitation in the future. Srivastav *et al.,* (2014) and Singh *et al.,* (2016) adopted the EQM to update IDF curves under climate change. Similarly, Hassanzadeh *et al.,* (2019) compared three quantile-based downscaling methods (QM, EQM, and the Scale-Invariance Method [SIM]) and found that the performance of quantile-based downscaling approaches in reproducing observed extreme quantiles can be divergent. However, the differences between the three schemes are insignificant at lower return periods.

2.6 Intensity-duration-frequency curves under climate change

There are three methods for generating intensity-duration-frequency (IDF) curves under climate change: the delta-change method, quantile mapping, and climate change projection at a daily timescale, followed by temporal disaggregation. Constructing curves aims to show how climate change can have a positive or negative effect. After the curves are assessed, different decisions could be made for future water resources planning.

2.6.1 IDF generation using the delta-change method

The delta-change method assumes that the change factor calculated by the daily timescale applies to sub-daily timescales. For instance, Rodriguez *et al.,* (2014) applied the delta-change method to determine the impact of climate change on extreme rainfall values in Barcelona, Spain.

$$C_f = \frac{I(T,d)_{future}}{I(T,d)_{current}} \qquad \text{Eq (2.3)}$$

where C_f is the climate change factor, I is the precipitation intensity, T is the return period, and d is the duration. The authors found that the average climate change factor increased with the return period of any given precipitation intensity for all investigated climate change scenarios.

The delta-change method is a straightforward yet robust approach to developing climate change knowledge. This approach's main benefits are retaining the original time series (temporal and spatial variability) and reducing the bias inherent in climate-model simulation. CSA (2012) reported several case studies, including Atlantic Canada, Vancouver, and Southern Ontario, where the delta-change method was applied. The maximum likelihood became involved when distribution functions were fitted to the maximum annual precipitation. One goodness-of-fit criterion was applied to predict and evaluate the distribution fittings.

The delta-change factor could be applied to detect the variability of future extreme precipitation statistics to climate change. Switzman *et al.,* (2017) conducted a delta-change factor approach to compare multiple IDF projections in two different climate sites; they concluded that storm frequency increased due to climate change model selection. Also, the heterogeneity of climate model data collection was higher than that resulting from the spatial extent of extreme precipitation. This method has also been applied to estimate the future changes in annual maximum precipitation using A1B and A1 climate change models. For instance, Kuo *et al.,* (2015) used the delta-change method to estimate the IDF curves under climate change; although they used old climate models, future changes in extreme events were identified. Another study had similar objectives but used modern climate models. Kim *et al.,* (2018) estimated the future IDF period using different bias corrections, including the delta-change factor. Though the delta-change factor method is simplistic, method is widely applied in the climate and hydrology fields (as seen in the literature). This approach is indispensable because it logically represents the resulting change in the data set. All studies in this literature review indicated the value of the approach.

2.6.2 IDF curve generation using quantile mapping

Quantile mapping (QM) is one of the bias correction methods. The cumulative probability distribution function of simulated rainfall calibrated to observed rainfall at meteorological stations in the QM bias correction process (Ceglar & Kajfež-Bogataj, 2012). Hassanzadeh (2013), Kuo *et al.,* (2013), and Alam and Elshorbagy (2015) are examples of studies that have used a variant of QM. The selection of a theoretical probability distribution is the initial step of this method. The QM is also widely applied as a delta-change factor method to estimate future IDF curves.

Furthermore, as mentioned in Table 2.1, QM is not complex; it does not require an expensive computational process and is a very straightforward approach. This section discusses the previous QM used to construct the annual extreme precipitation series IDF curves. Switzman *et al.,* (2017) used QM methods to capture the changes in future IDF projections with different GCM and RCM scenarios. Shukor *et al.,* (2020) used QM to correct bias in climate model data, and they concluded that the QM was highly satisfactory as the mean root square was close to one. The performance of QM with IDF is similar when the method is used at a daily scale to detect bias-corrected annual extreme precipitation that would reflect the IDF values in future periods with different year events (return period); the readers are referred to the literature review on the QM method in this chapter.

2.7 Temporal disaggregation techniques

This section discusses precipitation disaggregation techniques, including definitions, theories, equations, advantages, and disadvantages. Also, the purposes of stochastic disaggregation application in hydrologic modelling are shown.

2.7.1 Uniform disaggregation models

The daily data is divided into 24 assigned to each hour, called the uniform disaggregation method. The uniform disaggregation method was the primary method to divide the day equally into 24 hours; however, the method does not give the actual precipitation events for 24 hours (Gutierrez-Magness and McCuen, 2004). Another method, known as weather patterns disaggregation, utilizes weather patterns based on climate information; this method was investigated by Gutierrez-Magness and McCuen (2004). The stochastic disaggregation model did not consider the weather patterns because they could not be transferred to a different site location (Gutierrez-Magness and McCuen, 2004; Wey, 2006). Gutierrez-Magness and McCuen (2004) suggested a bivariate satellite ratio disaggregation model that uses the hourly distribution of a station located near the watershed to disaggregate the daily data into hourly data on the station's neighbours. The data sets of the two sites should be in the same period to transfer data directly. The problem with this model is that if a site does not have precipitation data, the model will create a dry period in disaggregated data. Moreover, the ratios in the model create a negative bias (Wey, 2006).

2.7.2 The k-nearest neighbour disaggregation method

Hydro-meteorological time series on finer temporal scales are essential for assessing the hydrological effects of land use or climate change on medium and small watersheds. These time series are generally available at no less than daily time intervals. Disaggregation of time series into finer scales has become the most crucial water resource management technique. Obtaining hourly data is a significant step for storm control and management. Due to the complexity of sub-hourly recording, stochastic disaggregation models and their various aspects have been discussed and applied in many works of literature. For instance, the fragment method was the first disaggregation model to convert the daily scale into a 24-hour scale. The following paragraphs elaborate on the k-nearest neighbour (KNN) disaggregation model's application in daily precipitation scale with or without climate change projection and how the resolution would impact the results.

Climate change has been a critical issue that should be considered in all hydrology and water resources management for more than a decade to save and secure water. Some researchers have found that fine-scale studying is helpful in the assessment of climate impacts on regional sites. Lu *et al.,* (2015) assessed the climate change impacts on extreme regional rainfall in Singapore. They generate rainfall time series spatially and temporally by combining LARS-WG with the KNN model. They discovered that the maximum rate of increase for 100-year extremes would be 14.8% and 16.3% for a duration of 24-h and 1-h, respectively. The proposed approach could be improved to provide synthetic rainfall data in continuous high resolution.

The k-nearest neighbour (KNN) disaggregation technique is a particular case of the fragment (MF) method, a non-parametric approach commonly used by researchers for the above reason. The principle of the method is to generate fragments that are fractions of daily precipitation that occurred in each hour of the day, and then the fragments are summed to 1. The general formulation of the MF is given in Equation (2.4). Then, the fragment is multiplied by the daily scale of precipitation to obtain the converted time series as in the following formula (Equation [2.5]):

$$w_i = \frac{h_i}{\sum_{i=1}^{n} h_i} \qquad \text{Eq (2.4)}$$

$$h_i' = w_i \times d \qquad \text{Eq (2.5)}$$

In Equation (2.4), $\boldsymbol{w_i}$ is the weight that will be computed, $\boldsymbol{h_i}$ is the data from the series selected to produce fragments, and n is the series number (24 hours). The hourly series data used to estimate fragments could be chosen randomly, leading to inadequate statistical properties (Srikanthan and McMahon, 1982). Therefore, the best choice is to compare the total disaggregated daily precipitation with close total daily precipitation before disaggregation (Wey, 2006). The k-nearest neighbour is a particular case of the fragment method where the fragment is selected from historical hourly precipitation in a sample of neighbours with similar precipitation amounts.

The KNN model has been involved in several studies on IDF curves in the climate change field. Furthermore, the model is used as a weather generator and a conversion tool to synthesize time series. Shahabul and Elshorbagy (2015) found that the size and magnitude of future variations in extreme precipitation quantiles are sensitive to the selection of GCMs and RCPs and seem to intensify toward the end of the 21st century. The quantification of uncertainties suggests that GCMs are the main contributor to the uncertainty. To summarize, this paper follows a two-stage modelling method for spatial and temporal downscaling precipitation from the global to the local scale in Saskatoon, Canada. Based on the sub-hourly series, it was found that variations in the future extreme precipitation quantiles are significant at shorter durations and more considerable return periods compared to the historical values. Hourly and five-minute precipitation records were used to construct IDF curves during the baseline and projection periods. The uncertainty in the projections of future precipitation increases at shorter durations and for more extended return periods.

2.7.3 Random cascade disaggregation models

Olsson and Berndtsson (1998) were the first to introduce the disaggregation method known as the multiplicative random cascade model. The primary aim of the cascade model is to split the time step from a coarser scale into more delicate time scale steps on an equal duration basis. The branching technique creates boxes starting from a coarser scale (total daily precipitation). When the branching (b) factor equals 2, then the coarser scale is divided into two boxes (see Figure 2.2). Each box represents a small amount of coarser scale. This stochastic model depends on the empirical observation of precipitation events. The model divides the precipitation amount at each level by using calibration with observed data and estimating the probability distribution for each climate station (see Figure 2.2). The advantage of the model is that it can produce various statistics for precipitation at the site (Olsson and Berndtsson, 1998). The cascade model is also commonly applied in urban hydrology. Based on the mass conservation of the model, it can be divided into microcanonical or canonical models. The microcanonical model preserves the precipitation amount of each time step. Moreover, the estimation of the parameters could be directly estimated from data (Carsteau and Foufoula-Georgiou, 1996; Müller and Haberlandt, 2015). On the other hand, the canonical cascade method is a downscaling method, and the microcanonical method is a disaggregation method. The canonical cascade method maintains the average of the precipitation data at each timescale (Langousis *et al.*, 2013). Cascade models have been used in different hydrology and water resource management fields. Jebri *et al.,* (2012) used a cascade multiplicative random model created by Olsson (1998) to estimate the soil erosion rate by utilizing an hourly precipitation data set. The model disaggregates the short scale of daily rainfall, and the downscaled output is applied to estimate the soil erosion index over a watershed on a spatial basis. The soil erosion index is one parameter that could help inform hydrologists about rainfall intensity - especially in some arid lands. Therefore, Jebri *et al.,* (2012) attempted to estimate the erosion rate using the disaggregated short scale of rainfall, and the random cascade approach was used to determine its efficiency in estimating the soil erosion index. Gaur and Lacasse (2018) used the multiplicative random cascade model for multivariate climate parameters at multiple sites in the same region. They concluded that the model applies to multisite grid-level statistics with at least 90% accuracy. The model is found to model more than one parameter. Furthermore, the model preserves statistical properties such as mean, standard deviation, and cross-correlation coefficient. Müller and Haberlundt (2018) studied temporal disaggregation using the multiplicative cascade method for a spatial area in urban hydrology. The model used in their study could be applied to achieve spatial consistency, without which the flood volumes of the sewer system are underestimated. The paper applied two disaggregation models: model A is a

1280-minute approach, and model B is a uniform splitting approach. Model B performed better than model A. While model B led to the best representation of observation, model A poorly represented an oversampling version. Garbrecht *et al.,* (2017) used a cascade rainfall model in the central plains of the United States to investigate the performance of the multiplicative random cascade model. The author found that the model could replicate well for different hourly and sub-hourly periods in terms of average and less persistent rainfall. Liczner *et al.* (2011) used six versions of the multiplicative cascade model to generate a fine-resolution scale. The proposed model used a beta-normal generator for a microcanonical cascade, and it produced a statistical behaviour of intermittency on a five-minute scale. In contrast, the canonical cascade model failed to produce the behaviour of an intermittent period of rainfall properly. Molnar and Burlando (2005) used the model to convert and analyze 1280 minutes to 10 minutes for 20 years; they briefly concluded the following important points: observed rainfall, intermittency period, and the canonical cascade model are beneficial for urban water system studies due to the simplicity of the model's parameter estimation. The uniform splitting approach has achieved a high resolution of a precipitation data set (Müller & Haberlandt, 2015). Muller and Haberlandt (2015) concluded that the multiplicative random cascade model showed errors in the range of 3% to 12% according to the relative error (r) and mean absolute error (MAE). Furthermore, the model outputs were compared with observed precipitation. Spatial precipitation can be estimated by using annealing algorithms. The number of sites in the study area plays a crucial role in reproducing the performance decline with some rainfall characteristics. The conclusion is that the resampling approach could achieve better performance.

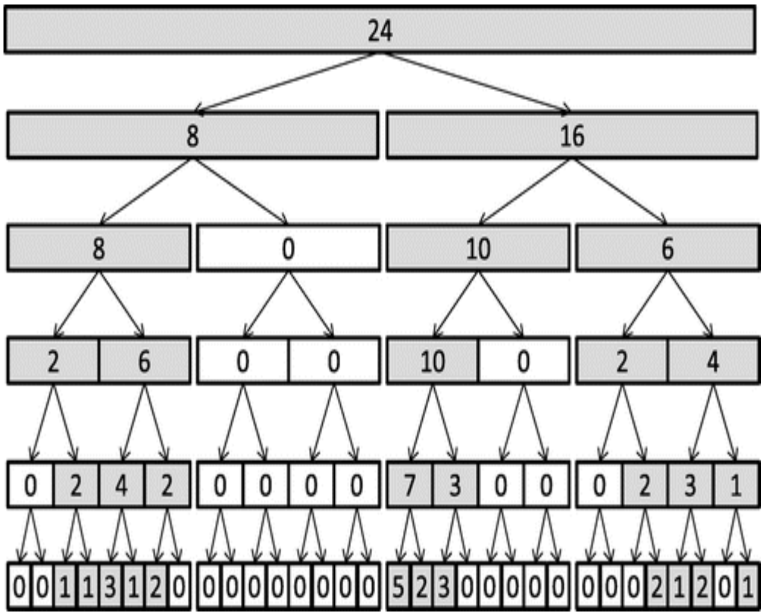

Figure 2.2 Random cascade model branching (b=2) (Olsson, 1998).

In this section, the cascade model is called a multiplicative model. It is an unbounded model because it conserves the daily amount in each time step. The original time series could be reassembled by aggregation of the disaggregated data. Also, the cascade model parameters could be estimated directly from the actual daily data set by reversing the cascade model to the observed data of a station. This model determines the rainfall intensity at each hourly time step and preserves the precipitation distribution for the daily series.

In all disaggregation steps explained previously, the random cascade model preserves the mass, meaning that the total amount of disaggregated daily precipitation equals the respective value of observed daily precipitation. The model is applied successfully for daily precipitation due to its simplicity, even though the parameters' estimation and the model are complex (Molnar and Burlando, 2005). This section discusses in more detail the literature on using the random cascade model and its theoretical framework of the multiplicative random cascade. Explaining the disaggregation of daily precipitation into an hourly series shows how precipitation is distributed over the daily period. The cascade levels are based on the branching numbers. As cascade levels increase, precipitation amount resolution will increase. The cascade model aggregates the results into the original scale. Then, statistical calculations are performed on aggregated data.

2.7.4 Hurst-Kolmogorov downscaling model

The other approach to temporal downscaling is the Hurst-Kolmogorov process (HKP), a stochastic process disaggregation model that uses a Gaussian white noise to convert the precipitation from coarse finer scales. HKP method can be applied to hydrology and water resources management in acquiring sub-hourly or sub-daily scales for different purposes of urban water systems.

Stochastic descriptions of such fields are the only way to characterize them macroscopically while also enabling simulations of the fields. Such simulations are helpful for engineering design, hydrometeorological forecasting, and water resource management. Stochastic fields are a straightforward extension of the theory of stochastic processes, which can explain the spatial and spatiotemporal structure of hydrometeorological fields (Schertzer and Lovejoy, 1987; Gagnon *et al.*, 2006; Veneziano and Langousis, 2010).

The HKP typically describes the natural phenomenon by fractional white noise in hydrological modelling. The HKP was first introduced by Hurst (1951). Hurst (1951) observed randomness in numerous physical time series, and the tendency of natural events was the most significant even though these events are in higher and lower values. Some studies have tried to identify the value of the Hurst exponent. According to Koutsoyiannis and Cohn (2008), the inability to recognize Hurst behaviour may be due to the unfavourable term used. Long memory (a metaphor for slowly declining autocorrelation) sends the wrong message, resulting in an inaccurate understanding of the physical mechanism. According to Klemes (1974), the Hurst value is not always a signal of infinite memory of a process, and the Hurst process can be described in terms of long-term change rather than long-term memory. Applying the idea of maximal entanglement (i.e., uncertainty) across several timescales yields the same result.

Hurst-Kolmogorov (HK) behaviour is the name given to this type of behaviour. HK behaviour is caused by changes occurring at multiple timescales according to Koutsoyiannis and Cohn (2008).

The HKP model has not been applied to generate IDF curves. Instead, it is used to reproduce the statistical properties of the new time series set. The model has never played a role in updating the urban water system because the output of the model has not been utilized. The main challenge of this model is estimating the exponent of the Hurst value from the actual data time series. At the desired finer (lower-level) timescale, a stationary disaggregation technique replicates the rainfall time series with a dependency structure, wet/dry probability, and marginal distribution. The technique maintains complete consistency with variables at an coarser (higher) level of timescales. This method produces a unique and concise mathematical framework that includes broad analytical formulations of mean, variance, and autocorrelation function (ACF) for a mixed-type stochastic process. As proof of concept, an application to real-world rainfall timings is presented. The HKP model has not been applied to daily or coarse-scale time series under climate change conditions. Studies related to this model, such as Lombardo *et al.* (2017) and Lombardo *et al.* (2012), have not included the daily time series of a climate change model for scenarios RCP 4.5 and 8.5. A few studies have mentioned the HKP, multiplicative (Lombardo *et al.*, 2017; Lombardo *et al.*, 2012; Koutsoyiannis, 2003) random cascade models related to climate variability (Willems *et al.*, 2013), impacts of climate change on the urban drainage system, or extreme events due to increasing greenhouse gas emissions or increasing average temperature exposure (Willems *et al.*, 2013). The HKP has described extreme precipitation phenomena and uncertainty analysis, such as in a study by Koutsoyiannis (2003).

2.8 Conclusion

The equidistant quantile mapping approach is widely applied in water resource engineering, especially in studying the relationship between climate change impacts and hydrological variables such as precipitation. However, equidistant quantile mapping needs more investigation regarding performance and uncertainty measures. Equidistant quantile mapping has been improved to avoid negative values in projected models concerning preserving mean changes in GCM and future model data. While the performance of equidistant quantile mapping is superior to that of traditional quantile transformation, the improved equidistant quantile mapping performs best in comparison to other methods of statistical downscaling. This method could be further improved and applied to other climate variables. As well, uncertainty measures could be applied.

The disaggregation models convert the data series from large scale to small scale. This report briefly explains the methods that are currently used for different simulation models. In addition, stochastic disaggregation models are crucial subjects for estimating the hourly data after the disaggregation process. The disaggregated daily data should be matched with the observed hourly series to obtain the same total values in both series. The fragment methods were found to be the most accurate for converting daily data to hourly data, and these are the most popular methods in hydrologic modelling. Microcanonical and canonical cascade models are comprised of temporal disaggregation methods based on the scale or branching. Disaggregation methods require further study because they are only suitable for a single site. Therefore, the disaggregation methods are limited in converting regional daily precipitation to hourly precipitation or annual regional flow to monthly annual flow. Furthermore, the unavailability of observed hourly data makes simulation difficult. The optimal performance of these methods means that output data maintains the most critical statistical characteristics of mean, standard deviation, and correlation coefficient.

2.9 References

Al-Amri, N. S., & Subyani, A. M. (2017). Generation of rainfall intensity duration frequency (IDF) curves for ungauged sites in arid region. *Earth Systems and Environment*, *1*(1), 1–12.

Alzahrani, F. (2013). *An approach to quantifying uncertainty in estimates of intensity duration frequency (IDF) curves*.

Bernardara, P., Lang, M., Sauquet, E., Schertzer, D., & Tchiriguyskaia, I. (2007). *Multifractal analysis in hydrology: Application to time series*. Editions Quae.

Boé, J., Terray, L., Martin, E., & Habets, F. (2009). Projected changes in components of the hydrological cycle in French river basins during the 21st century. *Water Resources Research*, *45*(8).

Bougadis, J., & Adamowski, K. (2006). Scaling model of a rainfall intensity-duration-frequency relationship. *Hydrological Processes*, *20*(17), 3747–3757.

Bürger, G., & Chen, Y. (2005). Regression-based downscaling of spatial variability for hydrologic applications. *Journal of Hydrology*, *311*(1–4), 299–317.

Burlando, P., & Rosso, R. (1996). Scaling and muitiscaling models of depth-duration-frequency curves for storm precipitation. *Journal of Hydrology*, *187*(1–2), Article 1–2.

Cannon, A. J., Sobie, S. R., & Murdock, T. Q. (2015). Bias correction of GCM precipitation by quantile mapping: How well do methods preserve changes in quantiles and extremes? *Journal of Climate*, *28*(17), 6938–6959.

Cârsteanu, A., & Foufoula-Georgiou, E. (1996). Assessing dependence among weights in a multiplicative cascade model of temporal rainfall. *Journal of Geophysical Research: Atmospheres*, *101*(D21), 26363–26370.

Ceglar, A., & Kajfež-Bogataj, L. (2012). Simulation of maize yield in current and changed climatic conditions: Addressing modelling uncertainties and the importance of bias correction in climate model simulations. *European Journal of Agronomy*, *37*(1), 83–95.

Chandra, R., Saha, U., & Mujumdar, P. P. (2015). Model and parameter uncertainty in IDF relationships under climate change. *Advances in Water Resources*, *79*, 127–139.

Chauveau, M., Chazot, S., Perrin, C., Bourgin, P.-Y., Sauquet, E., Vidal, J.-P., Rouchy, N., Martin, E., David, J., & Norotte, T. (2013). Quels impacts des changements climatiques sur les eaux de surface en France à l'horizon 2070? *La Houille Blanche*, *4*, 5–15.

Cheng, L., & AghaKouchak, A. (2014). *Nonstationary precipitation intensity-duration-frequency curves for infrastructure design in a changing climate. Sci. Rep., 4, 7093*.

Climate Models | NOAA Climate.gov. (n.d.). Retrieved March 24, 2023, from http://www.climate.gov/maps-data/climate-data-primer/predicting-climate/climate-models

Coulibaly, P., & Shi, X. (2005). Identification of the effect of climate change on future design standards of drainage infrastructure in Ontario. *Report Prepared by McMaster University with Funding from the Ministry of Transportation of Ontario*, *82*.

CSA PLUS 4013-2019—Technical guide: Development, interpretation and use of rainfall intensity-duration-frequency (IDF) information: Guideline for Canadian water resources practitioners. (2019). Retrieved December 12, 2021, from https://webstore.ansi.org/Standards/CSA/CSAPLUS40132019?source=preview

Dai, A., Rasmussen, R. M., Liu, C., Ikeda, K., & Prein, A. F. (2020). A new mechanism for warm-season precipitation response to global warming based on convection-permitting simulations. *Climate Dynamics*, *55*(1), 343–368.

Diaz-Nieto, J., & Wilby, R. L. (2005). A comparison of statistical downscaling and climate change factor methods: Impacts on low flows in the River Thames, United Kingdom. *Climatic Change*, *69*(2), 245–268.

Donnelly, C., Greuell, W., Andersson, J., Gerten, D., Pisacane, G., Roudier, P., & Ludwig, F. (2017). Impacts of climate change on European hydrology at 1.5, 2 and 3 degrees mean global warming above preindustrial level. *Climatic Change*, *143*(1), 13–26.

Eden, J. M., Widmann, M., Grawe, D., & Rast, S. (2012). Skill, Correction, and Downscaling of GCM-Simulated Precipitation. *Journal of Climate*, *25*(11), 3970–3984.

Elsebaie, I. H. (2012). Developing rainfall intensity–duration–frequency relationship for two regions in Saudi Arabia. *Journal of King Saud University-Engineering Sciences*, *24*(2), 131–140.

Fowler, H. J., & Kilsby, C. G. (2007). Using regional climate model data to simulate historical and future river flows in northwest England. *Climatic Change*, *80*(3–4), 337–367.

Frisch, U., & Parisi, G. (1980). Fully developed turbulence and intermittency. *New York Academy of Sciences, Annals*, *357*, 359–367.

Gagnon, J.-S., Lovejoy, S., & Schertzer, D. (2006). Multifractal earth topography. *Nonlinear Processes in Geophysics*, *13*(5), 541–570. https://doi.org/10.5194/npg-13-541-2006

Garbrecht, J. D., Gyawali, R., Malone, R. W., & Zhang, J. C. (2017). Cascade rainfall disaggregation application in US Central Plains. *Environment and Natural Resources Research*, *7*(4), 30–43.

Gaur, A., & Lacasse, M. (2018). Multisite multivariate disaggregation of climate parameters using multiplicative random cascades. *Urban Climate*, *26*, 121–132.

Giorgi, F., Hewitson, B., Arritt, R., Gutowski, W., Gutowski, W., Knutson, T., & Landsea, C. (2001). *Regional climate information—Evaluation and projections*.

Gudmundsson, L., Bremnes, J. B., Haugen, J. E., & Engen-Skaugen, T. (2012). Technical Note: Downscaling RCM precipitation to the station scale using statistical transformations – a comparison of methods. *Hydrology and Earth System Sciences*, *16*(9), 3383–3390.

Gutierrez-Magness, A. L., & McCuen, R. H. (2004). Accuracy Evaluation of Rainfall Disaggregation Methods. *Journal of Hydrologic Engineering*, *9*(2), 71–78.

Habets, F., Boé, J., Déqué, M., Ducharne, A., Gascoin, S., Hachour, A., Martin, E., Pagé, C., Sauquet, E., & Terray, L. (2013). Impact of climate change on the hydrogeology of two basins in northern France. *Climatic Change*, *121*(4), 771–785.

Hassanzadeh, E., Nazemi, A., Adamowski, J., Nguyen, T.-H., & Van-Nguyen, V.-T. (2019). Quantile-based downscaling of rainfall extremes: Notes on methodological functionality, associated uncertainty and application in practice. *Advances in Water Resources*, *131*, 103371.

Hattermann, F. F., Krysanova, V., Gosling, S. N., Dankers, R., Daggupati, P., Donnelly, C., Flörke, M., Huang, S., Motovilov, Y., & Buda, S. (2017). Cross-scale intercomparison of climate change impacts simulated by regional and global hydrological models in eleven large river basins. *Climatic Change*, *141*(3), 561–576.

Hayhoe, K. A. (2010). A standardized framework for evaluating the skill of regional climate downscaling techniques [Ph.D., University of Illinois at Urbana-Champaign]. In *ProQuest Dissertations and Theses* (787898828).

Heo, J.-H., Ahn, H., Shin, J.-Y., Kjeldsen, T. R., & Jeong, C. (2019). Probability Distributions for a Quantile Mapping Technique for a Bias Correction of Precipitation Data: A Case Study to Precipitation Data Under Climate Change. *Water*, *11*(7).

Hessami, M., Gachon, P., Ouarda, T. B., & St-Hilaire, A. (2008). Automated regression-based statistical downscaling tool. *Environmental Modelling & Software*, *23*(6), 813–834.

Houze Jr, R. A. (1997). Stratiform precipitation in regions of convection: A meteorological paradox? *Bulletin of the American Meteorological Society*, *78*(10), 2179–2196.

Huard, D., Mailhot, A., & Duchesne, S. (2010). Bayesian estimation of intensity–duration–frequency curves and of the return period associated to a given rainfall event. *Stochastic Environmental Research and Risk Assessment*, *24*, 337–347.

Hurst, H. E. (1951). Long-term storage capacity of reservoirs. *Transactions of the American Society of Civil Engineers*, *116*(1), 770–799.

Innocenti, S., Mailhot, A., & Frigon, A. (2017). Simple scaling of extreme precipitation in North America. *Hydrology and Earth System Sciences*, *21*(11), Article 11.

IPCC Fifth Assessment Report. (2013). *AR5 Climate Change 2013: The Physical Science Basis — IPCC*.

Jakob Themeßl, M., Gobiet, A., & Leuprecht, A. (2011). Empirical-statistical downscaling and error correction of daily precipitation from regional climate models. *International Journal of Climatology*, *31*(10), 1530–1544.

Jebari, S., Berndtsson, R., Olsson, J., & Bahri, A. (2012). Soil erosion estimation based on rainfall disaggregation. *Journal of Hydrology*, *436–437*, 102–110.

Kim, J., Tanveer, M. E., & Bae, D.-H. (2018). Quantifying climate internal variability using an hourly ensemble generator over South Korea. *Stochastic Environmental Research and Risk Assessment*, *32*(11), 3037–3051.

Klemeš, V. (1974). The Hurst Phenomenon: A puzzle? *Water Resources Research*, *10*(4), 675–688.

Koutsoyiannis, D. (2003). Climate change, the Hurst phenomenon, and hydrological statistics. *Hydrological Sciences Journal*, *48*(1), 3–24.

Koutsoyiannis, D. (2020). Revisiting the global hydrological cycle: Is it intensifying? *Hydrology and Earth System Sciences*, *24*(8), 3899–3932.

Koutsoyiannis, D., & Cohn, T. (2008). *The Hurst phenomenon and climate (solicited)*.

Kuo, C., Jahan, N., Gizaw, M., Gan, T., & Chan, S. (2013). *The climate change impact on future IDF curves in central Alberta*. *2729*.

Kuo, C.-C., Gan, T. Y., & Gizaw, M. (2015). Potential impact of climate change on intensity duration frequency curves of central Alberta. *Climatic Change*, *130*(2), 115–129.

Lafaysse, M., Hingray, B., Mezghani, A., Gailhard, J., & Terray, L. (2014). Internal variability and model uncertainty components in future hydrometeorological projections: The Alpine Durance basin. *Water Resources Research*, *50*(4), 3317–3341.

Lafon, T., Dadson, S., Buys, G., & Prudhomme, C. (2013). Bias correction of daily precipitation simulated by a regional climate model: A comparison of methods. *International Journal of Climatology*, *33*(6), 1367–1381.

Langousis, A., Carsteanu, A. A., & Deidda, R. (2013). A simple approximation to multifractal rainfall maxima using a generalized extreme value distribution model. *Stochastic Environmental Research and Risk Assessment*, *27*(6), Article 6.

Langousis, A., & Veneziano, D. (2007). Intensity-duration-frequency curves from scaling representations of rainfall. *Water Resources Research*, *43*(2), Article 2.

Lenderink, G., & van Meijgaard, E. (2008). Increase in hourly precipitation extremes beyond expectations from temperature changes. *Nature Geoscience*, *1*(8), 511–514.

Li, H., Sheffield, J., & Wood, E. F. (2010). Bias correction of monthly precipitation and temperature fields from Intergovernmental Panel on Climate Change AR4 models using equidistant quantile matching. *Journal of Geophysical Research: Atmospheres*, *115*(D10).

Licznar, P., Łomotowski, J., & Rupp, D. E. (2011). Random cascade driven rainfall disaggregation for urban hydrology: An evaluation of six models and a new generator. *Atmospheric Research*, *99*(3–4), 563–578.

Lombardo, F., Volpi, E., & Koutsoyiannis, D. (2012). Rainfall downscaling in time: Theoretical and empirical comparison between multifractal and Hurst-Kolmogorov discrete random cascades. *Hydrological Sciences Journal*, *57*(6), 1052–1066.

Lombardo, F., Volpi, E., Koutsoyiannis, D., & Serinaldi, F. (2017). A theoretically consistent stochastic cascade for temporal disaggregation of intermittent rainfall. *Water Resources Research*, *53*(6), 4586–4605. https://doi.org/10.1002/2017WR020529

Lu, Y., Qin, X. S., & Mandapaka, P. V. (2015). A combined weather generator and K-nearest-neighbour approach for assessing climate change impact on regional rainfall extremes. *International Journal of Climatology*, *35*(15), 4493–4508.

Luo, Y., & Huang, Y. (2018). A new combined approach on Hurst exponent estimate and its applications in realized volatility. *Physica A: Statistical Mechanics and Its Applications*, *492*, 1364–1372.

Mailhot, A., Duchesne, S., Rivard, G., Nantel, E., Caya, D., & Villeneuve, J. (2006). *Climate change impacts on the performance of urban drainage systems for southern Québec*. *10*.

Margulis, S. A., & Entekhabi, D. (2001). Temporal disaggregation of satellite-derived monthly precipitation estimates and the resulting propagation of error in partitioning of water at the land surface. *Hydrology and Earth System Sciences*, *5*(1), 27–38.

Marta, B., Kohnova, S., Ladislav, G., Szolgay, J., & Hlavčová, K. (2009). Estimation of IDF curves of extreme rainfall by simple scaling in Slovakia. *Contributions to Geophysics and Geodesy*, *39*(3), Article 3.

Martel, J.-L., Brissette, F. P., Lucas-Picher, P., Troin, M., & Arsenault, R. (2021). Climate Change and Rainfall Intensity–Duration–Frequency Curves: Overview of Science and Guidelines for Adaptation. *Journal of Hydrologic Engineering*, *26*(10), 03121001.

Maurer, E. P., & Hidalgo, H. G. (2008). Utility of daily vs. Monthly large-scale climate data: An intercomparison of two statistical downscaling methods. *Hydrology and Earth System Sciences*, *12*(2), 551–563.

Meehl, G. A., Covey, C., Delworth, T., Latif, M., McAvaney, B., Mitchell, J. F., Stouffer, R. J., & Taylor, K. E. (2007). The WCRP CMIP3 multimodel dataset: A new era in climate change research. *Bulletin of the American Meteorological Society*, *88*(9), 1383–1394.

Mélèse, V., Blanchet, J., & Molinié, G. (2018). Uncertainty estimation of Intensity–Duration–Frequency relationships: A regional analysis. *Journal of Hydrology*, *558*, 579–591.

Menabde, M., Seed, A., & Pegram, G. (1999). A simple scaling model for extreme rainfall. *Water Resources Research*, *35*(1), Article 1.

Menzel, L., & Bürger, G. (2002). Climate change scenarios and runoff response in the Mulde catchment (Southern Elbe, Germany). *Journal of Hydrology*, *267*(1–2), 53–64.

Mirhosseini, G., Srivastava, P., & Fang, X. (2014). Developing Rainfall Intensity-Duration-Frequency Curves for Alabama under Future Climate Scenarios Using Artificial Neural Networks. *Journal of Hydrologic Engineering*, *19*(11), 04014022.

Molnar, P., & Burlando, P. (2005). Preservation of rainfall properties in stochastic disaggregation by a simple random cascade model. *Precipitation in Urban Areas*, *77*(1), 137–151.

Mpelasoka, F. S., & Chiew, F. H. (2009). Influence of rainfall scenario construction methods on runoff projections. *Journal of Hydrometeorology*, *10*(5), 1168–1183.

Müller, H., & Haberlandt, U. (2015). Temporal Rainfall Disaggregation with a Cascade Model: From Single-Station Disaggregation to Spatial Rainfall. *Journal of Hydrologic Engineering*, *20*(11), 04015026.

Murphy, J. (2000). Predictions of climate change over Europe using statistical and dynamical downscaling techniques. *International Journal of Climatology*, *20*(5), 489–501.

Nguyen, T.-D., Nguyen, V.-T.-V., & Gachon, P. (2007). A Spatial–Temporal Downscaling Approach for Construction of Intensity–Duration–Frequency Curves in Consideration of Gcm-Based Climate Change Scenarios. In *Advances in Geosciences: Volume 6: Hydrological Science (HS)* (pp. 11–21). World Scientific.

Nguyen, T.-H., & Nguyen, V.-T.-V. (2018). *A Novel Scale-Invariance Generalized Extreme Value Model Based on Probability Weighted Moments for Estimating Extreme Design Rainfalls in the Context of Climate Change*. 251–261.

Nguyen, V., Nguyen, T.-D., & Ashkar, F. (2002). Regional frequency analysis of extreme rainfalls. *Water Science and Technology*, *45*(2), Article 2.

Nguyen, V.-T.-V. (2020). *Development of New Methods for Updating IDF Curves in Canada in the Context of Climate Change*. 186–200.

Nguyen, V.-T.-V., Nguyen, T.-D., & Cung, A. (2007). A statistical approach to downscaling of sub-daily extreme rainfall processes for climate-related impact studies in urban areas. *Water Science and Technology: Water Supply*, *7*(2), Article 2.

Olsson, J. (1998). Evaluation of a scaling cascade model for temporal rain-fall disaggregation. *Hydrology and Earth System Sciences*, *2*(1), 19–30.

Olsson, J., & Berndtsson, R. (1998). Temporal rainfall disaggregration based on scaling properties. *Use of Historical Rainfall Series for Hydrological Modelling*, *37*(11), 73–79.

Onof, C., & Arnbjerg-Nielsen, K. (2009). Quantification of anticipated future changes in high resolution design rainfall for urban areas. *Atmospheric Research*, *92*(3), 350–363.

Ormsbee, L. E. (1989). Rainfall disaggregation model for continuous hydrologic modeling. *Journal of Hydraulic Engineering*, *115*(4), 507–525.

Passow, C., & Donner, R. (2017). Linear Regression Quantile Mapping (RQM)—A new approach to bias correction with consistent quantile trends. *EGU General Assembly Conference Abstracts*, 12203.

Pierce, D. W., Cayan, D. R., Maurer, E. P., Abatzoglou, J. T., & Hegewisch, K. C. (2015). Improved Bias Correction Techniques for Hydrological Simulations of Climate Change. *Journal of Hydrometeorology*, *16*(6), 2421–2442.

Poujol, B., Mooney, P., & Sobolowski, S. (2021). Physical processes driving intensification of future precipitation in the mid-to high latitudes. *Environmental Research Letters*, *16*(3), 034051.

Poujol, B., Sobolowski, S., Mooney, P., & Berthou, S. (2020). A physically based precipitation separation algorithm for convection-permitting models over complex topography. *Quarterly Journal of the Royal Meteorological Society*, *146*(727), 748–761.

Prodanovic, P., & Simonovic, S. P. (2007). *Dynamic Feedback Coupling of Continuous Hydrologic and Socio-Economic Model Components of the Upper Thames River Basin*. Department of Civil and Environmental Engineering, The University of Western.

Ragno, E., AghaKouchak, A., Love, C. A., Cheng, L., Vahedifard, F., & Lima, C. H. (2018). Quantifying changes in future intensity-duration-frequency curves using multimodel ensemble simulations. *Water Resources Research*, *54*(3), 1751–1764.

Rodríguez, R., Navarro, X., Casas, M. C., Ribalaygua, J., Russo, B., Pouget, L., & Redaño, A. (2014). Influence of climate change on IDF curves for the metropolitan area of Barcelona (Spain). *International Journal of Climatology*, *34*(3), 643–654.

Roe, G. H. (2005). Orographic precipitation. *Annu. Rev. Earth Planet. Sci.*, *33*, 645–671.

Schardong, A., & P Simonovic, S. (2019). *Application of Regional Climate Models for Updating Intensity-duration-frequency Curves under Climate Change*.

Schardong, A., & Simonovic, S. P. (2015). Coupled self-adaptive multiobjective differential evolution and network flow algorithm approach for optimal reservoir operation. *Journal of Water Resources Planning and Management*, *141*(10), 04015015.

Schardong, A., Simonovic, S. P., Gaur, A., & Sandink, D. (2020). Web-Based Tool for the Development of Intensity Duration Frequency Curves under Changing Climate at Gauged and Ungauged Locations. *Water*, *12*(5).

Schertzer, D., & Lovejoy, S. (1987). Physical modeling and analysis of rain and clouds by anisotropic scaling multiplicative processes. *Journal of Geophysical Research: Atmospheres*, *92*(D8), 9693–9714.

Seidou, O., Ramsay, A., & Nistor, I. (2012). Climate change impacts on extreme floods I: Combining imperfect deterministic simulations and non-stationary frequency analysis. *Natural Hazards*, *61*(2), 647–659.

Semenov, V., & Bengtsson, L. (2002). Secular trends in daily precipitation characteristics: Greenhouse gas simulation with a coupled AOGCM. *Climate Dynamics*, *19*(2), 123–140.

Şen, O., & Kahya, E. (2021). Impacts of climate change on intensity–duration–frequency curves in the rainiest city (Rize) of Turkey. *Theoretical and Applied Climatology*, *144*(3), 1017–1030.

Shahabul Alam, Md., & Elshorbagy, A. (2015). Quantification of the climate change-induced variations in Intensity–Duration–Frequency curves in the Canadian Prairies. *Journal of Hydrology*, *527*, 990–1005.

Shukor, M. S. A., Yusop, Z., Yusof, F., Sa'adi, Z., & Alias, N. E. (2020). Detecting rainfall trend and development of future intensity duration frequency (IDF) curve for the state of Kelantan. *Water Resources Management*, *34*(10), 3165–3182.

Silva, D. F., Simonovic, S. P., Schardong, A., & Goldenfum, J. A. (2021). Assessment of non-stationary IDF curves under a changing climate: Case study of different climatic zones in Canada. *Journal of Hydrology: Regional Studies*, *36*, 100870.

Simonovic, S. P., & Peck, A. (2009). *Updated rainfall intensity duration frequency curves for the City of London under the changing climate*. Department of Civil and Environmental Engineering, The University of Western ….

Singh, R., Arya, D. S., Taxak, A. K., & Vojinovic, Z. (2016). Potential Impact of Climate Change on Rainfall Intensity-Duration-Frequency Curves in Roorkee, India. *Water Resources Management*, *30*(13), 4603–4616.

Solaiman, T. A., & Simonovic, S. P. (2011). *Development of probability based intensity-duration-frequency curves under climate change*.

Soltani, S., Almasi, P., Helfi, R., Modarres, R., Esfahani, P. M., & Dehno, M. G. (2020). A new approach to explore climate change impact on rainfall intensity–duration–frequency curves. *Theoretical and Applied Climatology*, *142*(3), Article 3.

Srivastav, R. K., Schardong, A., & Simonovic, S. P. (2014). Equidistance Quantile Matching Method for Updating IDFCurves under Climate Change. *Water Resources Management*, *28*(9), 2539–2562.

Subyani, A. M., & Al-Amri, N. S. (2015). IDF curves and daily rainfall generation for Al-Madinah city, western Saudi Arabia. *Arabian Journal of Geosciences*, *8*(12), 11107–11119.

Sunyer, M. A., Gregersen, I. B., Rosbjerg, D., Madsen, H., Luchner, J., & Arnbjerg-Nielsen, K. (2015). Comparison of different statistical downscaling methods to estimate changes in hourly extreme precipitation using RCM projections from ENSEMBLES. *International Journal of Climatology*, *35*(9), Article 9.

Svensson, C., Clarke, R. T., & Jones, D. A. (2007). An experimental comparison of methods for estimating rainfall intensity-duration-frequency relations from fragmentary records. *Journal of Hydrology*, *341*(1–2), 79–89.

Switzman, H., Razavi, T., Traore, S., Coulibaly, P., Burn, D. H., Henderson, J., Fausto, E., & Ness, R. (2017). Variability of future extreme rainfall statistics: Comparison of multiple IDF projections. *Journal of Hydrologic Engineering*, *22*(10), 04017046.

Teng, J., Potter, N., Chiew, F., Zhang, L., Wang, B., Vaze, J., & Evans, J. (2015). How does bias correction of regional climate model precipitation affect modelled runoff? *Hydrology and Earth System Sciences*, *19*(2), 711–728.

Teutschbein, C., & Seibert, J. (2012). Bias correction of regional climate model simulations for hydrological climate-change impact studies: Review and evaluation of different methods. *Journal of Hydrology*, *456–457*, 12–29.
Trenberth, K. E. (2011). Changes in precipitation with climate change. *Climate Research*, *47*(1–2), 123–138.

Trenberth, K. E., Dai, A., Rasmussen, R. M., & Parsons, D. B. (2003). The changing character of precipitation. *Bulletin of the American Meteorological Society*, *84*(9), 1205–1218.

Uraba, M. B., Gunawardhana, L. N., Al-Rawas, G. A., & Baawain, M. S. (2019). A downscaling-disaggregation approach for developing IDF curves in arid regions. *Environmental Monitoring and Assessment*, *191*(4), 245.

Van Roosmalen, L., Christensen, B. S., & Sonnenborg, T. O. (2007). Regional differences in climate change impacts on groundwater and stream discharge in Denmark. *Vadose Zone Journal*, *6*(3), 554–571.

Veneziano, D., & Furcolo, P. (2002a). Multifractality of rainfall and scaling of intensity-duration-frequency curves. *Water Resources Research*, *38*(12), Article 12.

Veneziano, D., & Furcolo, P. (2002b). Multifractality of rainfall and scaling of intensity-duration-frequency curves. *Water Resources Research*, *38*(12), Article 12.

Veneziano, D., & Langousis, A. (2010). Scaling and Fractals in Hydrology. In B. Sivakumar & R. Berndtsson, *Advances in Data-Based Approaches for Hydrologic Modeling and Forecasting* (pp. 107–243). World Scientific.

Vu, M., Raghavan, V., & Liong, S.-Y. (2017). Deriving short-duration rainfall IDF curves from a regional climate model. *Natural Hazards*, *85*(3), Article 3.

Wang, B., Zhang, M., Wei, J., Wang, S., Li, S., Ma, Q., Li, X., & Pan, S. (2013). Changes in extreme events of temperature and precipitation over Xinjiang, northwest China, during 1960–2009. *Zanzibar to the Yellow Sea: A Transect of Quaternary Studies from 6°S, 39°E to 35°N, 127°E*, *298*, 141–151.

Wang, H., & Chen, Q. (2014). Impact of climate change heating and cooling energy use in buildings in the United States. *Energy and Buildings*, *82*, 428–436.

Wang, L., & Chen, W. (2014). Equiratio cumulative distribution function matching as an improvement to the equidistant approach in bias correction of precipitation. *Atmospheric Science Letters*, *15*(1), 1–6.

Wey, K. M. (2006). *Temporal Disaggregation of Daily Precipitation Data in a Changing Climate*. 178.

Willems, P. (2013). Revision of urban drainage design rules after assessment of climate change impacts on precipitation extremes at Uccle, Belgium. *Journal of Hydrology*, *496*, 166–177.

Wood, A. W., Leung, L. R., Sridhar, V., & Lettenmaier, D. (2004). Hydrologic implications of dynamical and statistical approaches to downscaling climate model outputs. *Climatic Change*, *62*(1), 189–216.

Wood, A. W., Maurer, E. P., Kumar, A., & Lettenmaier, D. P. (2002). Long-range experimental hydrologic forecasting for the eastern United States. *Journal of Geophysical Research: Atmospheres*, *107*(D20), ACL-6.

Yu, P.-S., Yang, T.-C., & Lin, C.-S. (2004). Regional rainfall intensity formulas based on scaling property of rainfall. *Journal of Hydrology*, *295*(1–4), Article 1–4.

Chapter 3. Assessment and Improvement of IDF Generation Algorithms Used in IDF_CC Tool

3.1 Abstract:

Climate change will modify the spatio-temporal variation of hydrological variables worldwide, potentially leading to more extreme events and hydraulic infrastructure failures. Changes in extreme sub-daily precipitation must be accounted for in urban infrastructure planning and management; hence in intensity-duration-frequency (IDF) curves which represent the primary climatic input to urban water infrastructure design. The IDF_CC tool is a computerized tool for developing IDF curves under a changing climate that is widely used in adaptation studies, particularly in Canada. Earlier versions of the tool generate IDF curves using equidistant quantile mapping (EQM), while the latest version uses quantile delta mapping (QDM). In this study, we critically assess both algorithms to propose new and improved versions and compare their performance to the original algorithms at four locations in Eastern Ontario, Canada. In total, 3,600 simulated precipitation intensity series of the control (1976–2005) and future (2011–2100) periods under the RCP 4.5 and RCP 8.5 climate scenarios derived from four global climate models (GCMs) and four regional climate models (RCMs) were analyzed. The original EQM method was found to be insensitive to the climate change signal whereas the original QDM used an inadequate mapping function between quantiles of observed and RCM-simulated precipitation time series, leading to misrepresentations of future climate conditions. In general, the new versions outperformed the original versions and showed consistent projections, hence providing better inputs for adaptation assessments.

***Keywords*:** Climate change; IDF generation; IDF_CC tool; EQM; QDM; Climate sensitivity, Quantile mapping algorithms.

***** This chapter has been published in the journal of *Water Resources Management* as "Alzahrani, F., Seidou, O. & Alodah, A. Assessment and Improvement of IDF Generation Algorithms Used in the IDF_CC Tool. Water Resour Manage 36, 4591–4606 (2022). https://doi.org/10.1007/s11269-022-03265-3. "

3.2 Introduction

Climate change is expected to alter the temporal variability of precipitation at all timescales, including sub-daily, short-duration storms which are routinely used in the design of stormwater systems, road drainage, pond design, flood control, and water-quality control systems (Westra *et al.*, 2014; Chin, 2017). At the same time, there is considerable uncertainty about how hydrological variables will change in the future (S1). Uncertainties are higher at shorter timescales (Johnson and Sharma, 2012; Fatichi *et al.*, 2013; Scoccimarro *et al.*, 2015; Noor *et al.*, 2018; Dahm *et al.*, 2019), e.g., the climate change signal (CCS), defined as a persistent change in the climate regime due to greenhouse gas emissions, is more robust in simulated annual time series than in daily or hourly ones (Najafi *et al.*, 2012). Accurate estimation of the CCS is critical for devising adaptation strategies and planning (Ehret *et al.*, 2012; Hempel *et al.*, 2013).

Extreme precipitation events at sub-daily time scales are often represented using intensity-frequency-duration (IDF) curves, which relate precipitation duration and average precipitation intensity to the return period/frequency. Numerous studies have reported trends showing increased rainfall intensities across the world (Min *et al.*, 2011; Westra *et al.*, 2013; 2014; Kendon *et al.*, 2019; Martel *et al.*, 2021), including a 12% average rise in annual precipitation across Canada between 1950 and 2006 (Ligeti *et al.*, 2006; Shephard *et al.*, 2014). According to the Intergovernmental Panel on Climate Change (IPCC), the number of extreme precipitation events has risen globally in the last century (IPCC, 2013).

There is a consensus that global warming will lead to higher precipitation intensities for given return periods and to shorter return periods for given intensities (Westra *et al.,* 2013; Dore 2005; IPCC 2007; Kuo *et al.,* 2015), and that past estimates of the severity and frequency of extreme events will no longer be valid in the future (Adamowski and Bougadis 2003; Vavrus and Van Dorn 2010; Burn and Taleghani 2013; Sillmann *et al.,* 2013; Fischer *et al.,* 2021; Tatli 2021). From the Clausius-Clapeyron relationship, we know that extreme precipitation events will become more frequent under climate change as a warmer atmosphere can hold more water (Allen and Ingram 2002; Ingram 2016; Tabari 2020), although the changes will vary regionally according to local atmospheric dynamics (Zhang *et al.,* 2017; Norris *et al.,* 2019; Li *et al.,* 2019; Tabari 2020). Therefore, existing IDF curves, constructed based on past records, may not be valid for future scenarios and need updating (Yeo *et al.,*2022; Arfa *et al.,* 2021; Szeląg *et al.,* 2021; Shukor *et al.,* 2020; Adamowski *et al.,* 2010).

The techniques used to generate IDF curves under climate change include *i*) the Delta-Change method (DC) (e.g., Sunyer *et al.,* 2015; Requena *et al.* 2021), *ii*) quantile-based algorithms such as equidistant quantile mapping (EQM) and quantile delta mapping (QDM) (e.g., Hassanzadeh *et al.,* 2014; Kuo *et al.,* 2015; Singh *et al.*, 2016; Switzman *et al.,* 2017; Dau *et al.,* 2021; Şen & Kahya 2021), *iii*) techniques using temporal disaggregation of projected daily precipitation (e.g., Wang *et al.* 2013; Uraba *et al.* 2019), and *iv*) approaches based on scale invariance theory (e.g., Veneziano and Furcolo 2002; Langousis and Veneziano 2007; Innocenti *et al.* 2017). The linear DC method, although popular due to its simplicity (Kuo *et al.* 2015; Switzman *et al.* 2017; Wang *et al.* 2013; Rodriguez *et al.* 2014; Seidou and Alodah 2018; Alodah and Seidou 2019), employs the same temporal variabilities derived from past climate to future climate projections, which is unrealistic (Alodah and Seidou 2019). While EQM is an improved version of the traditional quantile mapping algorithm (Li *et al.,* 2010) in that it corrects the cumulative distribution function (CDF) of the future period (projections), QDM is a combination of the quantile mapping and delta change methods that conserves relative differences in precipitation quantiles (Cannon *et al.* 2015). Both methods have been shown to produce better agreement between the probability distribution functions (PDFs) of the corrected and observed time series compared to traditional QM (Cannon *et al.* 2015). IDF curves can also be generated by temporally downscaling projected daily precipitation time series. For instance, Mirhosseini *et al.* (2014) first projected daily precipitation from 2070 to 2100 using EQM before downscaling those projections to 3h timesteps using artificial neural networks while Wang *et al.* (2013) applied the downscaling before projecting extreme events. Uraba *et al.* (2019) used a stochastic weather generator (LARS-WG) to spatially downscale daily time series before applying K- nearest neighbours (KNN) disaggregation to downscale the daily data to an hourly scale. Scale invariance theory (simple scaling) can be used to temporally disaggregate daily precipitation and derive IDF (Veneziano and Furcolo 2002; Innocenti *et al.* 2017).

The IDF_CC tool is a free web-based platform to create IDF curves for future climate regimes in Canada using data from over 800 Canadian weather stations and corrected outputs from 24 global circulation models (GCMs) that simulate different climate conditions and local precipitation data (https://www.idf-cc-uwo.ca/; Simonovic, 2017). It is intended to assist local decision-makers, without any expertise in climate modeling, to select appropriate climate change adaptation options.

While earlier versions of the IDF_CC tool used EQM (Srivastav *et al.,* 2014), versions from 3.5.0 onward employ the QDM algorithm (Schardong *et al.*, 2020) which assumes that both the observed and historical GCM-simulated annual maximum precipitation (AMP) time series follow a Gumbel distribution as is most suitable for extreme value events, while GEV distribution is fitted to historical and future AMP time series.

Despite significant differences between both algorithms, no critical comparison has been performed. Here, we *a)* critically review the EQM and QDM algorithms and propose possible improvements; *b)* assess whether observations are better represented by a GEV or Gumbel distribution; *c)* examine whether the distribution type affects the performance of the algorithms; and *d)* test which algorithm yields more consistent projections.

3.3 Materials and Methods

3.3.1 Watershed and Data Description

We test our approach on the South Nation watershed (approximately 4000 km^2), located southeast of Ottawa in Eastern Ontario, Canada (Figure S1). Its main river is the South Nation River with a length of 175 km on relatively flat topography. Historical data of hourly precipitation were acquired from Environment Canada for the years 1976-2005 (Table S1). We obtained daily precipitation time series generated by four RCMs for the years 1976-2100 from the Coordinated Regional Climate Downscaling Experiment (NA-CORDEX) data portal. The RCMs were used to dynamically downscale the outputs of four GCMS as part of the fifth phase of the Coupled Model Inter-comparison Project (CMIP5) (Table S2). GCM simulations were run under Representative Concentration Pathway scenarios (RCP) RCP 4.5 and RCP 8.5, at a resolution of approximately 50 km. The 1976–2005 period serves as reference period. Future periods include 2011-2039 (short term), 2041-2069 (medium term), and 2071-2100 (long term).

3.3.2 Original IDF_CC algorithms

While earlier versions of the IDF_CC tool used EQM algorithm (Srivastav *et al.,* 2014), versions starting with 5.0 employ the QDM algorithm (Schardong *et al.,* 2020) (see Section 2 in the Supplementary Materials in the appendix A for a detailed description). Only the equations with issues are presented here.

3.3.3 Definitions and notations

EQM_o: original equidistant quantile mapping algorithm

EQM_m: modified equidistant quantile mapping algorithm

QDM_o: original quantile delta mapping algorithm

QDM_m: modified quantile delta mapping algorithm

X_{max}^{GCM}: maximum daily precipitation extracted from GCM of historical period

$X_{max,j}^{STN,Fut}$: future maximum sub-daily precipitation at station *j*.

$Y_{max}^{GCM,Fut}$: corrected GCM sub-daily series

$Y_{max,j}^{STN}$: corrected GCM sub-daily precipitation series at station *j*.

Θ is the fitting distribution parameter.

3.3.4 Flaws in the original EQM IDF_CC algorithm

There are several problems with the EQM_o method. If we consider these equations

$$\boldsymbol{Y_{max,j}^{STN}}\boldsymbol{=CDF((invCDF(\frac{X_{max}^{GCM}}{\theta^{GCM}}))/\theta^{STN,j})} \quad \text{(S4)}$$

$$\boldsymbol{Y_{max}^{GCM,Fut} = CDF\left(\left(invCDF\left(\frac{X_{max}^{GCM}}{\theta^{GCM}}\right)\right)/\theta^{GCM,Fut}\right)} \quad \text{(S5)}$$

(Eqs. S4 and S5, respectively, Supplementary Materials) we notice that the cumulative distribution function (CDF) and the inverse CDF (*invCDF* or *ICDF*) are inverted because *CDF* ranges are between 0 and 1; moreover, both equations lead to hydrological (precipitation time series) variables between 0 and 1.

Furthermore, in Equations S7, S9 and S10 (Supplementary Materials in the appendix A) of the EQM_o algorithm, linear equations are used to link observed and modelled time series:

$$\boldsymbol{Y_{max,j}^{STN}=a_1 \times X_{max}^{GCM} + b_1} \quad \text{(S7)}$$

$$\boldsymbol{Y_{max}^{GCM,Fut}=a_2 \times X_{max}^{GCM} + b_2} \quad \text{(S9)}$$

$$\boldsymbol{X_{max,j}^{STN,Fut}=a_1 \times \left[\frac{X_{max}^{GCM,Fut} - b_2}{a_2}\right] + b_1} \quad \text{(S10)}$$

where a_1, a_2, b_1 and b_2 are linear equation coefficients. The linear relationship between $\boldsymbol{Y_{max,j}^{STN}}$ and $\boldsymbol{X_{max}^{GCM}}$ in Eq.(S7) is problematic as the relationship between natural variables is generally nonlinear. In addition, Eq.(S7) is redundant because it is already contained in Eq.(S4) in a nonlinear form.

The biggest flaw in the method is Equation (S9) where it is assumed that a_2 will represent any increase or decrease in the climate signal resulting from climate change. Hence, the term $\left[\frac{X_{max}^{GCM,Fut} - b_2}{a_2}\right]$ in Equation (S10) **effectively cancels** the climate change signal contained in future GCM outputs as $\boldsymbol{X_{max,j}^{STN,Fut}=a_1\times}\left[\frac{X_{max}^{GCM,Fut}-b_2}{a_2}\right]$ $\boldsymbol{+\,b_1}$ will always have the same range of values as $\boldsymbol{Y_{max,j}^{STN}=a_1\times X_{max}^{GCM}+b_1}$.

Finally, Eq.(S7) assumes that observed and GCM-simulated time series **are synchronized in time**. However, the output from climate models does not necessarily coincide with the times for which we have *in situ* measurements, and we can only expect them to have similar distributions. Thus, observations and simulations cannot be linked by a linear equation.

3.3.5 Flaws in the QDM method

Equation (S11) (Supplementary Materials) links the quantiles of annual maxima precipitation at the station scale to model-derived quantiles:

$$\hat{x}_{j,o,h}=\frac{a_j+x_{m,h}}{b_j+c_j x_{m,h}}+\frac{d_j}{x_{m,h}} \tag{S11}$$

This equation is not monotonous and not continuously derivable which may pose a problem for specific optimization algorithms as seen in Fig. 3.2. Obviously, a simple polynomial or empirical mapping function would be better.

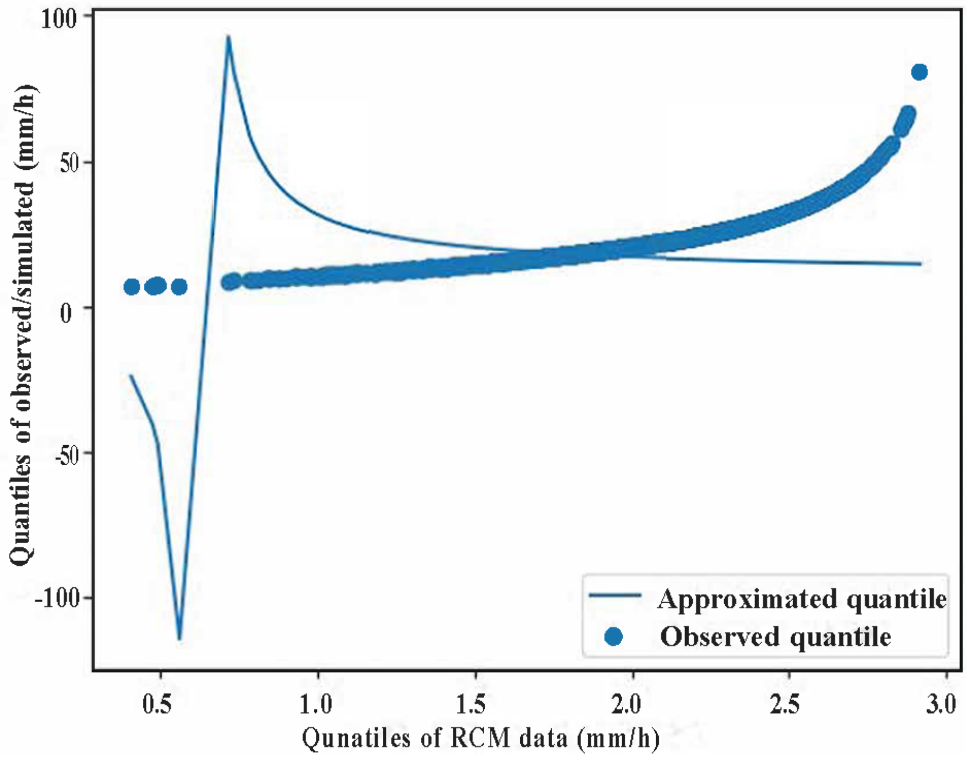

Figure 3.1 Unsuccessful fit of the original equation proposed by Schardong *et al.* (2020) (Eq. S11) using quantiles of precipitation simulated with CanESM2.CanRCM4 and quantiles of observation.

3.4 Improvements of IDF_CC algorithms

3.4.1 Improvements to the EQM method

As a first step, we can replace the actual time series in Eq.(S7) with the sorted one:

$$\left(Y_{max,j}^{STN}\right)_{sorted} = a_1 \times \left(X_{max}^{GCM}\right)_{sorted} + b_1 \qquad \text{Eq(3.}$$

which resolves the non-synchronization issue between GCMs and observations. Furthermore, in Eq.(S10) we can remove the part that cancels the climate change signal:

$$\left(X_{max,j}^{STN,Fut}\right)_{sorted} = a_1 \times \left(X_{max}^{GCM,Fut}\right)_{sorted} + b_1 \qquad \text{Eq(3.}$$

The second possible improvement to the EQM method solves the synchronization issue and the climate change signal cancellation issue. To resolve the issue related to the assumed linear relationship between GCM and observations (Eq.S4), we could simply remove Eqs.(S5-S10) altogether and calculate $X_{max}^{GCM,Fut}$ using:

$$X_{max,j}^{STN}=CDF\left(\left(invCDF\left(X_{max}^{GCM,fut}|\theta^{GCM}\right)\right)|\theta^{STN,j}\right) \qquad \text{Eq (3.3)}$$

which would accommodate non-linear relationships between quantiles in the current and future climate.

3.4.2 Improvement to the QDM algorithm

To improve the QDM approach we propose to replace Eq.(S11) by an empirical mapping function based on the quantiles of the RCM outputs and the quantiles of the observations:

$$F_{j,o,h}^{-1}\left(F_{m,h}^{-1}(x_{m,h})\right) \qquad \text{Eq (3.4)}$$

where $F^{-1}_{j,o,h}$ is the inverse CDF of the observed annual maximum precipitation, $F^{-1}_{m,h}$ the inverse CDF of climate model of historical period, and $x_{m,h}$ the annual maximum precipitation of climate change model for the historical period.

3.5 Assessment of model performance

The performance of the investigated methods is assessed using three different approaches:

1. a numerical experiment to test whether the EQM_o indeed ignores the climate change signal;

2. split-sample validation using the two-sample Kolmogorov-Smirnov (KS) test to examine whether the simulated and observed annual maxima have similar distributions for durations of 1h to 24h; and

3. two-by-two comparisons of these distributions to test for discrepancies.

3.5.1 Sensitivity to future climate signal

In section 2.3.2, we have hypothesized that, given the way EQM_o was formulated, it is insensitive to the climate signal. In order to demonstrate that, we devised a simple experiment in which we multiply the climate model output for the future period ($X_{max}^{GCM,fut}$) by an arbitrary factor of 1.5. If the EQM_o is sensitive to the climate change signal the resulting projection of annual maxima should increase noticeably. However, if the projected sub-daily time series should remain unchanged, then this would confirm our hypothesis that the EQM_o is indeed insensitive to the climate change signal (long-term trend) and should therefore not be used in adaptations studies.

3.5.2 Split-sample calibration and validation

Here, we split the historical data into calibration and validation periods and use the two-sample Kolmogorov-Smirnov (KS) test to compare the empirical cumulative distributions of the simulated and observed data sets. To avoid bias, the calibration data set contains all even years while the odd years are assigned to the validation data set instead splitting the time series into two portions. The KS test is based on the following $D_{m,n}$ statistic:

$$D_{m,n}=|F_n^1(x)-F_n^2(x)| \qquad \text{Eq (3.5)}$$

F^1 and F^2 are the CDF of the observed and simulated precipitation, respectively, while *m* and *n* are the number of data samples. There are two null hypotheses in the KS test, H_0 and H_1, which represent the acceptance or rejection of the test, respectively. $D_{m,n}$ is the maximum distance between the CDF curves of observed and simulated data. The *critical* value is calculated from the Kolmogorov distribution using:

$$D_{m,n,\alpha}=c(\alpha)\sqrt{\frac{m+n}{mn}} \qquad \text{Eq (3.6)}$$

where the c(α) is the critical value obtained from the KS distribution table. If $D_{m,n,\alpha}$ is more significant than $D_{m,n}$, then H_0 is accepted and both samples are similar. If $D_{m,n}$ is significantly larger than $D_{m,n,\alpha}$ then the null hypothesis is rejected.

3.5.3 Assessing the coherence between IDF generation methods

The KS test will be used to compare the probability distributions of the annual maxima as generated by the different algorithms for both the calibration and validation periods. Depending on how often two different approaches produce the same distribution we can assess how similar they are.

3.6 Results and Discussion

3.6.1 Comparison of the original and improved EQM method

Using Russell station as a representative example (other stations showed similar trends), the dotted red lines are drawn based on the data's maximum and minimum values. the annual maxima time series exhibit an increase in both magnitude and variance for event durations of 1h and 24h (Figs. 3.2, S3 in appendix A). However, the change is much more pronounced in the EQM_m. Overall, the EQM_o produced means and variances that are very similar to those of the observations for short and med term future periods. In contrast, the EQM_m yielded an increasing trend in the med and long terms, although its magnitude depends on the climate model. For instance, when applied to the CanESM2RCM4 model output, both EQM approaches are almost indistinguishable (Figs. 3.2 and S3, lower left panel). With the EC-Earth RCA4 model, the EQM_m yields higher values for both 1h and 24h event durations. Furthermore, the EQM_o yields time series that are significantly closer (in terms of mean and variance) to the observed time series, suggesting that it may not be able to capture the climate change signal.

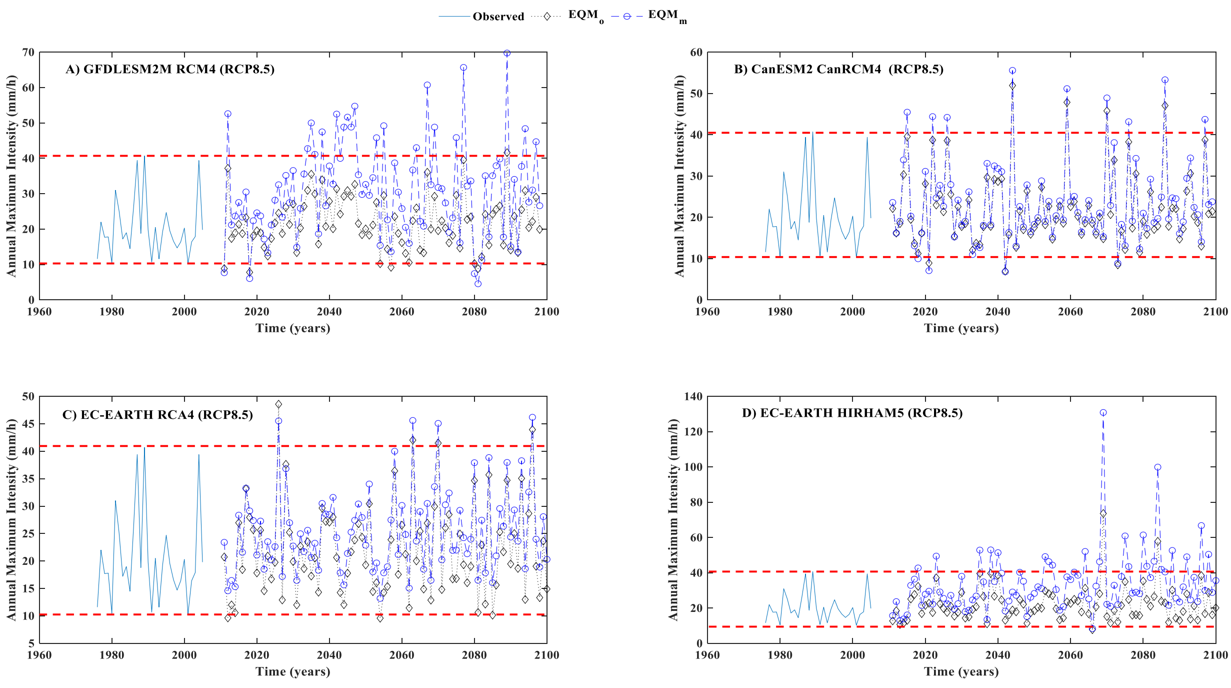

Figure 3.2 Differences between EQM_o and EQM_m at Russell station for the 1h precipitation datasets using scenario RCP 8.5 to force different climate models: A) GFDLESM2M RCM4, B) CanESM2 CanRCM4, C) EC-EARTH RCA4, and D) EC-EARTH HIRHAM5.

To test our hypothesis that the EQM_o is insensitive to the climate change signal (cf., Section 3.4.2), we multiplied the RCM outputs for future periods by an arbitrary factor of 1.5 and re-applied both the EQM_o and EQM_m. As a result, the EQM_m yielded increasing projections while the EQM_o produced the same output as before (Fig. 3.3), thus confirming our original hypothesis.

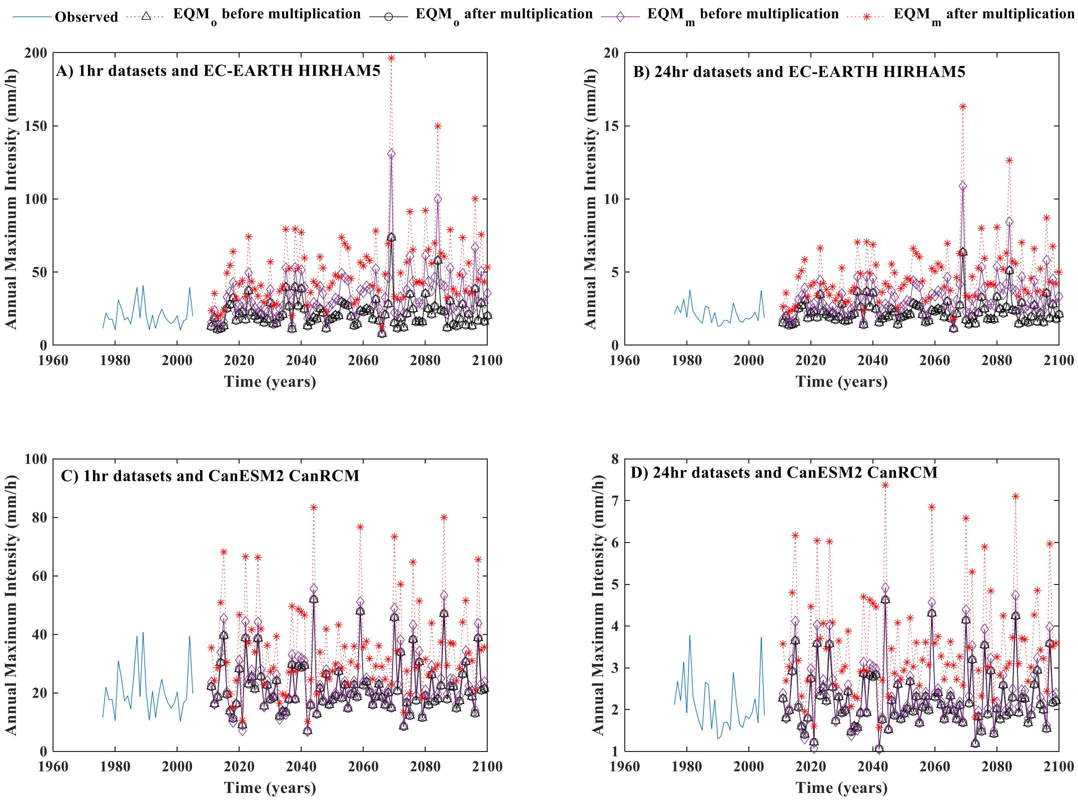

Figure 3.3 Evaluation of the effect of multiplying GCM (RCP 8.5) outputs for the future period at Russell station by 1.5 using: A) 1hr datasets and EC-EARTH HIRHAM5, B) 24hr datasets and EC-EARTH HIRHAM5, C) 1hr datasets and CanESM2 CanRCM, and D) 24hr datasets and CanESM2 CanRCM.

3.6.2 Split-sample calibration and validation results

Based on the two-sample KS test for precipitation durations of 1h and 24h at Russell station, the null hypothesis (the two samples are from the same distribution) was accepted in calibration for all methods and durations (Table 3.1). The null hypothesis was also accepted for all models and durations for EQM_o and EQM_m. The QDM_m slightly outperform QDM_o in terms of number of rejections in the validation period (2 versus 3, respectively) and minimum p value (0.05 versus 0.01, respectively). EQM_m has the highest minimum p-value (0.59) and no rejection in the validation period, making it the best overall.

Table 3.1 Results of the two-sample Kolmogorov-Smirnov test for different models and precipitation durations of 1h and 24h at Russell station. Significance: p≤0.05; the null hypothesis (two samples are from the same distribution) is accepted when p>0.1.

Experiment	Duration (hr)	EQM_o, Calibration	EQM_o, Validation	EQM_m, Calibration	EQM_m, Validation	QDM_o Calibration	QDM_o Validation	QDM Calibrat
CanESM2 CanRCM4 RCP 85	1h	Accepted (p=0.89)	Accepted (p=0.59)	Accepted (p=0.89)	Accepted (p=0.59)	Accepted (p=0.9)	Accepted (p=0.99)	Accept (p=0.9
	24h	Accepted (p=0.89)	Accepted (p=0.89)	Accepted (p=0.89)	Accepted (p=0.59)	Accepted (p=0.9)	Accepted (p=0.64)	Accept (p=0.7
EC-EARTH RCA4 RCP 85	1h	Accepted (p=0.59)	Accepted (p=0.051)	Accepted (p=0.59)	Accepted (p=0.89)	Accepted (p=0.9)	Rejected (p=0.01)	Accept (p=0.9
	24h	Accepted (p=0.89)	Accepted (p=0.31)	Accepted (p=0.89)	Accepted (p=0.59)	Accepted (p=0.7)	Rejected (p=0.1)	Accept (p=0.7
EC-EARTH HIRHAM5 RCP 85	1-h	Accepted (p=0.89)	Accepted (p=0.59)	Accepted (p=0.89)	Accepted (p=0.59)	Accepted (p=0.9)	Accepted (p=0.2)	Accept (p=0.9
	24h	Accepted (p=0.59)	Accepted (p=0.59)	Accepted (p=0.59)	Accepted (p=0.59)	Accepted (p=0.9)	Rejected (p=0.02)	Accept (p=0.9
GFDLESM2MReg CM4 RCP 85	1h	Accepted (p=0.99)	Accepted (p=0.86)	Accepted (p=0.99)	Accepted (p=0.86)	Accepted (p=0.9)	Accepted (p=0.7)	Accept (p=0.9
	24h	Accepted (p=0.89)	Accepted (p=0.86)	Accepted (p=0.89)	Accepted (p=0.86)	Accepted (p=0.9)	Accepted (p=0.3)	Accept (p=0.9
Minimum p-value	1h	0.59	0.1	0.59	0.59	0.9	0.01	0.9
	24h	**0.59**	**0.31**	**0.59**	**0.59**	**0.7**	**0.02**	**0.7**

The distribution of AMP generated with each method were systematically compared to the corresponding distribution of the observed datasets for durations ranging from 1h to 24h in 1h intervals using the KS test (Table 3.2). The null hypothesis was accepted for the calibration period and both the EQM_o and EQM_m methods, as well as for the QDM_m method. There is a 12% rejection rate of the QDM_o method for the calibration period (25% at Morrisburg, 4% at Russel, 5% at South Mountain, and 15% at St. Albert). Based on these results, the QDM_o performed worst while the QDM_m is the best (in the validation period). Considering that the EQM_o cannot account for the climate change signal, it should be considered even worse than the QDM_o which makes it the worst overall.

Table 3.2 Percentage of similarity between observed and downscaled AMP, calibration, and validation periods.

Method		Station				
		All stations	Morrisburg	Russell	South Mountain	St. Albert
EQM_o	*Calibration*	100%	100%	100%	100%	100%
	Validation	**98%**	**100%**	**99%**	**94%**	**100%**
EQM_m	*Calibration*	100%	100%	100%	100%	100%
	Validation	**83%**	**98%**	**64%**	**69%**	**100%**
QDM_o	*Calibration*	88%	75%	96%	95%	86%
	Validation	**76%**	**73%**	**74%**	**68%**	**88%**
QDM_m	*Calibration*	100%	100%	100%	100%	100%
	Validation	**87%**	**94%**	**81%**	**75%**	**98%**

3.6.3 Coherence of the distributions of the downscaled annual maxima between downscaling methods

The KS test is used to make pairwise comparisons of the distributions of the annual maxima time series for durations ranging from 1h to 24h in 1h increments and all periods (calibration, validation, short-term, medium-term, and long-term) with non-rejection rates presented in Tables 3.3 (all stations) and S3 (individual stations). Non-rejection rates range from 100% to 50%, although for some cases they are as low as 0%, especially for long-term projections.

The EQM_m and QDM_m are systematically coherent with each other (100% non-rejection of the null hypothesis in all periods). The EQM_o, EQM_m, and QDM_m are systematically coherent in the historical and the future short-term periods. In contrast, the QDM_o stands apart in these periods with a 75% non-rejection rate of the null hypothesis compared to all other methods.

The original method increasingly diverges from the modified ones as one looks forward. The non-rejection rate of the QDM_o is only 50% compared to the modified methods in the medium and long-term. The non-rejection rate of the EQM_o goes from 75% to 0% compared to the EQM_m. It goes from 75% to 50% compared to the QDM_m.

3.6.4 Comparison of IDF curves generated using different methods

A comparison of IDF curves generated with all methods shows that results can vary greatly depending on the method (Figs 3.4 and S4 to S8). Some of the IDF curves generated using the QDM_o method were not smooth because of the issue of fitting a monotonic function (relation between quantiles) using a non monotonic function (equation S11 These results indicate that the choice of the downscaling method is likely to have a significant impact on the projected design intensities, hence on the selection of the climate change adaptation strategies.

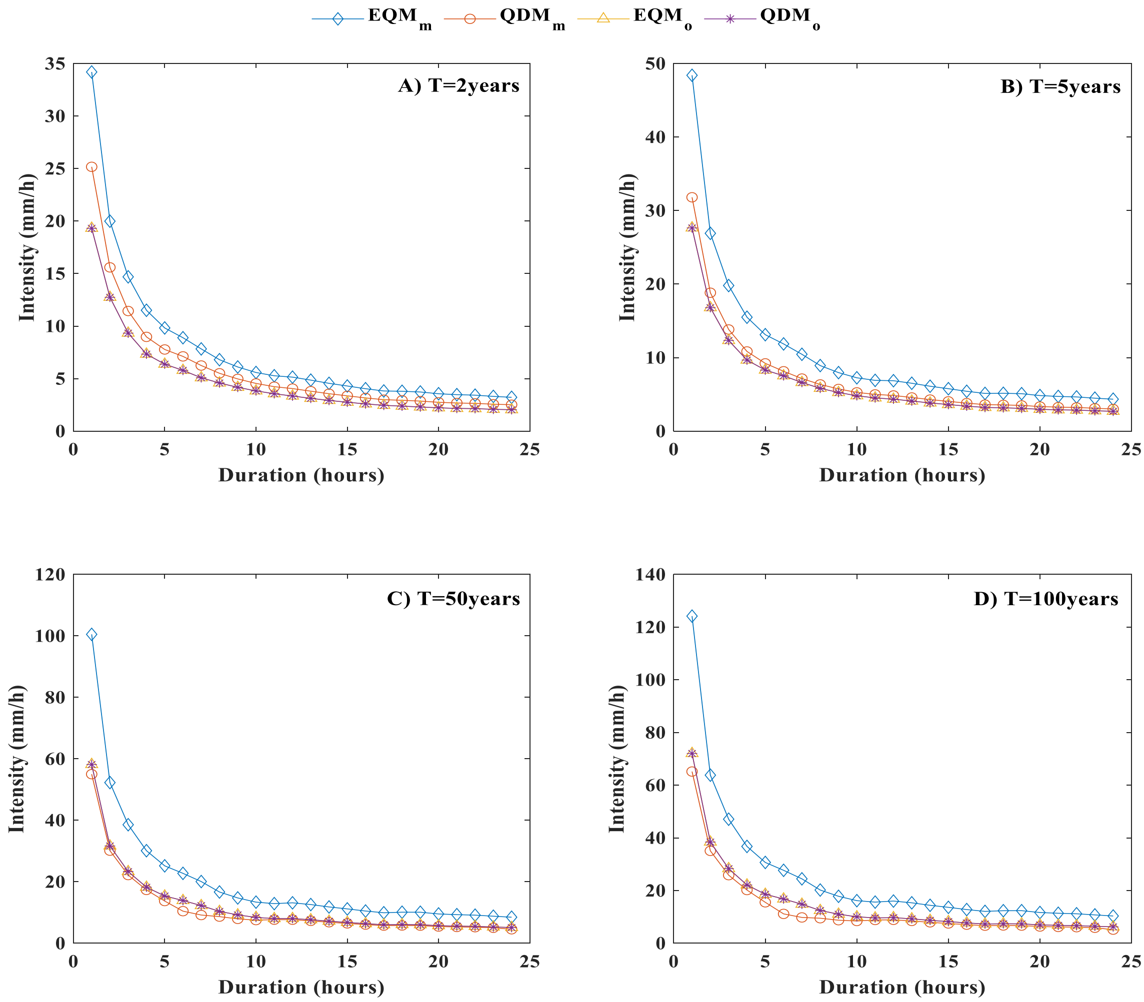

Figure 3.4 IDF curves generated for the period 2071-2100 at Russel station using model EC-EARTH HIRHAM 5 RCP8.5 and return periods of A) T=2years, B) T=5years, C) T=50years, and D) T=100years.

Table 3.3 Percentage of similarity between downscaled annual maxima for all periods.

Period		Method	Downscaling method EQM_m	QDM_m	EQM_o	QDM_o
Historical	Calibration	EQM_m	100%	**100%**	100%	75%
		QDM_m	**100%**	100%	100%	75%
		EQM_o	100%	100%	100%	75%
		QDM_o	75%	75%	75%	100%
	Validation	EQM_m	100%	**100%**	100%	75%
		QDM_m	**100%**	100%	100%	75%
		EQM_o	100%	100%	100%	75%
		QDM_o	75%	75%	75%	100%
Future	Short-term	EQM_m	100%	**100%**	100%	50%
		QDM_m	**100%**	100%	100%	75%
		EQM_o	100%	100%	100%	50%
		QDM_o	50%	75%	50%	100%
	Med-term	EQM_m	100%	**100%**	75%	50%
		QDM_m	**100%**	100%	75%	50%
		EQM_o	75%	75%	100%	50%
		QDM_o	50%	50%	50%	100%
	Long-term	EQM_m	100%	**100%**	0%	50%
		QDM_m	**100%**	100%	50%	50%
		EQM_o	0%	50%	100%	0%
		QDM_o	50%	50%	0%	100%

3.7 Discussion

Urban water infrastructures play a critical role in preventing floods and ensuring the well-being of the population in case of extreme precipitation. They are typically designed for a specific return period specified by local guidelines. There is more and more evidence that climate regimes will be shifting in the future, and that the performance and safety of existing infrastructures will change. It is therefore critical to anticipate these changes to upgrade existing infrastructure elements and properly design the ones that will be built in the future. Some Canadian municipalities use IDF_CC tool, an IDF generation software which used EQM_o then QDM_o as an IDF generation method. In this work, we critically assessed both methods and exposed several flaws in both algorithms. The EQM_o method appears unable to account for changes in the climate change signal, causing it to underestimate the impact of climate change on IDF curves. We proposed several fixes that resulted in two modified versions: EQM_m and QDM_m. In the pilot case study presented above, the distributions of maxima series obtained with EQM_o systematically deviated from other distributions, especially in the long-term. It was also demonstrated that the QDM_o method generates time series that often have different distributions compared to observations, even in the calibration period. This is due to the mapping function applied to the quantiles of the distributions of observed and GCM data (step 4 in the QDM algorithm, Eq. [S11]).

Given that the IDF_CC tool is widely used by municipalities and stakeholders in Canada to devise adaptation policies, the flaws exposed here may lead to serious misjudgments. Many local climate change assessments are based on the EQM_o and QDM_o algorithms to devise water resource management practices, e.g., projections of floodplain extents of the Riviere Des Prairies Basin, Quebec, Canada (Batchabani *et al.*, 2016), predictions of changing precipitation intensities for urban stormwater planning in Canada (Senior *et al.*, 2019; Kaykhosravi *et al.*, 2020) and China (Wang *et al.*, 2019), or devising general adaptation strategies to climate change (Sandink *et al.*, 2016; Wellstead *et al.*, 2016). Considering the potential implications of changing extreme precipitation patterns, all results generated using the original algorithms should be interpreted with caution. Still, the IDF_CC tool provides an innovative approach to support the decision-making process, particularly for professionals, engineers, and stakeholders as it allows them to produce updated IDF estimates based the most up-to-date local datasets, particularly for ungauged locations, and incorporating updated regional climate models.

3.8 Conclusions

Possible errors in estimations of future extreme sub-daily precipitation events, particularly IDF curves, could lead to ill-suited adaptation strategies and a higher risk of failure of water management infrastructures. IDF curves are based on sub-daily precipitation intensities, whose changes are more difficult to predict than those of daily, monthly, and annual precipitation. In this paper, we assessed the accuracy of the two IDF generation algorithms used in the web-based IDF_CC tool (EQM_o and QDM_o) and identified areas for improvement. A critical flaw was found in the EQM_o method which prevents it from accurately accounting for changes in the climate change signal. The performance of the EQM_o, QDM_o, EQM_m, and QDM_m was assessed by testing the similarity of the annual maxima generated by each method in the historical periods. The four methods were applied to four stations in Eastern Ontario, and the results were compared for the historical period (1976 –2006), the short-term (2011–2040), the medium-term (2041–2070), and the long-term (2071–2100). The best method was the QDM_m, while the QDM_o fared poorly regarding the similarity of distributions and the EQM_o could not capture the climate change signal. It was also shown that the modified versions (EQM_m and QDM_m) are more consistent with each other in future periods compared to the original versions. These findings should be highly useful for incorporating projected changes in derived climate information (IDF curves) as the basis for planning, design, and management in various water engineering applications.

3.9 References

Adamowski, J., Adamowski, K., & Bougadis, J. (2010). Influence of trend on short duration design storms. Water Resources Management, 24(3), 401-413.

Adamowski, K.; Bougadis, J. Detection of Trends in Annual Extreme Rainfall. Hydrological Processes 2003, 17 (18), 3547–3560.

Allen, M. R., & Ingram, W. J. (2002). Constraints on future changes in climate and the hydrologic cycle. Nature, 419(6903), 228-232.

Alodah, A.; Seidou, O. Assessment of Climate Change Impacts on Extreme High and Low Flows: An Improved Bottom-Up Ap-proach. Water 2019, 11 (6).

Arfa, S., Nasseri, M., & Tavakol-Davani, H. (2021). Comparing the effects of different daily and sub-daily downscaling approaches on the response of urban stormwater collection systems. Water Resources Management, 35(2), 505-533.

Batchabani, E., Sormain, E., & Fuamba, M. (2016). Potential impacts of projected climate change on flooding in the Riviere des Prairies basin, Quebec, Canada: One-dimensional and two-dimensional simulation-based approach. Journal of Hydrologic Engineering, 21(12), 05016032.

Burn, D. H.; Taleghani, A. Estimates of Changes in Design Rainfall Values for Canada. Hydrological Processes 2013, 27 (11), 1590–1599.

Cannon, A. J.; Sobie, S. R.; Murdock, T. Q. Bias Correction of GCM Precipitation by Quantile Mapping: How Well Do Methods Preserve Changes in Quantiles and Extremes? Journal of Climate 2015, 28 (17), 6938–6959.

Chin, D. A. (2017). Designing bioretention areas for stormwater management. Environmental Processes, 4(1), 1-13.

Dahm, R., Bhardwaj, A., Sperna Weiland, F., Corzo, G., & Bouwer, L. M. (2019). A temperature-scaling approach for projecting changes in short duration rainfall extremes from GCM data. Water, 11(2), 313.

Dau, Q. V., Kuntiyawichai, K., & Adeloye, A. J. (2021). Future changes in water availability due to climate change projections for Huong Basin, Vietnam. Environmental Processes, 8(1), 77-98.

Dore, M. H. Climate Change and Changes in Global Precipitation Patterns: What Do We Know? Environment international 2005, 31 (8), 1167–1181.

Ehret, U., Zehe, E., Wulfmeyer, V., & Liebert, J. (2012). Should we apply bias correction to global and regional climate model data? Hydrol. Earth Syst. Sci., 16, 3391–3404.

Fatichi, S., Ivanov, V. Y., & Caporali, E. (2013). Assessment of a stochastic downscaling methodology in generating an ensemble of hourly future climate time series. Climate Dynamics, 40(7-8), 1841-1861.

Fischer, E. M., Sippel, S., & Knutti, R. (2021). Increasing probability of record-shattering climate extremes. Nature Climate Change, 11(8), 689-695.

Ganguli, P.; Coulibaly, P. Assessment of Future Changes in Intensity-Duration-Frequency Curves for Southern Ontario Using North American (NA)-CORDEX Models with Nonstationary Methods. Journal of Hydrology: Regional Studies 2019, 22, 100587–100587.

Hassanzadeh, E., Nazemi, A., & Elshorbagy, A. (2014). Quantile-based downscaling of precipitation using genetic programming: Application to IDF curves in Saskatoon. Journal of Hydrologic Engineering, 19(5), 943-955.

Ingram, W. (2016). Increases all round. Nature Climate Change, 6(5), 443-444.

Innocenti, S.; Mailhot, A.; Frigon, A. Simple Scaling of Extreme Precipitation in North America. Hydrology and Earth System Sciences 2017, 21 (11), 5823–5846.

IPCC – SREX https://archive.ipcc.ch/report/srex/ (accessed 2021-11).

IPCC Fifth Assessment Report. AR5 Climate Change 2013: The Physical Science Basis — IPCC, 2013.

IPCC., A. S. Climate Change 2007: Synthesis Report. Summary for Policymakers 2007.

Johnson, F., & Sharma, A. (2012). A nesting model for bias correction of variability at multiple time scales in general circulation model precipitation simulations. Water Resources Research, 48(1).

Kaykhosravi, S., Khan, U. T., & Jadidi, M. A. (2020). The effect of climate change and urbanization on the demand for low impact development for three Canadian cities. Water, 12(5), 1280.

Kendon, E. J., R. A. Stratton, S. Tucker, J. H. Marsham, S. Berthou, D. P. Rowell, and C. A. Senior. 2019. "Enhanced future changes in wet and dry extremes over Africa at convection-permitting scale." Nat. Commun. 10 (1): 1794.

Kuo, C.-C.; Gan, T. Y.; Gizaw, M. Potential Impact of Climate Change on Intensity Duration Frequency Curves of Central Alberta. Climatic Change 2015, 130 (2), 115–129.

Hempel, S., Frieler, K., Warszawski, L., Schewe, J., & Piontek, F. (2013). A trend-preserving bias correction–the ISI-MIP approach. Earth System Dynamics, 4(2), 219-236.

Langousis, A.; Veneziano, D. Intensity-duration-frequency Curves from Scaling Representations of Rainfall. Water Resources Re-search 2007, 43 (2).

Li, C.; Zwiers, F.; Zhang, X.; Chen, G.; Lu, J.; Li, G.; Norris, J.; Tan, Y.; Sun, Y.; Liu, M. Larger Increases in More Extreme Local Precipitation Events as Climate Warms. Geophysical Research Letters 2019, 46 (12), 6885–6891.

Li, H.; Sheffield, J.; Wood, E. F. Bias Correction of Monthly Precipitation and Temperature Fields from Intergovernmental Panel on Climate Change AR4 Models Using Equidistant Quantile Matching. Journal of Geophysical Research: Atmospheres 2010, 115 (D10).

Ligeti, E.; Wieditz, I.; Penney, J. A scan of climate change impacts on Toronto. Clean Air Partnership 2006.

Martel, J. L., Brissette, F. P., Lucas-Picher, P., Troin, M., & Arsenault, R. (2021). Climate Change and Rainfall Intensity–Duration–Frequency Curves: Overview of Science and Guidelines for Adaptation. Journal of Hydrologic Engineering, 26(10), 03121001.

Min, S.-K., X. Zhang, F. W. Zwiers, and G. C. Hegerl. 2011. "Human contribution to more-intense precipitation extremes." Nature 470 (7334): 378–381.

Mirhosseini, G.; Srivastava, P.; Fang, X. Developing Rainfall Intensi-ty-Duration-Frequency Curves for Alabama under Future Climate Scenarios Using Ar-tificial Neural Networks. Journal of Hydrologic Engineering 2014, 19 (11), 04014022.

Najafi, M. R., Moradkhani, H., & Piechota, T. C. (2012). Ensemble streamflow prediction: climate signal weighting methods vs. climate forecast system reanalysis. Journal of Hydrology, 442, 105-116.

Noor, M., Ismail, T., Chung, E. S., Shahid, S., & Sung, J. H. (2018). Uncertainty in rainfall intensity duration frequency curves of peninsular Malaysia under changing climate scenarios. Water, 10(12), 1750.

Norris, J.; Chen, G.; Neelin, J. D. Thermodynamic versus Dynamic Controls on Extreme Precipitation in a Warming Climate from the Community Earth System Model Large Ensemble. Journal of Climate 2019, 32 (4), 1025–1045.

Piani, C., Weedon, G. P., Best, M., Gomes, S. M., Viterbo, P., Hagemann, S., & Haerter, J. O. (2010). Statistical bias correction of global simulated daily precipitation and temperature for the application of hydrological models. Journal of hydrology, 395(3-4), 199-215.

Requena, A. I., Burn, D. H., & Coulibaly, P. (2021). Technical guidelines for future intensity–duration–frequency curve estimation in Canada. Canadian Water Resources Journal/Revue Canadienne des Resources Hydriques, 46(1-2), 87-104.

Rodríguez, R.; Navarro, X.; Casas, M. C.; Ribalaygua, J.; Russo, B.; Pouget, L.; Redaño, A. Influence of Climate Change on IDF Curves for the Metropolitan Area of Barcelona (Spain). International Journal of Climatology 2014, 34 (3), 643–654.

Sandink, D., Simonovic, S. P., Schardong, A., & Srivastav, R. (2016). A decision support system for updating and incorporating climate change impacts into rainfall intensity-duration-frequency curves: Review of the stakeholder involvement process. Environmental Modelling & Software, 84, 193-209.

Schardong, A.; Simonovic, S. P.; Gaur, A.; Sandink, D. Web-Based Tool for the Development of Intensity Duration Frequency Curves under Changing Climate at Gauged and Ungauged Locations. Water 2020, 12 (5).

Scoccimarro, E., Villarini, G., Vichi, M., Zampieri, M., Fogli, P. G., Bellucci, A., & Gualdi, S. (2015). Projected changes in intense precipitation over Europe at the daily and subdaily time scales. Journal of climate, 28(15), 6193-6203.

Seidou, O., & Alodah, A. (2018). From top-down to bottom-up approaches to risk discovery: a paradigm shift in climate change impacts and adaptation studies related to the water sector. In Proceedings of the Annual Conference of the Canadian Society for Civil Engineering (CSCE2018), Fredericton, NB, Canada (pp. 13-16).

Şen, O.; Kahya, E. Impacts of Climate Change on Intensity–Duration–Frequency Curves in the Rainiest City (Rize) of Turkey. Theoretical and Applied Climatology 2021, 144 (3), 1017–1030.

Senior, M., Scheckenberger, R., Nimmrichter, P., Ingebrigsten, M. (2019) Assessing Potential Climate Change Impacts to a Stormwater Management System for a Residential Subdivision in Southern Ontario, 2019 CSCE Annual Conference, Laval (Greater Montreal), Canada.

Shephard, M. W.; Mekis, E.; Morris, R. J.; Feng, Y.; Zhang, X.; Kilcup, K.; Fleetwood, R. Trends in Canadian Short-duration Ex-treme Rainfall: Including an Intensity–Duration–Frequency Perspective. Atmosphere-Ocean 2014, 52 (5), 398–417.

Shukor, M. S. A., Yusop, Z., Yusof, F., Sa'adi, Z., & Alias, N. E. (2020). Detecting rainfall trend and development of future intensity duration frequency (IDF) curve for the state of Kelantan. Water Resources Management, 34(10), 3165-3182.

Sillmann, J.; Kharin, V. V.; Zwiers, F.; Zhang, X.; Bronaugh, D. Climate Extremes Indices in the CMIP5 Multimodel Ensemble: Part 2. Future Climate Projections. Journal of Geophysical Research: Atmospheres 2013, 118 (6), 2473–2493.

Simonovic, S. P. (2017). Bringing future climatic change into water resources management practice today. Water Resources Management, 31(10), 2933-2950.

Singh, R., Arya, D. S., Taxak, A. K., & Vojinovic, Z. (2016). Potential impact of climate change on rainfall intensity-duration-frequency curves in Roorkee, India. Water Resources Management, 30(13), 4603-4616.

Srivastav, R. K.; Schardong, A.; Simonovic, S. P. Equidistance Quantile Matching Method for Updating IDF Curves under Climate Change. Water Resources Management 2014, 28 (9), 2539–2562.

Sunyer, M. A., Gregersen, I. B., Rosbjerg, D., Madsen, H., Luchner, J., & Arnbjerg-Nielsen, K. (2015). Comparison of different sta-tistical downscaling methods to estimate changes in hourly extreme precipitation using RCM projections from ENSEMBLES. International Journal of Climatology, 35(9), 2528-2539.

Switzman, H., Razavi, T., Traore, S., Coulibaly, P., Burn, D. H., Henderson, J., ... & Ness, R. (2017). Variability of future extreme rainfall statistics: comparison of multiple IDF projections. Journal of Hydrologic Engineering, 22(10), 04017046.

Szeląg, B., Kiczko, A., Łagód, G., & De Paola, F. (2021). Relationship Between Rainfall Duration and Sewer System Performance Measures Within the Context of Uncertainty. Water Resources Management, 35(15), 5073-5087.

Tabari, H. (2020). Climate change impact on flood and extreme precipitation increases with water availability. Scientific reports, 10(1), 1-10.

Tatli, H. (2021). Multivariate-drought indices—case studies with observations and outputs of NCAR CCSM-4 ensemble models. Theoretical and Applied Climatology, 146(1), 257-275.

Uraba, M. B.; Gunawardhana, L. N.; Al-Rawas, G. A.; Baawain, M. S. A Downscaling-Disaggregation Approach for Developing IDF Curves in Arid Regions. Environ-mental Monitoring and Assessment 2019, 191 (4), 245–245.

Vavrus, S.; Van Dorn, J. Projected Future Temperature and Precipitation Extremes in Chicago. Journal of Great Lakes Research 2010, 36, 22–32.

Veneziano, D.; Furcolo, P. Multifractality of Rainfall and Scaling of Intensity-duration-frequency Curves. Water resources research 2002, 38 (12), 42–1.

Wang, D.; Hagen, S. C.; Alizad, K. Climate Change Impact and Uncertainty Analysis of Extreme Rainfall Events in the Apalachic-ola River Basin, Florida. Journal of Hydrology 2013, 480, 125–135.

Wang, M., Zhang, D., Lou, S., Hou, Q., Liu, Y., Cheng, Y., ... & Tan, S. K. (2019). Assessing hydrological effects of bioretention cells for urban stormwater runoff in response to climatic changes. Water, 11(5), 997.

Wellstead, A., Howlett, M., Nair, S., & Rayner, J. (2016). "Push" dynamics in policy experimentation: Downscaling climate change adaptation programs in Canada. Climate Services, 4, 52-60.

Westra, S., Fowler, H. J., Evans, J. P., Alexander, L. V., Berg, P., Johnson, F., ... & Roberts, N. M. (2014). Future changes to the intensity and frequency of short-duration extreme rainfall. Reviews of Geophysics, 52(3), 522-555.

Westra, S.; Alexander, L. V.; Zwiers, F. W. Global Increasing Trends in Annual Maximum Daily Precipitation. Journal of Climate 2013, 26 (11), 3904–3918.

Yeo, MH., Nguyen, VTV., Kim, Y.S. *et al.* An Integrated Extreme Rainfall Modeling Tool (SDExtreme) for Climate Change Impacts and Adaptation. Water Resources Management (2022).

Zhang, X.; Zwiers, F. W.; Li, G.; Wan, H.; Cannon, A. J. Complexity in Estimating Past and Future Extreme Short-Duration Rainfall. Nature Geoscience 2017, 10 (4), 255–259.

Chapter 4. Assessing the Performance of Daily to Sub-Daily Temporal Disaggregation Methods for IDF Curves Generation under Climate Change

4.1 Abstract

Given the short time of concentration in urban watersheds, the design of municipal water infrastructures, such as storm sewers and detention basins, often requires knowledge of sub-daily precipitation intensity. Sub-daily time series can be directly used in a rainfall-runoff model or to derive Intensity-Duration-Frequency (IDF) curves and calculate the design precipitation or flow. Given that precipitation projections are typically at a daily time scale, temporal disaggregation using techniques of variable complexity is often needed to evaluate the risk/performance of urban infrastructure in the future. In this paper, a simple steady-state stochastic disaggregation model that generates wet/dry day occurrence using a binomial distribution and precipitation intensity using an exponential distribution is proposed and compared to widely used temporal disaggregation methods: the multiplicative random cascade model (MRC), the Hurst-Kolmogorov process (HKP), and three versions of the K-nearest neighbour model (KNN) using the nonparametric KS test. The six disaggregation techniques were assessed at four stations located in the South Nation River Watershed located in Eastern Ontario, Canada. Daily precipitation time series were obtained by downscaling the outputs of four regional climate models (RCMs) forced with the high-emission scenarios (RCP8.5) for the future period (2010-2100) using quantile mapping method. Results indicate that the method introduced in this work performed well compared to other temporal disaggregation methods when resampling the observed extreme precipitation.

Keywords

Climate change, GCM, RCM, HKP, IDF curves, KNN, MRC, temporal disaggregation

Highlights

1. A simple steady-state stochastic disaggregation model is introduced to generate future sub-daily precipitation data.
2. Climate change impacts on short-duration precipitation extreme events are investigated using different temporal disaggregation methods.
3. The developed disaggregation method adequately resamples the observed short-duration extreme precipitation for application in municipal water infrastructure.

4.2 Introduction

Changes in the temporal variability of precipitation at all timescales is expected as a result of global warming. Such changes affect urban water infrastructure by potentially influencing their performance and risk of failure. Unfortunately, there is considerable uncertainty about how hydrological variables will change in the future. While uncertainty is present at all timescales, the climate signal in the daily time series simulated by climate models, for instance, can be estimated with much greater certainty than in the simulated hourly time series. Sub-daily (finer-scale) time series are critical in some water resource engineering problems, especially urban hydrology because they serve as input for urban drainage system design. One way of obtaining hourly or sub-hourly precipitation time in the future is to temporally disaggregate daily time series generated using either weather generators or spatially downscaled climate models outputs. Daily time series can, for instance, be disaggregated into hourly time steps and converted to IDF curves or be directly fed to a rainfall-runoff model. Temporal disaggregation is the conversion of annual, monthly, or daily scale observations into sub-daily scales, such as hourly or minute scales, using a stochastic approach. Examples of temporal disaggregation techniques include: i) the K-nearest neighbour disaggregation model (KNN); ii) the multiplicative random cascade model (MRC); ii) the microcanonical random cascade model (MRCM) (e.g., Olsson 1998; Olsson and Berndtsson, 1998; Molnar and Burlando 2005; Licznar *et al.,* 2011; Jebari *et al.,* 2012; Müller and Haberlandt, 2015; Garbrecht, 2017; Gaur and Lacasse 2018); and iii) and iv) the Hurst-Kolmogorov process downscaling model (HKP) (Hurst, 1951) (Hurst, 1951; Müller and Haberlandt, 2015; Lombardo *et al.,* 2017; Koutsoyiannis and Cohn, 2008).

The KNN disaggregation technique is a version of the method of fragments (MF). The MF is a popular nonparametric temporal disaggregation approach in which sub-daily precipitation values are estimated as fractions (fragments) of the daily precipitation amount. In the KNN approach, the fragments are calculated using available daily and hourly precipitation time series that are close (neighbour) to the period of interest based on a distance measure (e.g., distance in time, magnitude, etc.). Park and Chung (2020) applied the KNN model using three-day patterns and found that the disaggregated hourly rainfall data had similar statistical properties to the observed series. Sharif *et al.,* (2013) applied the KNN model to synthesize and temporally disaggregate daily precipitation under climate change scenarios in the Upper Thames River Basin (UTRB). They found that the model effectively reproduces simulated sequences of future climate scenarios represented and predicted by GCMs. Lu *et al.,* (2015) investigated the effects of climate change on heavy regional rainfall by producing a spatially and temporally varying rainfall time series using a hybrid LARS-WG and KNN model. Uraba *et al.,* (2019) used a stochastic KNN disaggregation model to convert downscaled GCM scale rainfall production; They found that climate change's impact on rainfall intensity would be noticeable in storms with shorter durations and longer return times. Sharma *et al.,* (2006) applied KNN combined with the fragment (KNN-MOF) method. Their results showed that KNN-MOF performed better in producing the descriptive statistics of wet and dry spell distributions than the other models. The main challenge in the KNN model is choosing the optimum value of neighbours for the temporal downscaling process. The number of neighbours should be estimated to synthesize daily time series using the KNN model (Sharif and Burn, 2007).

HKP is a stochastic process disaggregation model that uses Gaussian white noise to convert precipitation from coarser to finer scales. This model uses the Hurst exponent (H) to qualify the data behaviour. Hurst (1951) observed randomness in numerous physical time series, and the tendency of natural events was the most significant even though these events were in higher and lower values. The HKP method was intensely used in hydrology and water resource management to generate sub-hourly or subdaily scales for different purposes in the urban water system. A challenge in the HKP model is determining the H value, which is expensive to estimate. Lombardo *et al.,* (2012) used HKP to convert the daily precipitation into a five-minute time step. However, the model is in the log domain, and not all daily time series are appropriate for a lognormal distribution.

The MRC model, first introduced by Olsson (1998), is an invariance scaling method used for temporal downscaling. Gaur and Lacasse (2018) applied the MRC model to multivariate climate variables at several sites within the same region to assess the model's accuracy in performance. Licznar *et al.,* (2011) generated a fine scale using the multiplicative cascade model and a microcanonical cascade, yielding intermittency on a five-minute scale. Molnar and Burlando (2005) found that the cascade model performed well in terms of rainfall distribution preservation at a 10-minute scale; the model could reproduce the growth of the intermittency period. Koutsoyiannis and Onof (2001) developed a stochastic disaggregation model that combines a precipitation simulation with an adjustment process to convert the coarse scale to a finer scale. This model's main advantage is preserving descriptive precipitation statistics; however, the main limitation is that the model does not reproduce instantaneous hourly series because of the variance in the generated weights in each cascade level. Müller and Haberlandt (2018) found that a five-minute resolution will lead to missing time steps with dry intervals if the branching of the cascade is constant, and it is generally considered a limitation for the cascade model.

Temporal disaggregation techniques have different levels of complexity and unequal performances, and the generated time series may not have the same statistical characteristics. HKP and MRC are mathematically challenging to calibrate, while the KNN methods are straightforward. A natural question is whether more complex temporal disaggregation techniques lead to better results in terms of IDF curves and descriptive statistics of the disaggregated time series. In this paper, a simple temporal disaggregation technique called the

Fahad-Ousmane method (FO) is introduced. Daily time series of future precipitation are generated by spatially downscaling the outputs of four RCMs using quantile mapping (QM) method. The FO model and five alternative downscaling methods (the MRC, the HKP, and three versions of the KNN) are used to generate hourly precipitation time series in both the historic (1976-2005) and future periods (short term 2010-2040, medium-term 2041-2070 and long-term 2071-2100). Beside the visual comparison of generated IDF curves, the two sample Kolmogorov Smirnov test is used to compare the distribution of the time series of annual precipitation of durations 1h to 24h.

4.3 Materials and methodologies

4.3.1 General methodology

The general methodology of the work, as illustrated in Figure 4.1, is described as follows:

a) Developing a simple temporal disaggregation technique called the FO method.

b) Generating time series of daily precipitation by downscaling the precipitation output of a climate model using QM.

c) Disaggregating these time series from daily to subdaily (hourly) timescales by the MRC, the HKP, three versions of the KNN (5, 15, 30) and the FO model.

d) Extracting the maximum annual precipitation intensity for durations of 1 h to 24 h from the disaggregated and observed time series.

e) Generating IDF curves from the maximum annual precipitation of the disaggregated and observed time series; and

f) The disaggregation performance was tested using visual comparisons, main statistics, and the two-sample Kolmogorov–Smirnov (KS) test. The disaggregated hourly times series from disaggregation models (KNN, FO, MRC and HKP) will be compared with each other.

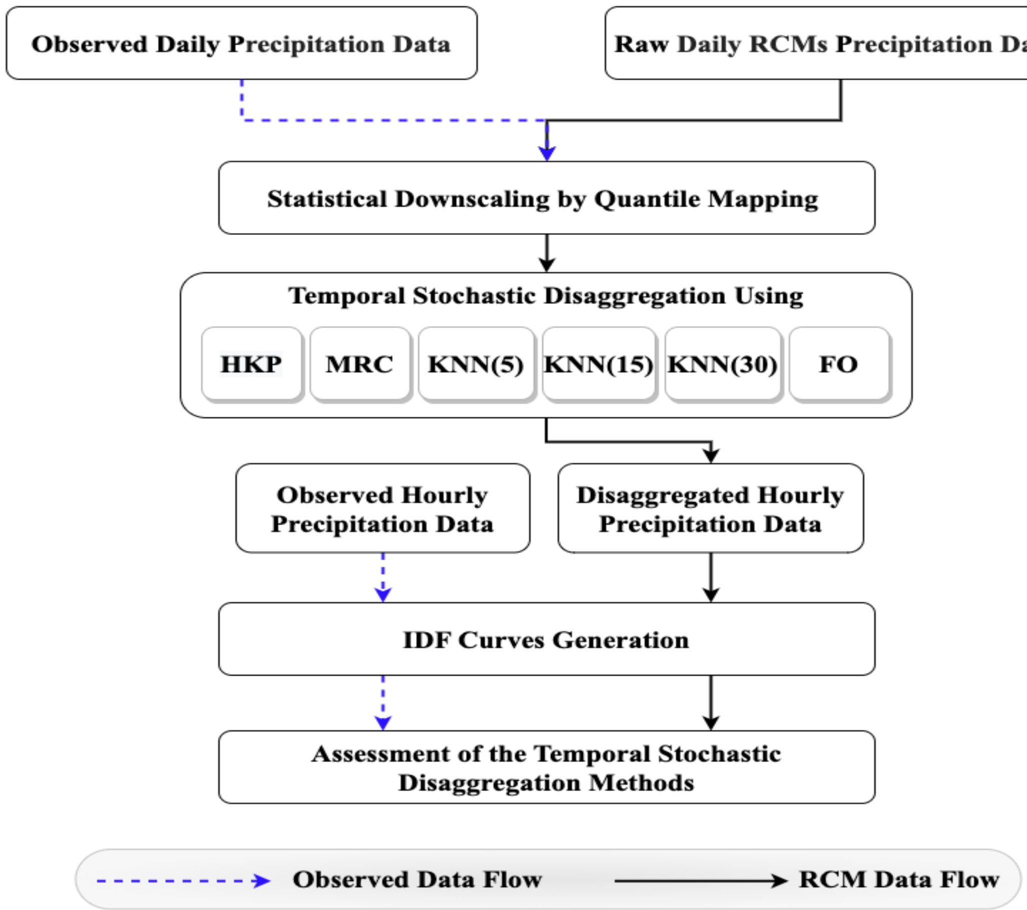

Figure 4.1 Flowchart of methodology.

4.3.2 Study area and available data

The study area is the South Nation watershed (approximately 4000 km^2), located southeast of Ottawa in Eastern Ontario, Canada (Figure 4.2). The South Nation River drains the watershed, running for 175 km with relatively flat topography (approximately 80 m between its headwaters and output at the Ottawa River), making the area prone to significant flooding risk. The observed daily precipitation (PCP) and hourly precipitation acquired from Environment Canada cover the 1976-2005 period at four stations, as presented in Table (4.1). Table (4.2) presents the available regional climate model outputs from the NA-CORDEX experiment.

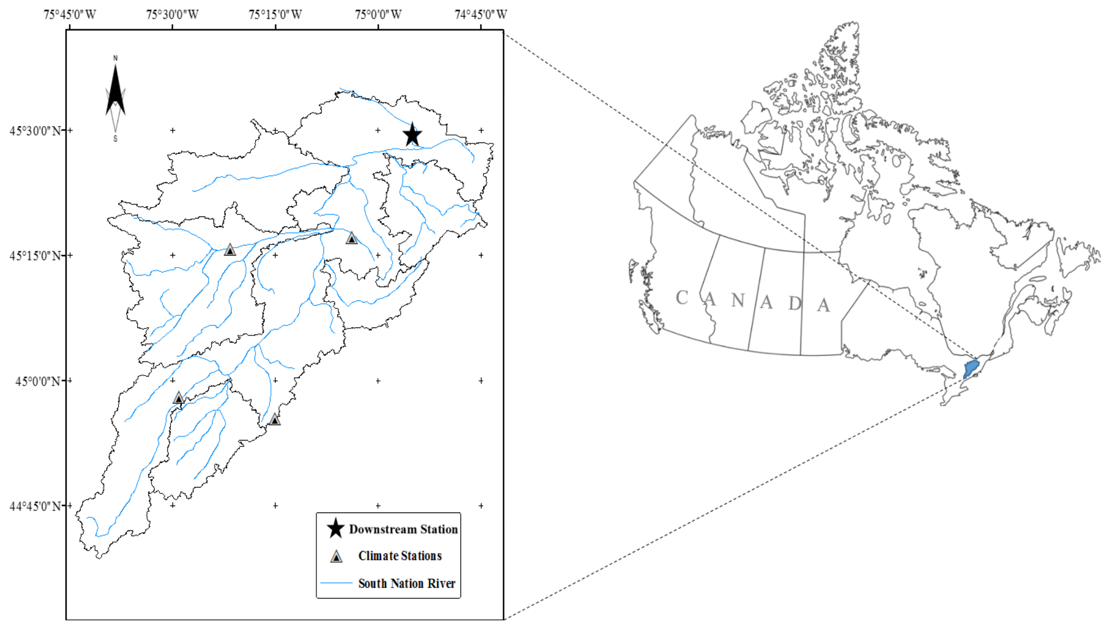

Figure 4.2 The meteorological gauges in the South Nation watershed (Alodah and Seidou, 2019).

Table 4.1 Weather station information.

Station	Climate Identifier	Latitude (N)	Longitude (W)	Elevation (m)	Mean	Standard Deviation
St. Albert	6107276	45° 17' 14"	75° 03' 49"	80	2.77	6.06
South Mountain	6107955	44° 58' 00"	75° 29' 00"	84.7	2.64	6.07
Morrisburg	6105460	44° 55' 25"	75° 11' 18"	81.7	2.77	6.17
Russell	6107247	45° 15' 46"	75° 21' 34"	76.2	2.63	5.97

Table 4.2 List of regional climate models used in the study.

Global Circulation Models (GCM), (Driver)	Regional Climate Model (RCM)	Representative Concentration Pathways (RCP) Scenario		Variable
Second-generation Canadian Earth System Model (CanESM2)	Canadian Regional Climate Model Version 4 (CanRCM4)	RCP 4.5 & RCP 8.5		Precipitation (pr)
European Earth System Model (EC-EARTH)	High-Resolution Limited Area Model Physics, Version 5 (HIRHAM5)	RCP 4.5	RCP 8.5	Precipitation (pr)
	Rossby Centre Regional Atmospheric Climate Model (RCA4)	RCP 4.5	RCP 8.5	
Geophysical Fluid Dynamic Laboratories (GFDL)	Regional Climate Model Version 4 (RegCM4)	RCP 8.5		Precipitation (pr)

4.3.3 Downscaling RCM outputs at the daily timescale

The outputs of the RCMs are downscaled using the QM technique. The QM method consists of remapping the probability density function (PDF) of the uncorrected RCM series in combination with the probability of the observed data series. The following formula transforms the corrected RCM to cumulative distribution functions:

$$X_{Corrected}=F^{-1}_{Observed}\,(F_{RCM}(X_{RCM})) \qquad \text{Eq (4.1)}$$

where $\boldsymbol{X_{RCM}}$ adds to the RCM data before projection. In practice, Equation (4.1) is replaced by the following mapping function between GCM outputs and observations:

$$\begin{bmatrix} \left(X_{observation}\right)_{sorted,1} & \left(X_{RCM}\right)_{sorted,1} \\ \left(X_{observation}\right)_{sorted,2} & \left(X_{RCM}\right)_{sorted,2} \\ . & \\ . & \\ . & \\ \left(X_{observation}\right)_{sorted,N} & \left(X_{RCM}\right)_{sorted,N} \end{bmatrix} \qquad \text{Eq (4.2)}$$

The limitation of this approach is that it cannot predict the values beyond the range of historical data. The reference period is split into validation and calibration. Equation (4.2) is fitted to the calibration period and applied to the validation and future periods. To avoid any bias that may result from oscillations in the observed precipitation time series, the calibration data set contains all data series from 1976-1991, and the validation period covers the data series for the time range of 1992-2005.

4.3.4 Temporal disaggregation techniques

The following subsections describe the models and theories of each temporal stochastic disaggregation method. Four temporal downscaling techniques are considered: the KNN disaggregation technique, the MRC model, the HKP downscaling model, and a novel disaggregation technique called the FO model.

4.3.4.1 *K-nearest neighbour disaggregation technique (KNN)*

The K-nearest neighbour disaggregation technique (KNN) is a particular case of the fragment (MF) method, a nonparametric approach commonly used by researchers for the above reason. The principle of the method is to generate fragments that are fractions of daily precipitation that occur in each hour of the day, and then, the fragments are summed to 1. The general formulation of the MF is given in Equations (4.3) and (4.4). Equation (4.3) contains w_i, which is the weight that will be computed, h_i is the data selected to produce fragments from the series, and n is the number of data in the series (24 hours).

$$w_i = \frac{h_i}{\sum_{i=1}^{n} h_i} \qquad \text{Eq (4.3)}$$

Then, each fragment is multiplied by daily data d in Equation (3) to obtain the new hourly data or disaggregated values.

$$h'_i = w_i \times d \qquad \text{Eq (4.4)}$$

The hourly series of data used to estimate fragments could be chosen randomly; however, this would lead to inadequate statistical properties (Srikanthan and McMahon, 1982). Therefore, the best choice is to compare the total disaggregated daily precipitation with the close total daily precipitation before the disaggregation process (Wey, 2006). The K-nearest neighbour is a particular case of the fragment method where the fragment is selected from historical hourly precipitation in a sample of neighbours with similar precipitation amounts. The neighbours are selected in a temporal window to preserve the seasonal characteristics of precipitation. Note that the sliding window is based on the Julian calendar and spans all years in the data. The K neighbours with the most negligible difference in precipitation amount are selected. Then, one neighbour is sampled from the set and used to calculate the fragment. The probability of sampling neighbour $\boldsymbol{j}$ is

$$p(j) = \frac{{}^{1}/_{|P(j)-P(t)|}}{\sum_{i=1}^{k}(|P(i)-P(t)|)} \qquad \text{Eq (4.5)}$$

where *p(j)* is the precipitation amount of neighbour *j* and *P(s)* is the precipitation amount on the simulation day.

4.3.4.2 Fahad- Ousmane disaggregation model

The FO model is a steady-state stochastic disaggregation model that generates wet hours (hours with precipitation above 1 mm) using a binomial distribution with parameter *p*, and for each wet hour, precipitation intensity is generated using an exponential distribution with parameter α. The parameters are fitted month by month using observed data in the calibration period as follows:

a) Estimate all hourly precipitation for month M.
b) Estimate *p* as the ratio of hours with precipitation higher than 1 mm to the total number of hours.
c) Create a time series of hours with precipitation above 1 mm.
d) Fit the exponential distribution to the above time series to obtain *α*.

The generation of hourly precipitation for a day with precipitation amount p_{day} is calculated as follows:

a) If *p=0,* set all hourly values to 0.
b) If *p>0*,
    a. Generate a series of 0 (dry hours) and 1 (wet hours); repeat until you obtain at least one nonzero value.
    b. For each wet hour h, take a sample from the exponential distribution with the parameter α to obtain $\mathrm{p_h}$(hour); otherwise, set $\mathrm{p_h}$(hour) to 0 for dry hours.

The final precipitation for each hour of the day is set to

$$\boldsymbol{p_{day}} = \frac{\boldsymbol{P_{hour}(h)}}{\sum_{i=0}^{24} \boldsymbol{P_{hour}(i)}} \qquad \text{Eq (4.6)}$$

4.3.4.3 Hurst-Kolmogorov downscaling model

The Hurst-Kolmogorov downscaling model is a technique used to convert coarse-scale data into fine-scale data. This model uses pure downscaling to generate precipitation based on fractional Gaussian noise called the HKP (Koutsoyiannis, 2002). As shown in Figure 4.2, a dyadic additive cascade is used to disaggregate fractional Gaussian noise; each higher amount of precipitation is disaggregated into a lower-scale level. Then, the disaggregated fractional

Gaussian noise is exponentially transformed to derive the actual precipitation. The HKP represents the long-term persistence of the observed time series with a simple and efficient stochastic process. Additionally, it has been demonstrated that this random representation is not solely based on data, as the behaviour of Hurst-Kolmogorov develops from entropy production (Koutsoyiannis *et al.*, 2011). For any integers *i* and j and any timescale ***f*** and ***i***, the HKP could be defined as a stochastic stationary process, as in the following equation:

$$\left(\tilde{R}_j^{(f)} - \tilde{\mu}\right) \stackrel{\text{def}}{=} \left(\frac{f}{l}\right)^{H-1} \left(\tilde{R}_j^{(l)} - \tilde{\mu}\right) \qquad \text{Eq (4.7)}$$

where $\stackrel{\text{def}}{=}$ indicates the equality in probability distributions, *H* is the Hurst coefficient in the range between 0 and 1, $\tilde{R}_j$ is Gaussian noise, and $\tilde{\mu} = \langle \tilde{R} \rangle$ is the mean value. For the related process, $\tilde{R}_j^{(f)}$ in the following equation is used:

$$var\left[\tilde{Z}_j^{(f)}\right] = f^2 var\left[\tilde{R}_j^{(f)}\right] = f^{2H}\tilde{\sigma}^2 \qquad \text{Eq (4.8)}$$

where $var[\tilde{R}] = \tilde{\sigma}^2$.

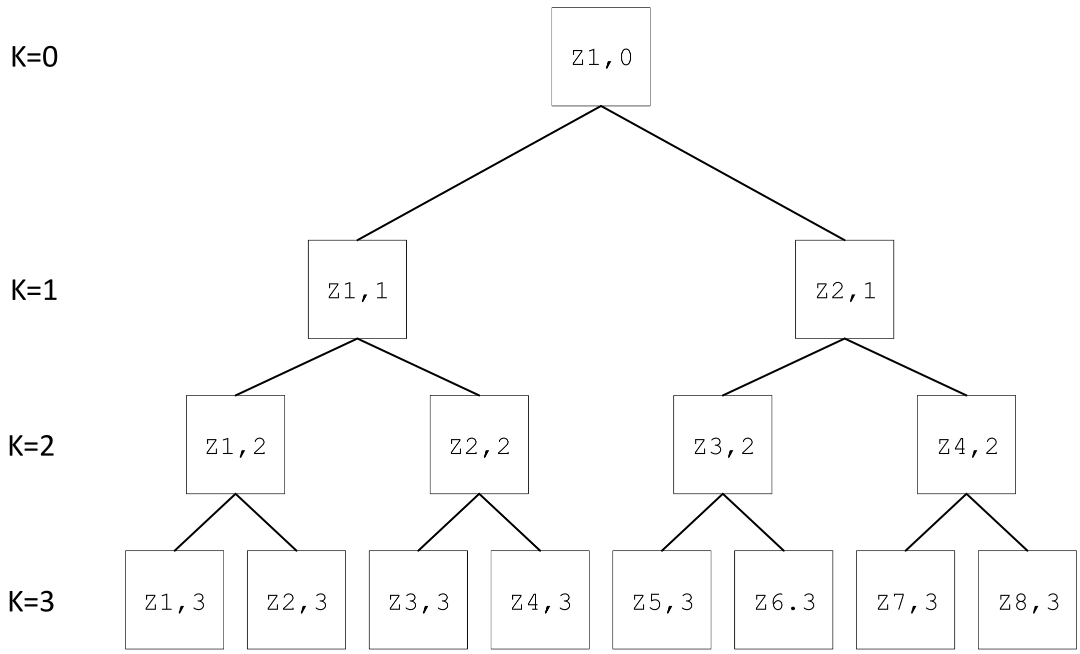

Figure 4.3 A sketch of the disaggregation model steps at the level of k)Lombardo *et al.,* 2012).

The HKP is implemented as follows: consider the Z_1^f to be the depth of daily precipitation aggregated in an enormous timescale (j=1). Z_1^f is assumed to be a random variable with a mean and standard deviation of the stochastic process. The observed daily precipitation is assumed to be a lognormal distribution. An auxiliary Gaussian random variable $Z_1^f :=$ $ln\ (Z_1^f)$ of the aggregated HKP on a timescale f with mean $\tilde{\mu}_0$ and variance $\tilde{\sigma}_0^2$ is expressed as follows:

$$\tilde{\mu}_0 = ln\, \mu_0\ - \frac{1}{2}\left(\frac{\sigma_0^2}{\mu_0^2} + 1\right) \qquad \text{Eq (4.9)}$$

$$\tilde{\sigma}_0^2 = ln\left(\frac{\sigma_0^2}{\mu_0^2} + 1\right) \qquad \text{Eq (4.10)}$$

$\tilde{Z}_{1,0}$ is disaggregated as a dyadic ($b = 2$) additive cascade. Then, $\tilde{Z}_{1,0}$ is split into two ($b = 2$) Gaussian random variables based on the timescale $\Delta s = f/2$. For example, at the first cascade level $k = 1$, we have$\tilde{Z}_{1,1} + \tilde{Z}_{2,1} = \tilde{Z}_{1,0}$. Similarly, the k cascade level corresponds to $\Delta s_k = 2^{-kf}$

$$\tilde{Z}_{1,0} + \tilde{Z}_{2j,k} = \tilde{Z}_{j,k-1} \qquad \text{Eq (4.11)}$$

Consequently, the equation is adequate to generate $\tilde{Z}_{j,k-1}$ and then obtain $\tilde{Z}_{2j,k}$.

This is a generic procedure that resembles the well-known interpolation procedure. Therefore, the following linear generation scheme is considered, as shown in Figure 4.2:

$$\tilde{Z}_{2j-1,k} = \theta^T Y + V \qquad \text{Eq (4.12)}$$

where $V = [\tilde{Z}_{2j-3,k}, \tilde{Z}_{2j-2,k}, \tilde{Z}_{j,k-1}, \tilde{Z}_{j+1,k-1}]^T$ Θ is a vector of parameters, and V is Gaussian white noise. This equation allows the interpolated value to preserve the total depth of two earlier lower-level variables (level k) and one later higher-level variable (level k –1) (Koutsoyiannis 2002).

Therefore, in each disaggregation step, two lower-level variables are estimated by

$$\tilde{Z}_{2j-1,k} = a_2\tilde{Z}_{2j-3,k} + a_1\tilde{Z}_{2j-2,k} + b_0\tilde{Z}_{j,k-1} + b_1\tilde{Z}_{j+1,k-1} + V \qquad \text{Eq (4.13)}$$

$$\tilde{Z}_{j,k-1} = \tilde{Z}_{j,k-1} - \tilde{Z}_{2j-1} \qquad \text{Eq (4.14)}$$

where the parameters a_2, a_1, b_0, and b_1 and the variance V are estimated in terms of the correlation coefficient ρ, which is independent of j and k, and of the HKP variance at level k (Koutsoyiannis 2002), as given by the following equations:

$$\begin{bmatrix} a_2 \\ a_1 \\ b_0 \\ b_1 \end{bmatrix} =$$

$$\begin{bmatrix} 1 & \tilde{\rho}(1) & \tilde{\rho}(2) + \tilde{\rho}(3) & \tilde{\rho}(4) + \tilde{\rho}(5) \\ \tilde{\rho}(1) & 1 & \tilde{\rho}(1) + \tilde{\rho}(2) & \tilde{\rho}(3) + \tilde{\rho}(4) \\ \tilde{\rho}(2) + \tilde{\rho}(3) & \tilde{\rho}(1) + \tilde{\rho}(2) & 2[1 + \tilde{\rho}(1)] & \tilde{\rho}(1) + 2\tilde{\rho}(2) + \tilde{\rho}(3) \\ \tilde{\rho}(4) + \tilde{\rho}(5) & \tilde{\rho}(3) + \tilde{\rho}(4) & \tilde{\rho}(1) + 2\tilde{\rho}(2) + \tilde{\rho}(3) & 2[1 + \tilde{\rho}(1)] \end{bmatrix}^{-1} \begin{bmatrix} \tilde{\rho}(2) \\ \tilde{\rho}(1) \\ 1 + \tilde{\rho}(1) \\ \tilde{\rho}(2) + \tilde{\rho}(3) \end{bmatrix}$$

(15)

and

$$VAR[V] = \tilde{\sigma}_k^2(1 - [\tilde{\rho}(2), \tilde{\rho}(1), 1 + \tilde{\rho}(1), \tilde{\rho}(2) + \tilde{\rho}(3)][a_2, a_1, b_0, b_1]^T \qquad \text{Eq (4.16)}$$

The mean and the variance in the HKP at the k-level of the cascade are

$$\tilde{\mu}_k = \langle \tilde{Z}_{j,k} \rangle = \frac{\Delta s_k}{f} \tilde{\mu}_0 = \frac{\tilde{\mu}_0}{2^k} \qquad \text{Eq (4.17)}$$

$$\tilde{\sigma}_k^2 = var[\tilde{Z}_{j,k}] = \left(\frac{\Delta s_k}{f}\right)^{2H} \tilde{\sigma}_0^2 = \frac{\tilde{\sigma}_k^2}{2^{2Hk}} \qquad \text{Eq (4.18)}$$

where $\Delta s_k = 2^{-k} f$ and H is HKP.

The above step-by-step disaggregation approach was introduced by Koutsoyiannis (2002), who established that it effectively generates fractional Gaussian noise. However, the precipitation process is not a Gaussian distribution. Indeed, specific exponentiation to the HKP is applied by the following equation to make a lognormal domain and preserve the scaling properties:

$$Z_{j,k} = exp\ (\alpha(k)\tilde{Z}_{j,k} + \beta(k)) \qquad \text{Eq (4.19)}$$

HKP is assumed to be a unique process in the untransformed domain, and the characteristics of the exponentiation transformation are changed for the transformed domain. Using different characteristics for different disaggregation steps while utilizing the scale-dependence of the daily step will help to transform the Gaussian domain to a lognormal domain by the following equations:

$$\alpha(k) = \frac{2^{Hk}}{\tilde{\sigma}_0}\sqrt{ln\ (2^{2k(1-H)}(exp\ exp\ (\ \tilde{\sigma}_0^2 - 1)\ + 1)} \qquad \text{Eq (4.20)}$$

$$\beta(k) = -k\ ln\ ln\ 2 - \ \tilde{\mu}_0\left(\frac{\alpha(k)}{2^k} - 1\right) - \frac{\tilde{\sigma}_0^2}{2}\left(\frac{\alpha^2(k)}{2^{2Hk}} - 1\right) \qquad \text{Eq (4.21)}$$

The explained model is a disaggregation model only if the random variables are Gaussian processes. However, the hypothesis of lognormal rainfall, a conversion model of a coarser scale into a small scale, is statistically consistent with the given process *Z* at the coarser scale. The Hurst coefficient *H* is the only parameter of the HKP downscaling model. Therefore, the *H* value is estimated numerically.

H values have been estimated for each season from the historical time series because the disaggregated values are subject to the range of *H* values between 0 and 1. If the *H* value is closer to or beyond 1, the final values will be imagined, negative, or extreme. As a result, the simulated annual maximum precipitation would be the effect. Therefore, the results are needed for the calibration procedure. The procedure comprises thresholds and correction factors, which are estimated numerically using evolutionary optimization, such as a genetic algorithm, to estimate the optimal annual maximum precipitation values. The following equations illustrate the coefficients and thresholds, and these coefficients play the primary role in the results:

$$yy = pr_1 + pr_2 + pr_3 + pr_4 + x_4 \times R_{sim} \qquad \text{Eq (4.22)}$$

where

$$p_1 = 0.73 + \left(\frac{R_{sim}}{thr_1}\right) \qquad \text{Eq (4.23)}$$

$$p_2 = \ 0.12 + \left(\frac{R_{sim}}{thr_2}\right) \qquad \text{Eq (4.24)}$$

where

$aa_1 = x_2 \times \left(\frac{R_{sim}^2}{thr_2}\right)$ and $aa_2 = \frac{x_1 \times p_1 \times thr_1}{p_2}$ Eq (4.25)

$pr_1 = x_{12} \times sin\ (2\pi \times x_{11})$ Eq (4.26)

$pr_2 = x_1 \times thr_1 \times x_8^{1.99}$ Eq (4.27)

$pr_4 = x_3 \times \frac{R_{sim}}{thr_2} \times R_{sim} \times x_{10}^{1.99}$ Eq (4.28)

$pr_3 = aa_1 \times aa_2 \times x_9^{1.99}$ Eq (4.29)

Because the discrete data (precipitation to be simulated) are manipulated as samples of an analogue signal with its local maxima and minima of the annual maximum precipitation values, in some time intervals (some seasons), the coefficient performs as a periodic (distorted) signal with some periodicity.

The first poly (pr_1) contains a sinusoidal component, and the factors play a role in the amplitude and phase (x_{12} manages the amplitude and x_{11} controls the frequency of the sinusoidal component). The second poly (pr_2) has a *DC* value (direct current or constant value) where the simulated date is raised or lowered based on the factor value (x_1, x_8, and threshold [*thr1*]). Additionally, the third poly (pr_3) is added to cover the linear component (x_4). The fourth poly (pr_4) is added to consider a square component where the observed data are squared and multiplied linearly by the factor (x_3 and x_{10}). In the last poly, a cubic component of the actual data is applied to cover more possibilities of correlation with the actual data (x_2, thr_2, x_1, *and* x_9).

4.3.4.4 The multiplicative random cascade model

MRC model is a temporal scaling method that converts a coarse scale into a fine scale. The conversion is based on branch splitting of each value at a daily or subdaily scale. The best branch splitting occurs when the original value is split into two cells, called a dyadic cascade. The final format of the disaggregated hourly series comprises consecutive tree vertices of each rainy-day event.

In this section, *Pr* or *R* is the precipitation average over the timescale at the time origin (j=1). *Pr* is assumed to be a random variable with mean u_0 and variance sigma$_2$ of a stochastic process.

The branching number, which estimates the number of branches assigned to the next level with the smaller timescale steps for the distributed rainfall from the coarser-scale time step, is a structural component of the model. Using $b=2$ means that the 24 hours of the day could be split into day and night hours. Similarly, the day hours could be split into morning and afternoon hours. The precipitation amount V is multiplied by multiplicative weights W_1 and W_2 to obtain V at each time step. The total summation of these weights must equal 1 at each level, and they are not independent of one another; therefore, there is a probability of how the total amount of precipitation in each cascade level is converted. The following equation illustrates the three cases of each cascade level of branching (b=2):

$$W_1, W_2 = \begin{cases} 0 \; and \; 1 \; with \; P(0/1) \\ 1 \; and \; 0 \; \; with \; P(1/0) \\ x \; and \; 1-x \; \; with \; P(x/(1-x)); \; 0 < x < 1 \end{cases} \qquad \text{Eq (4.30)}$$

P denotes the probability for each time step in the level. The first case, which is *P* (1/0), means that the total precipitation is assigned in the first-time step (*W1=1*), and no precipitation will be allocated to the second time step when (*W2=1-W1=0*). For the second case, the probability of the *P* (0/1) disaggregation level is accomplished. The third case, which is the probability *(x/(1-x)* splitting, is to redistribute the rainfall amount over the time step, where *x* is defined as *0< x<1*, and it represents the relative fraction of precipitation values that is attributed to the first step. The *x* value is a random variable in all disaggregation steps, and the PDF *f(x)* can be estimated for each value of *x*. These cases in equation (4.30) provide the following four different types of wet boxes with $Pi > 0$: the first box is the starting box, including a dry box in the past time step and a wet box in the later time step. Second, the ending box follows a wet box and is followed by the dry box; this can be called a chain box. Next, the isolated box is defined as side-by-side past boxes, and the next steps are dry. Finally, the enclosed box is an isolated box case, but it is for wet boxes.

A reverse scaling procedure achieved these probability cases for three different cases in equation (4.29). Backward cascade level branching assumptions lead to highly resolved precipitation time series aggregation. Each cascade level of branches is summed to represent the total volume of precipitation at the preceding higher level. The statistics (mean, maximum, minimum, and standard deviation) and probabilities are calculated for each branch in the level by dividing the counts of each case by the total number of elements of the higher cascading level time series. Additionally, statistical calculations are needed to evaluate the case *P(x/1-x),* where x is the relative weight. Therefore, the relative weight (x) is a value between zero and the 90th percentile, influenced by the mean and standard deviation. This process aggregates the rainfall as follows: $1 \rightarrow 3\ h\ (3*2^0\ h)$, $3 \rightarrow 6\ h\ (3*2^1\ h)$, $6 \rightarrow 12\ h\ (3*2^2\ h)$, and $12 \rightarrow 24\ h\ (3*2^3\ h)$. In each aggregation step, a related weight is assigned to probabilities *P (0/1), P (1/0),* and *P (x/(1 − x))* before estimating the averages of all probabilities of all steps (Güntner *et al.* 2001). As a result, the probability and weight matrices are derived to represent the station's scaling. Notably, an empirical distribution is applied to estimate the parameters, which is done by a random number generator if there is no representation.

Sequentially, the weight matrices are applied to disaggregate the daily time series of precipitation. Tracing the random numbers for each cascade level, which incorporates the probabilities *(P (0/1)*, *P (1/0)*, and *P (x/(1 − x)))* (they are cumulatively evaluated), defines the branching type in each time step.

When the disaggregation of the daily precipitation model begins, the drawing of the random numbers determines the type of branching that incorporates the probabilities (three cases in the above equations). If the random numbers are in the range *P(x/(1 − x))*, a similar technique is applied to estimate the weight x value by using another random number.

Numerical simulation of the cascade is carried out if $\mu_o = 1$ and $\alpha^2_o = 0$. Thus, the summary statistics are

$$R_j^{(\Delta S_k)} = R_{j,k} = R_{1,0} \prod_{i=0}^{k} W_{g(i,j),i} \quad \text{Eq (4.31)}$$

where $j = 1, 2, \ldots, b^k$ is the position index in the series at level k; i is the index of the cascade level; and $g(i, j)$ represents a function defining the position in the series at level i, i.e., $g(i,j) = \left\lceil \frac{j}{b^{k-i}} \right\rceil$, which is a ceiling function (Gaume *et al.* 2007). For $k = 0$, we have $W_{1,0} = 1$.

$$\langle \frac{1}{b^k} \sum_{j=1}^{b^k} R_{j,k} \rangle = \langle R_0 \rangle \quad \text{Eq (4.32)}$$

where < > denotes the expected value, which is an average over the independent realizations of the stochastic process. The expected value of $R_{j,k}$ is given by

$$\langle R_{j,k} \rangle = \langle R_k \rangle = \langle R_{1,0} \prod_{i=0}^{k} W_{g(i,j),i} \rangle = \langle R_0 \rangle \langle \prod_{i=0}^{k} W_{g(i,j),i} \rangle = \langle R_0 \rangle \langle W \rangle^k = \mu_0 \mu_W^k \quad \text{Eq (4.33)}$$

For a microcanonical cascade model, the k-level's mean process equals the process at the 0-level, which means that a further cascade-level relationship will hold for every pair of successive aggregations.

$$\frac{1}{b} \sum_{i=b(j-1)+1}^{b-j} R_{j,k} = R_{j,k-1} \quad \text{Eq (4.34)}$$

where *j=1,... bk-1* with $k > 0$. The following example explains how the microcascade model processes during each cascade level when $b=2$:

$$\frac{1}{2} \sum_{i=2j-1}^{2j} R_{j,k} = R_{j,k-1}, R_{2j-1,k} + R_{2j,k} = 2R_{j,k-1}, W_{2j-1,k} = 2 - W_{2j,k} \quad \text{Eq (4.35)}$$

Therefore, in the above equation, the weights $W_{j,k}$ fulfil $\mu_W = 1$ and $W < b$.

Let us assume that the branching value is $b = 2$, and the exponent $h_{j,k}(t)$ represents the top of the tree, excluding the cascading level start that belongs to both simple paths leading to $R_{j\,k}$ and $R_{j+t,k}$. The $h_{j,k}(t)$ *is* calculated as follows:

$$h_{j,k}(t) = \begin{cases} \sum_{r=1}^{k} \Theta\,[2^{r-1} - j - t], j \leq 2^k, t > 0 \\ h_{2^k - j - t + 1, k}\,(t),\ j > 2^k, t > 0 \\ h_{2^k - j + 1, k}(|t|), \quad t < 0 \end{cases} \qquad \text{Eq (4.36)}$$

The following equation (4.37) illustrates the computation of the model's exponent $h_{j,k}(t)$. In the computation, we use this equation: $\langle R_{j,k} R_{j+t,k} \rangle = \langle R_0^2 \rangle \langle W^2 \rangle^{h_{j,k}(t)}$. The arrows show the links to those variables considered, where Θ[n] is the discrete form of the Heaviside step function, defined for a discrete variable (integer) n as

$$\Theta[n] = \begin{cases} 0, & n < 0 \\ 1, & n \geq 0 \end{cases} \quad \langle R_{j,k} R_{j+1,k} \rangle = \langle R_{1,0}^2 \rangle \langle W^2 \rangle^{h_{j,k}(t)} \qquad \text{Eq (4.37)}$$

$$\langle R_{4,3} R_{5,3} \rangle = \langle W_{4,3} W_{2,2} W_{1,1} W_{5,3} W_{3,2} W_{2,1} R_{1,0}^2 \rangle = \langle R_{1,0}^2 \rangle \qquad \text{Eq (4.38)}$$

$$h_{4,3}(t = -1) = 2$$

$$\langle R_{4,3} R_{5,3} \rangle = \langle W_{4,3} W_{2,2}^2 W_{1,1}^2 W_{3,3} R_{1,0}^2 \rangle = \langle R_{1,0}^2 \rangle \langle W^2 \rangle^2 \qquad \text{Eq (4.39)}$$

$$R_{3,3} = W_{3,3} W_{2,2} W_{1,1} R_{1,0}$$

$$R_{4,3} = W_{4,3} W_{2,2} W_{1,1} R_{1,0}$$

$$R_{5,3} = W_{5,3} W_{3,2} W_{2,1} R_{1,0}$$

The mathematical part can be calculated numerically in the following section. The numerical experiment of the MRC model is explained as follows:

$$\rho_{j,k}(t) = \frac{(1+\sigma_W^2)^{h_{j,k}(t)} - 1}{(1+\sigma_W^2)^k - 1} \qquad \text{Eq (4.40)}$$

The weights $\boldsymbol{W}$ refer to the lognormal distribution defined as follows:

$$W = b^{\sigma_N Y - \frac{\sigma_N^2 \ln b}{2}} \qquad \text{Eq (4.41)}$$

where Y is a normal random variable $N(1,0)$. Therefore, the variance in the weights is given by

$$\sigma_W^2 = \exp(\sigma_N^2 (\ln b)^2) - 1 \qquad \text{Eq (4.42)}$$

where σ_N^2 is a parameter defining the standard random variable of normal distribution.

To summarize, as the simulated subdaily scale is essential for the storm control design system, this section elaborates on the mathematical scheme of the open-source software in which the MRC model was implemented. The model makes valuable contributions to water resource engineering.

4.3.5 Estimation of intensity-duration-frequency (IDF) curves

The extreme theoretical value (EV) distribution approach is used to estimate the frequency of extreme precipitation for different durations and return period events. As long as the annual maximum precipitation is obtained for each duration, the Gumbel type I distribution (Gumbel, 1935) or EV could be the best approach. The Gumbel type I distribution is

$$G(x; \mu, \beta) = \frac{1}{\beta} e^{\frac{x-\mu}{\beta}} e^{-e^{\frac{x-\mu}{\beta}}} \qquad \text{Eq (4.40)}$$

where μ is the location and β is the scale parameter. The random variable X_T associated with the return period can be estimated as follows:

$$X_T = \overline{X} + K_T S \qquad \text{Eq (4.41)}$$

where $\overline{X}$ is the mean of the observed or simulated annual maximum precipitation values, and S is the standard deviation. K_T is the frequency factor calculated with a given return period (T):

$$K_T = -\frac{\sqrt{6}}{\pi}\left[0.5772 + \ln\left(ln\left(\frac{T}{T-1}\right)\right)\right] \qquad \text{Eq (4.42)}$$

The duration events 1-24 h are involved, and the return period T is 2 years; 5, 10, 50, 100, and 200 years are chosen to construct the curves.

4.4 Model performance measure

4.4.1 The two-sample Kolmogorov-Smirnov test

The KS test is used to compare two empirical cumulative distributions representing a simulated data set and an observed data set to identify whether they are significantly different; this is based on the following $D_{m,n}$ statistics (Massey, 1951):

$$D_{m,n} = |F_n^1(x) - F_n^2(x)| \qquad \text{Eq(4.43)}$$

where F_1 and F_2 are the *CDF* of the observed and simulated data, respectively.

The null hypothesis, H_0, is that the two samples are similar. The alternative hypothesis, H_1, is that the two samples are different. A critical value is calculated from the Kolmogorov distribution and compared with the $D_{m,n}$ statistic value. Therefore, $D_{m,n,\alpha}$ is the critical value, as estimated by the following formula:

$$D_{m,n,\alpha} = c(\alpha)\sqrt{\frac{m+n}{mn}} \quad \text{Eq (4.44)}$$

where $c(\alpha)$ is … the critical value obtained from the KS distribution table, and m & n are sample numbers. If $D_{m,n,\alpha}$ is more significant than $D_{m,n}$, then H_0 is accepted and both samples are similar. If $D_{m,n}$ is significantly larger than $D_{m,n,\alpha}$ then the null hypothesis is rejected.

4.5 Results

The uncorrected outputs of the four RCMs were downscaled using QM at the four climate stations on four arbitrarily chosen periods: a historical period (1979-2005), a short term period (2011-2040), medium term period (2041-2070), and long-term period (2071-2100). Each of the 64 daily time series was temporally disaggregated using five techniques (HKP, RCM, FO and KNN using 5, 15 and 30 neighbours). When using HKP and MRC, the daily time series were temporally disaggregated on five levels to obtain a time step of 1/36 h. These time series were linearly interpolated to produce hourly time series. Each hourly time series was afterward aggregated to obtain precipitation intensity time series at a 2h, 3h, …., and 24h time step, which in turn were converted into 24 time series of annual maximums and an IDF curve. The performance of each disaggregation time series was assessed by a) comparing the time series of annual maxima to corresponding observations using box plots and the KS-test and b) comparing the IDF curves derived from temporally disaggregated data with the IDF curves generated by observations on the historical period. The results of these comparisons are presented in the following sections:

4.5.1 Comparison of the simulated and observed time series of each temporal downscaling method

Figure 4.4 compares the observed and the disaggregated annual maxima resulted from FO, KNN (5), KNN(15), KNN (30), HKP and MRC models in historical period for the 1h and 24 hours time series. None of the models perfectly captures the interquartile range of the observed data as it was generally underestimated by MRC but overestimated by KNN models, HKP and FO at the one hour time step. For 24h time series, the interquartile range was overestimated by almost all models while HKP clearly did not mimic the observed values regardless of the RCM used. Results also show that HKP and MRC lead to more severe biases: HKP overestimates precipitation intensity at the one hour time step, while MRC underestimates them at the 24h time step. FO performed well compared to other models in terms of bias and interquartile range. The main descriptive statistics for each model; namely the mean, standard deviation, kurtosis and skewness, are presented in Table 4.3. All methods have mean and standard deviation values of the historical period close to the observations, while there are deviations in the kurtosis and skewness coefficients. The skewness of the observation and the FO and KNN models (all neighbour sizes) were found to be relatively similar to those of the observed values. MRC and HKP, in contrast, underestimated the skewness and the kurtosis values.

Table 4.4 provides the results of the similarity percentage between observed and downscaled AMP in the calibration and validation periods. The similarity percentage is estimated based on each climate station's KS test results of each temporal downscaling. The null hypothesis was systematically rejected for the MRC, except for the 1h duration event accepted by the test (Russel station, duration=1h) with a very small p-value, i.e., close to rejection. HKP had acceptance rates between 20% and 70%, while KNN and FO had better acceptance rates. KNN(30) and FO had acceptance rates of 100% except for one station, making them the best disaggregation techniques in this study.

Table 4.3 Descriptive statistics of observed and disaggregated hourly time series of Russell station.

Disaggregation method	GCM, RCM	Mean	Standard deviation	Skewness	Kurtosis
--	Observed	**0.1**	**0.6**	**20.7**	**760**
HKP	CanESM2, CanRCM4	0.1	0.5	7.1	82.4
	EC-EARTH, HIRHAM5	0.1	0.4	8.6	139.8
	EC-EARTH, RCA4	0.1	0.4	7.8	108.1
	GFDL, RegCM4	0.1	0.6	21.9	679.5
MRC	CanESM2, CanRCM4	0.1	0.4	9.9	150.4
	EC-EARTH, HIRHAM5	0.1	0.5	11.9	283.7
	EC-EARTH, RCA4	0.1	0.5	9.9	152.5
	GFDL, RegCM4	0.1	0.5	11.8	244.5
KNN(5)	CanESM2, CanRCM4	0.1	0.6	18.4	5613
	EC-EARTH, HIRHAM5	0.1	0.4	18.2	526.4
	EC-EARTH, RCA4	0.1	0.6	18.9	516.7
	GFDL, RegCM4	0.1	0.6	22.8	782.5
KNN(15)	CanESM2, CanRCM4	0.1	0.6	21.7	885.2
	EC-EARTH, HIRHAM5	0.1	0.4	18.4	539.7
	EC-EARTH, RCA4	0.1	0.6	18.2	475.6
	GFDL, RegCM4	0.1	0.7	24.8	910.4
KNN(30)	CanESM2, CanRCM4	0.1	0.6	19.5	636.5
	EC-EARTH, HIRHAM5	0.1	0.4	18.3	535.2
	EC-EARTH, RCA4	0.1	0.6	18.8	507.3
	GFDL, RegCM4	0.1	0.8	24.9	756.5
FO	CanESM2, CanRCM4	0.1	0.6	15.6	394
	EC-EARTH, HIRHAM5	0.1	0.4	11.9	196.1
	EC-EARTH, RCA4	0.1	0.6	14.3	264.9
	GFDL, RegCM4	0.1	0.7	27.6	1112.5

Table 4.4 Percentage of similarity between observed and downscaled AMP in the calibration (Cal.) and validation (Val.) periods across all climate change models.

Station	**Russell**		**Morrisburg**		**St. Albert**		**South Mountain**	
Model	***Cal.***	***Val.***	***Cal.***	***Val.***	***Cal.***	***Val.***	***Cal.***	***Val.***
HKP	63%	50%	65%	70%	63%	60%	20%	60%
MRC	0%	0%	0%	60%	0%	10%	10%	60%
KNN 5	63%	88%	94%	100%	60%	55%	80%	100%
KNN 15	65%	100%	100%	100%	65%	100%	100%	100%
KNN 30	75%	100%	100%	100%	75%	100%	100%	100%
FO	100%	100%	94%	100%	100%	100%	100%	100%

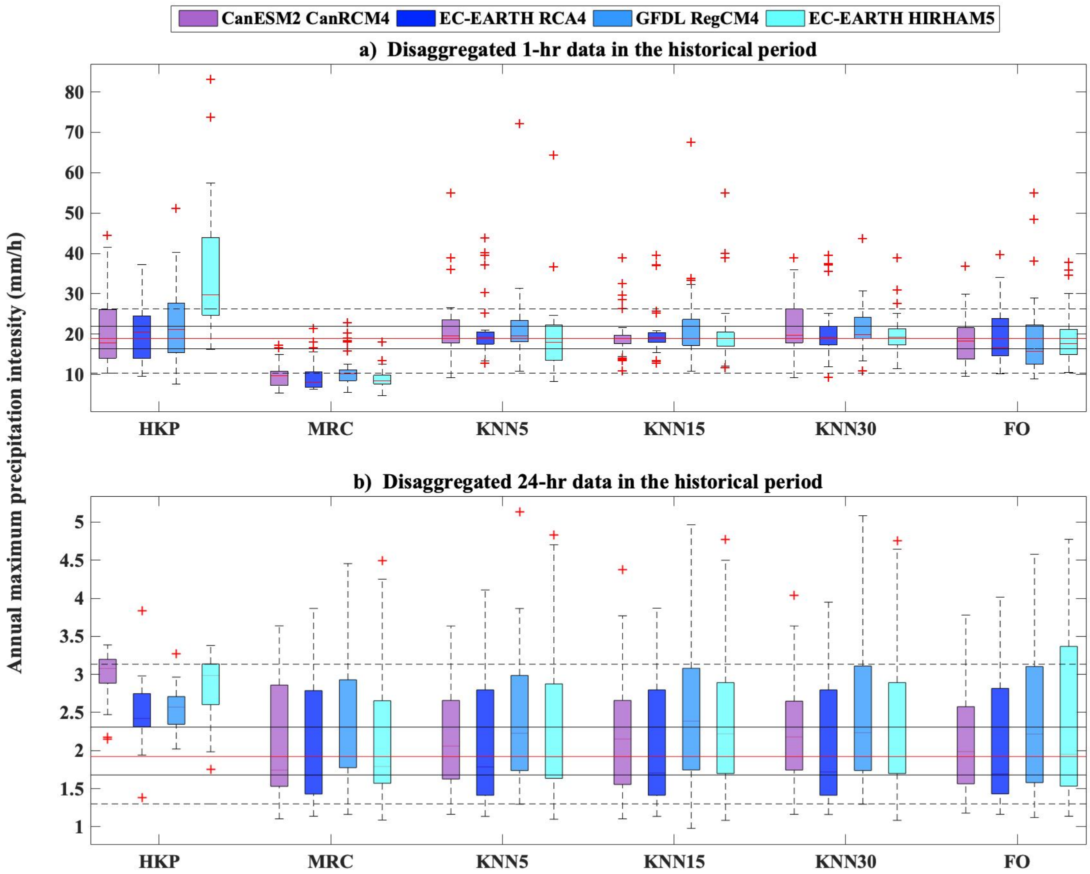

Figure 4.4 Grouped boxplot for all disaggregation methods and different RCMs in the historical period using a) 1-hr precipitation data, and b) 24-hr precipitation data. The horizontal solid black lines represent the 25th and 75th percentiles while the horizontal solid red line represents the 50th percentile of the observed data. The dashed lines represent the whiskers (extended to the most extreme data points not considered outliers) of the observed data. The outliers are shown as '+' marker symbol.

4.5.2 Comparison of generated IDF curves using each temporal stochastic downscaling method

The IDF curves generated using observations and disaggregated time series on the historical period are shown in Figure 4.5, representing one sample station, namely Russel station. IDF curves for the same station on the long-term period are shown in Figure 4.6 (next section). The IDF curves have been generated using annual maximum precipitation generated using all temporal stochastic disaggregation models for each return period of 2-, 5-, 10-, 50-, and 100-year events in the historical period and 3 future climate periods (short term: 2011-2040, the medium term: 2041-2070 and long term: 2071-2100). Figure 4.5 shows that IDF curves generated by KNN models and FO are generally closer to the IDF curves of observations than those generated using HKP and MRC. KNN (30) and FO are competing for first place. For two RCMs (CanESM2, CanRCM4 and EC-EARTH HIRHAM5), disaggregation using KNN (30) leads to the most realistic IDF curves. For the two others (EC-EARTH RCA4, GFDL RegCM4), FO seems to be the best.

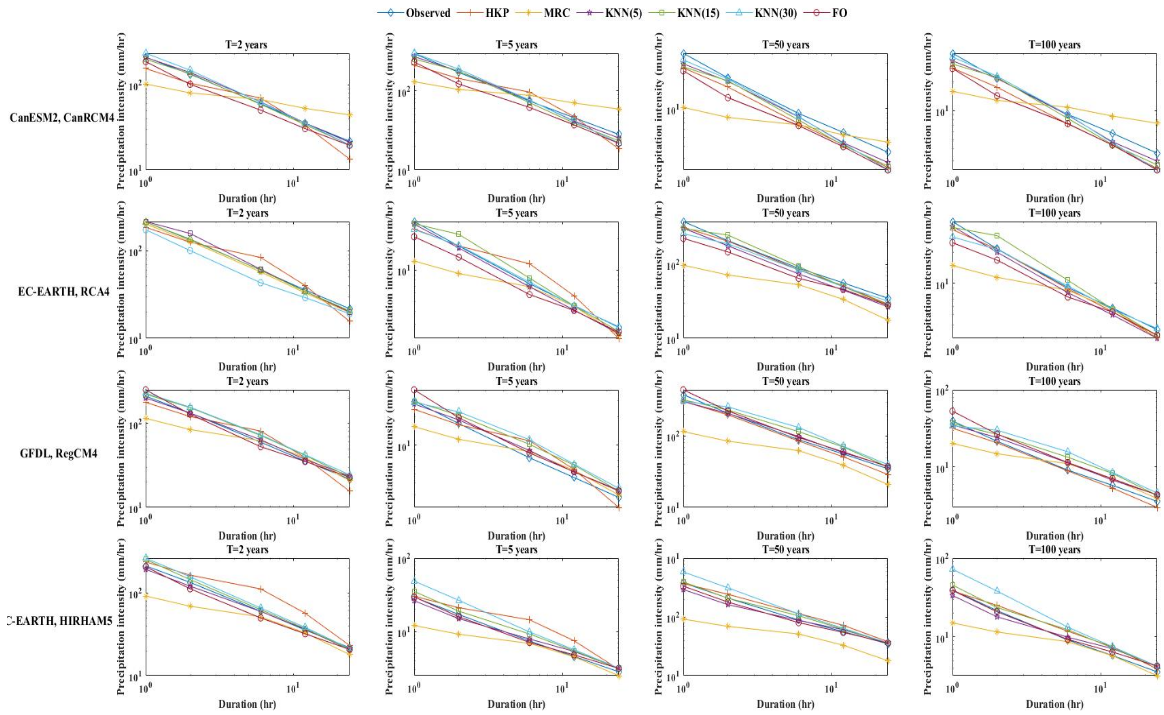

Figure 4.5 IDF curves of Russel Station resulting from KNN30 and FO disaggregation methods, historical period (all climate models); for return periods T=2, 5, 50 and 100 years.

4.6 Discussion

Given that subdaily finer-scale precipitation time series are essential for stormwater control and management in urban water systems, an efficient temporal disaggregation method is crucial due to the lack of such data in some locations. The subdaily time series can be directly used in rainfall-runoff models or transformed into IDF curves using the rational method. Six different temporal disaggregation models (the KNN disaggregation with neighbour sizes of 5, 15, and 30, the HKP, the MRC, and the proposed FO model) were applied to the downscaled precipitation time series of 4 station climate stations in the South Nation watershed. Various tests were used to assess the performance of the temporal disaggregation techniques. The main findings are recapitulated in Table 4.5.

Table 4.5 Summary of results

Temporal disaggregation method	Preservation of descriptive statistics in the generated hourly time series	Comparison of the generated annual maximums to observations using boxplots	Percentage of similarity of annual maximum time series using KS test	Comparison of IDF curves generated with disaggregated time series to IDF curves of observations
MRC	Mean and standard deviation preserved, underestimate skewness and kurtosis	Underestimates interquartile range and mean intensity at the one-hour time step	Systematic rejection	Significantly deviates from the IDF of observations
HKP	Mean and standard deviation preserved, underestimate skewness and kurtosis	Underestimates interquartile range and overestimates mean intensity at the 24-hours time step	Acceptance rate ranging from 20% to 70%	Significantly deviates from the IDF of observations
FO	Mean and standard deviation preserved, moderate underestimation of skewness. Kurtosis generally underestimated (3 out of 4 RCMs)	Interquartile range overestimated; reasonable estimation of mean intensity compared to MRC and HKP. Similar to KNN	Acceptance rate generally 100%, except for one station where it is 94%	Generally close to the IDF of observations
KNN	Mean and standard deviation preserved, reasonable estimation of skewness and kurtosis	Interquartile range overestimated; reasonable estimation of mean intensity compared to MRC and HKP. Similar to FO	Acceptance rates increase with neighbourhood. Generally, 100% for a neighbourhood of 30, except for two stations where it is 75%	Generally close to the IDF of observations. Agreement increases with the size of the neighbourhood.

All methods preserved the main descriptive statistics, such as the mean and standard deviation of the precipitation intensity. The three last comparison methods all seem to suggest that FO and KNN (30) are the most appropriate temporal disaggregation methods for the study area. Note that these results cannot be generalized and that different results could have been obtained if other climate stations or MRCs were used. It is also worth noting that the parameters of MRC and HKP were obtained by optimization, and its algorithm could have affected the final performance of the methods. The box plots of the projected precipitation intensities using the two best methods (FO and KNN(30)) are shown on Figure 4.6. Figure 4.7 shows the corresponding IDF curves. All figures suggest precipitation intensities will increase in the future in the study area, potentially making urban water infrastructure less safe as the impacts of global warming kick in.

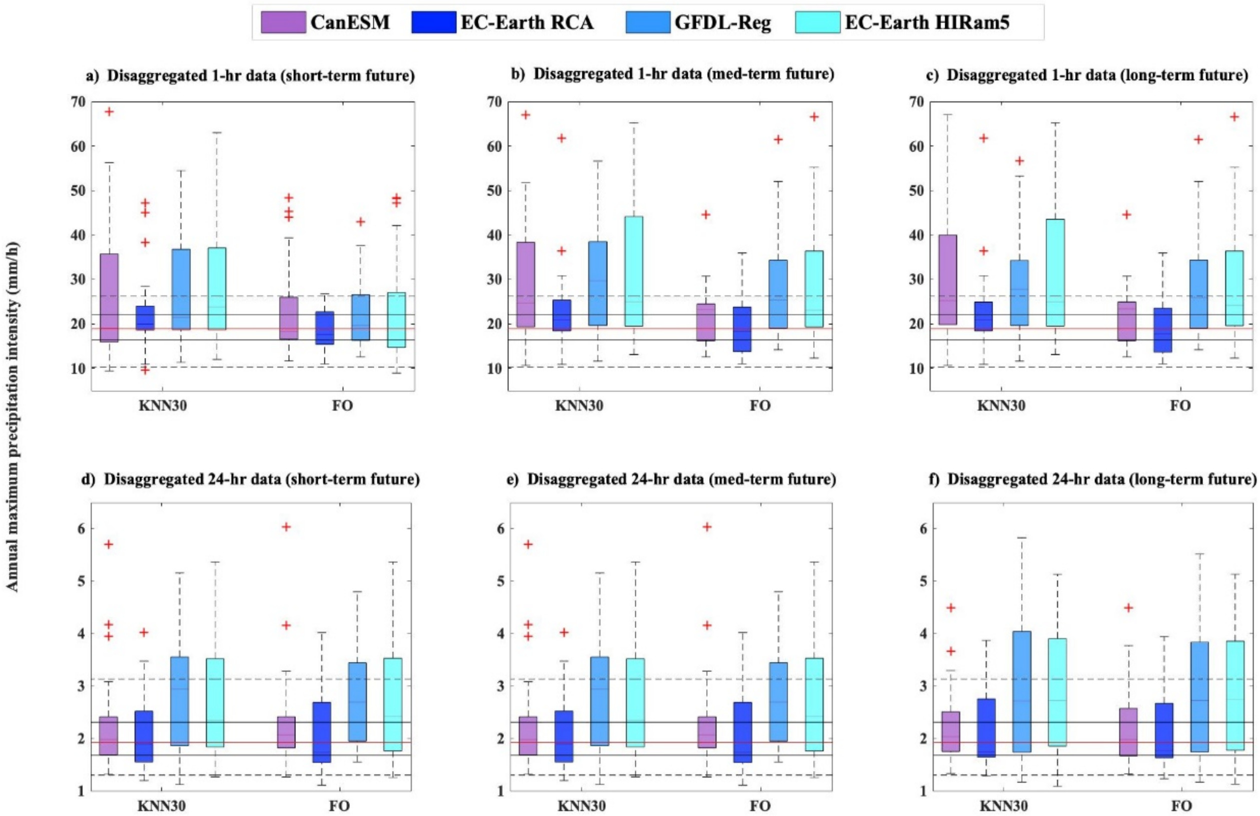

Figure 4.6 Grouped boxplot for KNN(30) and FO disaggregation methods and different RCMs in the future periods using a) 1-hr precipitation data in the short-term period, and b) 1-hr precipitation data in the medium-term period and c) 1-hr precipitation data in the long-term period. f) 24-hr precipitation data in the short-term period, and e) 24-hr precipitation data in the medium-term period, and d)24-hr precipitation data in the long-term period. The horizontal solid black lines represent the 25th and 75th percentiles while the horizontal solid red line represents the 50th percentile of the observed data. The dashed lines represent the whiskers (extended to the most extreme data points not considered outliers) of the observed data. The outliers are shown as '+' marker symbol.

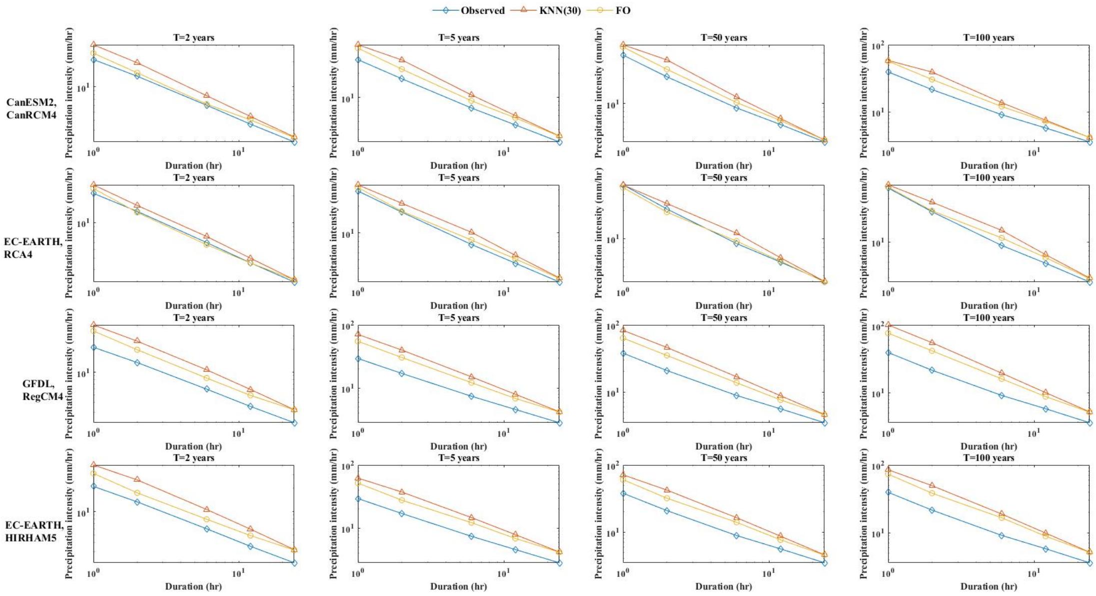

Figure 4.7. IDF curves of Russel Station curves resulting from KNN30 and FO disaggregation methods, long period (all climate models); for return periods T=2, 5, 50 and 100 years.

This study highlights the importance of carefully selecting the method used to generate future IDF curves, as two different methods can yield wildly different results. The resilience of urban infrastructure, public safety and global economic prosperity in the future is at stake and the blind use of a particular method can lead to maladaptation and costly infrastructure failure.

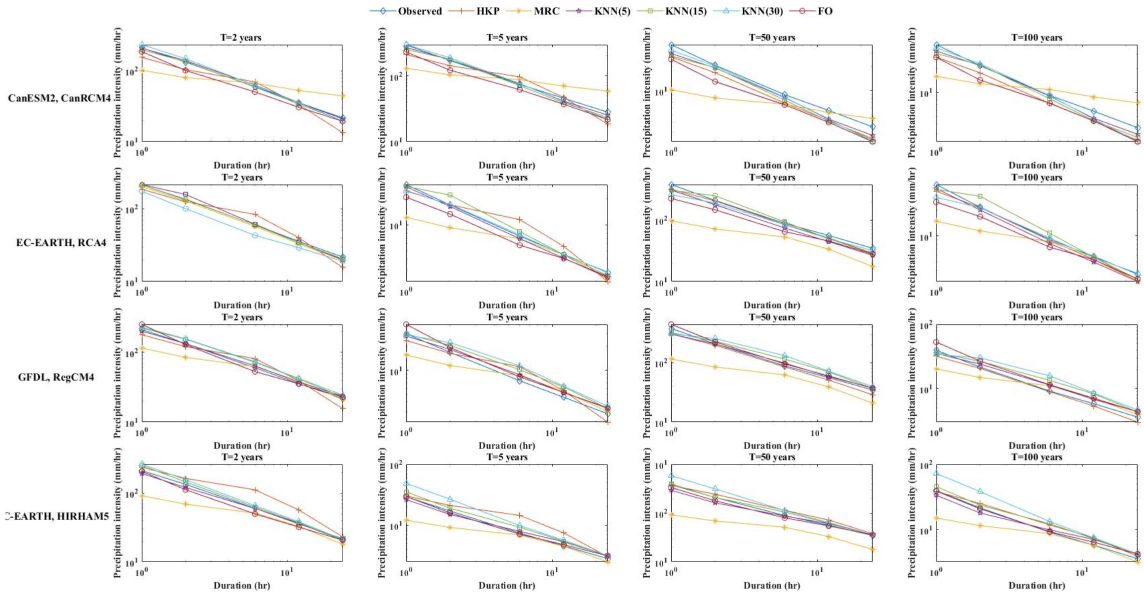

Figure 4.8 IDF curves at the Russel station for all disaggregation methods using different RCMs in the historical period for return period 2, 5, 50 and 100 years.

4.7 Conclusion

Given that precipitation projections are typically at a daily time scale, temporal disaggregation using techniques of variable complexity is often needed to evaluate the risk/performance of urban infrastructure in the future. Temporal disaggregation techniques have different levels of complexity and unequal performances, and the generated time series may not have the same statistical characteristics. In this paper, a simple steady-state stochastic disaggregation model that generates wet/dry day occurrence using a binomial distribution and precipitation intensity using an exponential distribution is proposed and compared to widely used temporal disaggregation methods: the multiplicative random cascade model (MRC), the Hurst- Kolmogorov process (HKP), and three versions of the K-nearest neighbour model (KNN) using the nonparametric KS test. Daily time series of future precipitation is generated by temporally downscaling the outputs of four RCMs using the quantile mapping (QM) method. Results show that for the selected RCMs and climate stations, while all methods are able to preserve descriptive statistics in the hourly time series, they perform very differently when it comes to annual maximum time series. The annual maximum time series generated using MRC systematically failed the KS test comparing them to observations, while HKP had low (20% to 70%) acceptance rates. FO and KNN (30) had acceptance rates close to 100%, and led to the most realistic annual maximum time series at subdaily and IDF curves, suggesting that complexity does not necessarily yield the best results.

4.8 References

Alodah, A., & Seidou, O. (2019). Assessment of Climate Change Impacts on Extreme High and Low Flows: An Improved Bottom-Up Approach. *Water*, *11*(6).

Garbrecht, J. D., Gyawali, R., Malone, R. W., & Zhang, J. C. (2017). Cascade rainfall disaggregation application in US Central Plains. *Environment and Natural Resources Research*, *7*(4), 30–43.

Gaur, A., & Lacasse, M. (2018). Multisite multivariate disaggregation of climate parameters using multiplicative random cascades. *Urban Climate*, *26*, 121–132.

Gumbel, E. J. (1935). *Les valeurs extrêmes des distributions statistiques*. *5*(2), 115–158.

Hurst, H. E. (1951). Long-term storage capacity of reservoirs. *Transactions of the American Society of Civil Engineers*, *116*(1), 770–799.

Jebari, S., Berndtsson, R., Olsson, J., & Bahri, A. (2012). Soil erosion estimation based on rainfall disaggregation. *Journal of Hydrology*, *436–437*, 102–110.

Koutsoyiannis, D. (2002). The Hurst phenomenon and fractional Gaussian noise made easy. *Hydrological Sciences Journal*, *47*(4), 573–595.

Koutsoyiannis, D., & Cohn, T. (2008). *The Hurst phenomenon and climate (solicited)*.

Koutsoyiannis, D., & Onof, C. (2001). Rainfall disaggregation using adjusting procedures on a Poisson cluster model. *Journal of Hydrology*, *246*(1–4), 109–122.

Koutsoyiannis, D., Paschalis, A., & Theodoratos, N. (2011). Two-dimensional Hurst–Kolmogorov process and its application to rainfall fields. *Journal of Hydrology*, *398*(1–2), 91–100.

Licznar, P., Łomotowski, J., & Rupp, D. E. (2011). Random cascade driven rainfall disaggregation for urban hydrology: An evaluation of six models and a new generator. *Atmospheric Research*, *99*(3–4), 563–578.

Lu, Y., Qin, X. S., & Mandapaka, P. V. (2015). A combined weather generator and K-nearest-neighbour approach for assessing climate change impact on regional rainfall extremes. *International Journal of Climatology*, *35*(15), 4493–4508.

Massey Jr, F. J. (1951). The Kolmogorov-Smirnov test for goodness of fit. *Journal of the American Statistical Association*, *46*(253), 68–78.

Mearns, L., McGinnis, S., Korytina, D., Arritt, R., Biner, S., Bukovsky, M., Chang, H.-I., Christensen, O., Herzmann, D., Jiao, Y., Kharin, S., Lazare, M., Nikulin, G., Qian, M., Scinocca, J., Winger, K., Castro, C., Frigon, A., & Gutowski, W. (2017). *The NA-CORDEX dataset* [NetCDF]. UCAR/NCAR.

Molnar, P., & Burlando, P. (2005). Preservation of rainfall properties in stochastic disaggregation by a simple random cascade model. *Precipitation in Urban Areas*, *77*(1), 137–151.

Müller, H., & Haberlandt, U. (2015). Temporal Rainfall Disaggregation with a Cascade Model: From Single-Station Disaggregation to Spatial Rainfall. *Journal of Hydrologic Engineering*, *20*(11), 04015026.

Müller, H., & Haberlandt, U. (2018). Temporal rainfall disaggregation using a multiplicative cascade model for spatial application in urban hydrology. *Journal of Hydrology*, *556*, 847–864.

Olsson, J. (1998). Evaluation of a scaling cascade model for temporal rain-fall disaggregation. *Hydrology and Earth System Sciences*, *2*(1), 19–30.

Olsson, J., & Berndtsson, R. (1998). Temporal rainfall disaggregration based on scaling properties. *Use of Historical Rainfall Series for Hydrological Modelling*, *37*(11), 73–79.

Park, H., & Chung, G. (2020). A Nonparametric Stochastic Approach for Disaggregation of Daily to Hourly Rainfall Using 3-Day Rainfall Patterns. *Water*, *12*(8), 2306.

Sharif, M., & Burn, D. H. (2007). Improved K-nearest neighbor weather generating model. *Journal of Hydrologic Engineering*, *12*(1), 42–51.

Sharif, M., Burn, D. H., & Hofbauer, K. M. (2013). Generation of Daily and Hourly Weather Variables for use in Climate Change Vulnerability Assessment. *Water Resources Management*, *27*(5), 1533–1550.

Srikanthan, R., Sharma, A., & McMahon, T. (2006). Comparison of two nonparametric alternatives for stochastic generation of monthly rainfall. *Journal of Hydrologic Engineering*, *11*(3), 222–229.

Srikanthan Ratnasingham & McMahon Thomas A. (1982). Stochastic Generation of Monthly Streamflows. *Journal of the Hydraulics Division*, *108*(3), 419–441.

Uraba, M. B., Gunawardhana, L. N., Al-Rawas, G. A., & Baawain, M. S. (2019). A downscaling-disaggregation approach for developing IDF curves in arid regions. *Environmental Monitoring and Assessment*, *191*(4), 245.

Wey, K. M. (2006). *Temporal Disaggregation of Daily Precipitation Data in a Changing Climate*. 178.

Chapter 5. Climate Change impact on a Municipal Water System with Combined Sewers. Case study of Port Dalhousie, Ontario, Canada

5.1 Abstract

The performance of urban stormwater drainage systems depends on multiple factors, including population growth, urbanization, and future precipitation regime in the region. Increased water bodies contamination resulting from climate change-related risks is a concern for municipalities like Port-Dalhousie, where part of the sewer system is still combined. Heavy rainfall events and melting snow currently cause the wastewater treatment plant to reach its capacity, resulting in the discharge of untreated or partially treated water into water bodies (also known as overflows). The situation may become worse in the future as such events become more frequent. The performance of the Port-Dalhousie sewer system and treatment plant under a changing climate is examined in this study using a SWMM (Stormwater Management Model) model. The model was forced with downscaled and temporally disaggregated precipitation outputs of the Canadian Regional Climate Model at the Port Dalhousie station, simulated under emission scenario RCP8.5. The temporal disaggregation was done using three versions of *k*-nearest neighbour (KNN5, KNN15, and KNN30) as well as Fahad-Ousmane (FO) method. The impact of climate change on the frequency, volume, and quality of combined sewer overflows and other hydraulic parameters is examined. Results indicate that the total bypass flow volume as well as the maximum flow values gradually increase in the future periods. The pollution levels are also projected to increase severely and potentially causing more burden on the current infrastructure.

Keywords: Climate change, SWMM, Water quality modelling, Flow routing modelling, Stormwater collection system, Temporal stochastic disaggregation.

5.2 Graphical Abstract:

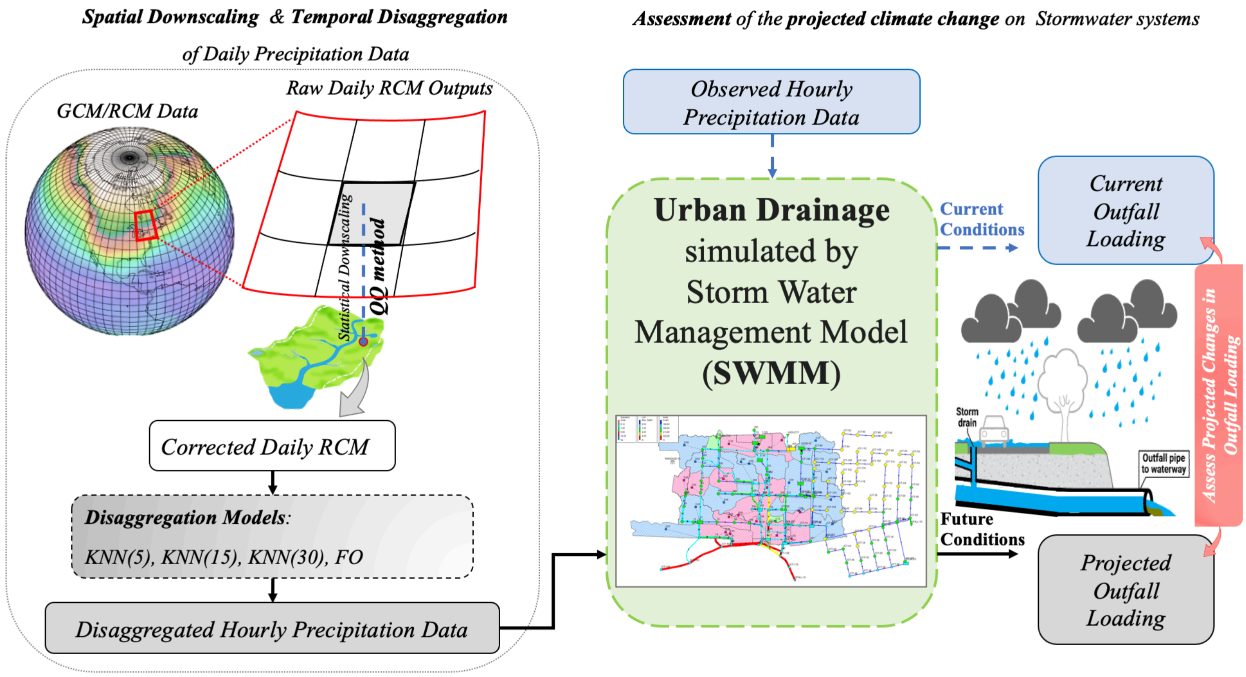

5.1 Introduction

Stormwater and sanitary sewer systems are critical infrastructures that can lead to flooding, water pollution, traffic disruption, or power grid failure. Limited rehabilitation budgets and high replacement costs have prevented many Canadian cities from converting older combined sewer systems into separate ones. When part of the system is combined, wastewater treatment plants receive a mix of stormwater and sanitary wastes. Due to heavy rainfall or melting snow, the plant's capacity may be overwhelmed during extreme wet weather events, and consequently releasing untreated water into the nearest water body which might lead to a risk of contamination of aquatic ecosystems and other water users. Economically, flooding, and consequently overflows, is Canada's most expensive weather-related disaster (Decent and Feltmate, 2018). In terms of public health and safety, overflows could cause many poisonings and life-threatening illnesses to people exposed to these discharges.

Climate change is a factor that is likely to make further disruptions in the frequency and volume of combined sewer overflows. The impact of climate change on the performance of urban water systems and potential mitigation measures for these impacts has received significant attention from the research community. Inadequate performance of storm water infrastructure due to projected changes in precipitation depths and intensities under different climate scenarios poses challenges to water professionals (Moglen & Rios Vidal, 2014; Andimuthu *et al.,* 2019; Zhang et al., 2019; Patel *et al.,* 2023). Projected changes in climate conditions may have effects on runoff volume and pollution particularly on urban drainage systems at a city scale (Semadeni-Davies *et al*., 2008; Krieger *et al*., 2013; Fortier and Mailhot, 2015; Zahmatkesh *et al*., 2015; Mohammed *et al*., 2021;

Hussain *et al*., 2022). Such vulnerability was repeatedly modeled using the U.S. EPA Storm Water Management Model (SWMM) in cold regions (e.g. Moghadas *et al*., 2018), arid and semi-arid regions (e.g Hussain *et al.*, 2022). Also, Burge *et al,*. (2012) evaluated the impacts of climate change on water system design using multiple climate scenarios and found that future climate would maximize the efficiency of urban water design and lead to system stability by understanding the potential climate change impact and comprehensible adaption to its adverse consequences. Luan *et al.*, (2017) investigated changes in urban stormwater quantity and quality resulting from climate change using the USS Environmental Protection Agency Storm Water Management Model (SWMM) and concluded that urbanization considerations significantly impact flow quantity and quality more than climate change. Zhang *et al*., (2019) evaluated the reliability of stormwater treatment under climate change. They found a minimal difference in water system performance in pollution removal; thus, the uncertainty level was high in systems such as wetland areas and land used by the catchment. O'Hara and Georgakakos (2008) quantified the impacts of climate change on an urban water system by estimating the amount of storage required to meet urban water demand in the future. The study found considerable uncertainty in the projected data and concluded that there is a need to increase storage capacity, possibly at a high cost. Alamdari *et al.,* (2017) assessed the effects of climate change on water quantity and quality by using a SWMM model of the Difficult Run Watershed located in Fairfax County, Virginia, USA. This study found that climate change will lead to increased wash-off load, total suspended solids, and total nitrogen. Several other studies have been conducted on sustainable solutions, such as storm biofilters and wetland ponds, to mitigate the adverse climate change impacts and urbanization (Bach *et al*., 2013;

Luan *et al.,* 2017; Zhang *et al.,* 2019) . Sharma *et al.,* (2016) found that the total suspended solids (TSS) concentration from a retention pond will potentially increase due to climate change.

This research will focus on the collection system connected to the Port Dalhousie wastewater treatment plant, shown in figure 5.1.

The system is located in the municipality of St. Catherines, in the Niagara region in Ontario, Canada. Port Dalhousie is one of the two wastewater treatment plants in the municipality and services a population of approximately 75,000 in the western district of the city of St. Catherines and parts of the city of Thorold, covering about 3,000 ha. The population of the municipality of St. Catherines is predicted to increase modestly because the development has primarily reached the limits of the designated urban area. In 2014, the population of St. Catherines was estimated to be 135,940, and the projected population would be 167,480 in 2041. Part of the sewer system is still combined, and overflows are not uncommon during wet events.

This paper would help to achieve the following objectives:

- Develop a SWMM model of the system that can simulate both water quantity and quality
- Force the system with projected hourly precipitation generated by downscaling and temporally disaggregating precipitation outputs of the Canadian Regional Climate Model (CRCM) at the Port Dalhousie station, simulated under emission scenario RCP8.5. The temporal disaggregation was accomplished using the methods of Fahad-Ousmane and K-nearest neighbour (5, 15, and 30).

Examine the impacts of climate change on the system's performance by estimating the percentage of the change in the total volume.

5.2 Material and methods

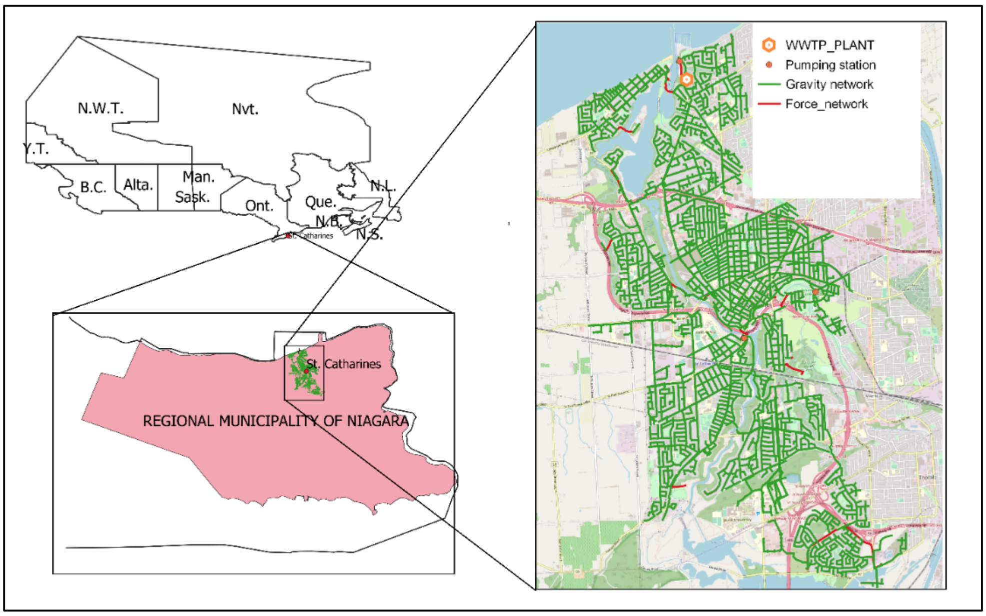

Figure 5.1 Port Dalhousie wastewater treatment plant and associated sanitary and stormwater network.

5.2.1 Study area

The municipality of Niagara has 427,421 residents spread over an area of 1,852 km^2 located in Ontario, Canada (Figure 5.1). Sewage in the municipality is conveyed to two wastewater treatment plants (Port Dalhousie site). The Port Dalhousie WWTP processes approximately 80,000 megaliters of sewage each year (Niagara Region, 2020). During extreme wet weather events, the sewer's capacity does not manage to retain all the excess water which goes to the wastewater treatment plant; therefore, a large part of this water is discharged into nature without being treated.

5.2.2 Wastewater treatment plant overview and overflows statistics

Port Dalhousie Wastewater Treatment Plant is a conventional activated sludge with screening, de-gritting, primary settling, aeration, chemical phosphorus removal, secondary clarification, and seasonal disinfection utilizing sodium hypochlorite. It is also classified as a secondary sewage treatment plant.

The plant operates at 67% of its rated capacity of 61,350 m3/day. The influent raw wastewater appears to be low to medium strength for carbonaceous biochemical oxygen demand (CBOD5), total suspended solids (TSS), and TKN (Total Kjeldahl Nitrogen) and low strength for TP (Total Phosphorus). Peak flows during wet weather events exceed the maximum capacity of 100,000 m3/day. Flows above the plant's peak capacity are bypassed at a diversion chamber upstream of the influent flow meter. The WWTP treats municipal wastewater from domestic, industrial, and commercial conveyors connected to the collection system. The observed influent characteristics are outlined in Table 5.1.

Table 5.1 Influent characteristics of municipal wastewater treated by the WWTP. (Water Environment Association of Ontario, 2020)

Parameter	2016	2017	2018	2019
Total Flow (1,000 m^3)	10,839	12,878	12,720	13,240
Avg Daily flow (1,000 m^3)	26.616	35.278	34.85	36.576
Peak day flow (1,000 m^3)	94.007	138.576	163.02	127.309
TSS (mg/L)	243	231	336	233
$TBOD_5$ (mg/L)	183	179	221	170

TP (mg/L)	4.28	4	4.4	3.81
TKN (mg/L)	39	38	39	37

On average, the Port Dalhousie WWTP meets the ECA effluent limits for all parameters and objectives for CBOD5 and TSS. In contrast, the yearly average TP concentration exceeded the 0.5 mg/L aim in 2006 at 0.52 mg/L.

Table 5.2 ECA effluent requirements of the PDWWT**P** (Water Environment Association of Ontario, 2020)**.**

Effluent Parameter	**Effluent monthly average concentration**		**Effluent monthly average daily loading**	
	Limit	**Objective**	**Limit**	**Objective**
$CBOD_5$	25 mg/L	15 mg/L	1,534 k /d	920 kg/d
TSS	25 mg/L	15 mg/L	1,534 kg/d	920 kg/d
TP	1.0 mg/L	0.5 mg/L	61.5 kg/d	30.7 kg/d
Total Residual Chlorine	0.02 mg/L	Non-detectable	N/A	N/A
E.Coli (April 1 to Oct. 31)	200 CFU/100mL	100 CFU/100mL	N/A	N/A

The last overflows for the Port Dalhousie Wastewater Treatment Plant site were recorded on February 24, 2021. In 2019, 36 bypass/overflow events occurred in the treatment plant and its collection system as 264.8 megalitres of untreated water were spilled into the nearby Twelve Mile Creek (Water Environment Association of Ontario, 2020).

5.2.3 Data collection

The 1976-2005 hourly observed precipitation time series from the Port Dalhousie climate station located in St. Catharines, Ontario (longitude -79.2667; latitude 43.1833) were obtained from Environment Canada. The 1976-2100 daily time series at the port Dalhousie climate station were extracted from the outputs of the Canadian regional Climate model, simulated under emission scenario RCP 8.5. A database of the sewer network (gravity pipes and force mains), pumping stations and stormwater inlets were obtained from the city. However, note that all pipe invert elevations are documented, and pipe material was unavailable. Land use in the study area was acquired from Southern Ontario Land Resource Information System (SOLRIS) Version 2.0.

5.2.4 Methodology

SWMM is a discrete simulation model that is physically oriented to simulate the amount and quality of stormwater tributaries using the following physical processes: surface runoff, groundwater, flow routing, water quality routing, infiltration, snowmelt, and surface ponding. Each surface of a subcatchment is modelled as a nonlinear reservoir. Precipitation and any designated upstream subcatchments provide inflow. Infiltration, evaporation, and surface runoff are all examples of outflows. Surface runoff per unit area occurs only when the water level in the reservoir surpasses the maximum Depression Storage level (DS). Designers frequently utilize the Natural Resources Conservation Service's model (NRCS) where soils are categorized into four types, A, B, C, and D based on their minimal infiltration rate. The final NRCS curve number may then be used in a computer model to calculate the peak runoff for the location. The flow routing inside a pipe or conduit link in SWWM is governed by the conservation of mass and momentum equations for progressively changing unsteady flow (the Saint-Venant flow equations). Only the dynamic wave routing equation is used in this study to determine how water travels down a wire or conduit in a water tunnel. The Saint-Venant equations' one-dimensional domain is solved using dynamic wave routing equations. The same technique is used to model water quality within storage unit nodes for conduits. Integrating the conservation of mass with average values for parameters that may fluctuate over time, such as flow rate and conduit volume, yields the concentration of a constituent departing the conduit at the end of a time step. The quality of water departing other nodes with no volume is the mixed concentration of all the water entering the node.

The first step in the methodology consists of developing a SWMM model of the network and treatment plan. Once the model is developed, the analysis will be done following the flowchart presented in Figure 5.2. First, the daily outputs extracted from the CRCM will be downscaled using quantile mapping method. The daily time series will then be temporally disaggregated at the hourly time step using KNN (30) and the Fahad-Ousmane (FO) methods presented in Alzahrani *et al.*, (2023).

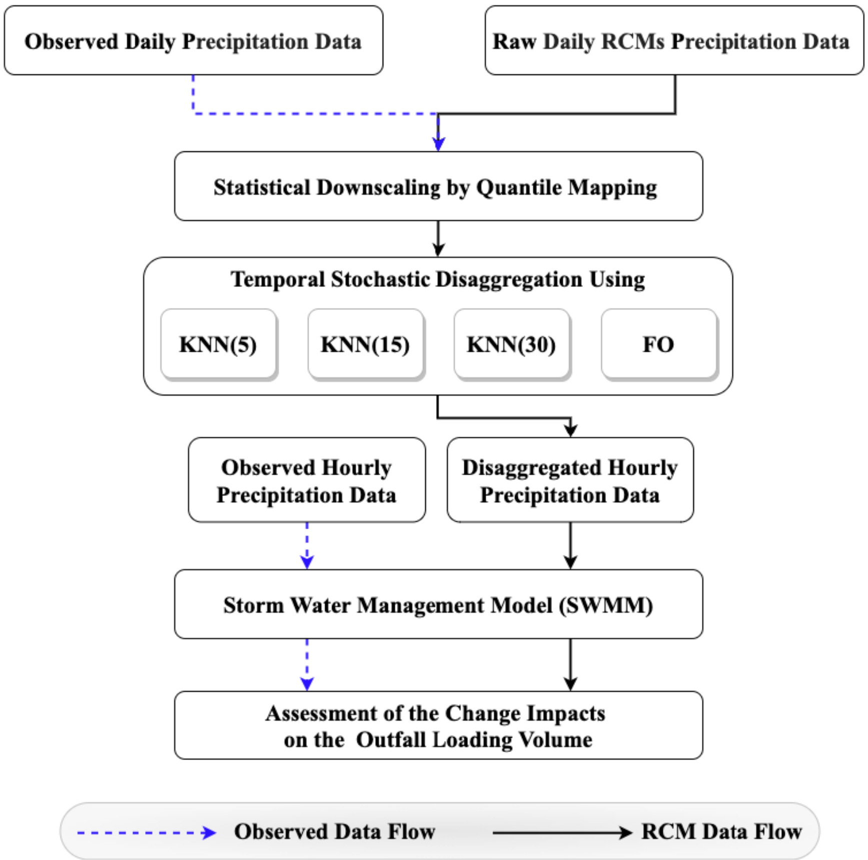

Figure 5.2 Flowchart of the methodology.

5.2.5 SWMM model development

The SWMM model was developed according to Southern Ontario Land Resource Information System (SOLRIS) Version 2.0. The following steps were used to develop the model:

1. Gravity pipes in the sanitary network were transferred from geographic information system (GIS) files to SWMM. When invert elevation was unavailable, it was estimated by assuming a pipe slope of 2%.
2. Force mains were represented by pumps with a substantial capacity.
3. All pipes were assumed to have a Manning's roughness coefficient of 0.011.
4. Stormwater was assumed to enter the system in pipes with a diameter above 1.5 m.
5. The sanitary flow was calculated assuming a population density of 307 people per square kilometers. Thiessen polygons were used to identify the contributing area of each sanitary inlet. The urbanized area in the Thiessen polygon was extracted from the Southern Ontario Land Resource Information System (SOLARIS) Version 2.0.
6. Thiessen polygons were used to evaluate the contributing area of each storm inlet (Figure 5.4). The curve number for each Thiessen polygon was obtained using land use classes in the Southern Ontario Land Resource Information System (SOLRIS) Version 2.0. Flow from each Thiessen polygon entered the system in the first node using the drainage system with a diameter above 1.5m.
7. Pumping stations are represented in the model by a reservoir, a pump, and an overflow weir. The pump is set to provide the maximum flow provided by the client in the pumping station. When the inflow is above the capacity of the pump, the reservoir fills, and an overflow occurs. Three pumping stations were represented in the system: Renown, Argyle

and Glendale (Figure 5.4). The team did not have enough information to model the remaining pumping stations.

8. The wastewater treatment plant was represented in the model by a reservoir, a pump, and an overflow weir (Figure 5.3). However, in this case, the capacity of the pump is the maximum treatment capacity of the station (100,000 m^3/day=1276 l/s). When the inflow is above the capacity of the pump, the reservoir fills in, and a bypass occurs.

A) Collection network and catchments (Thiessen polygons)

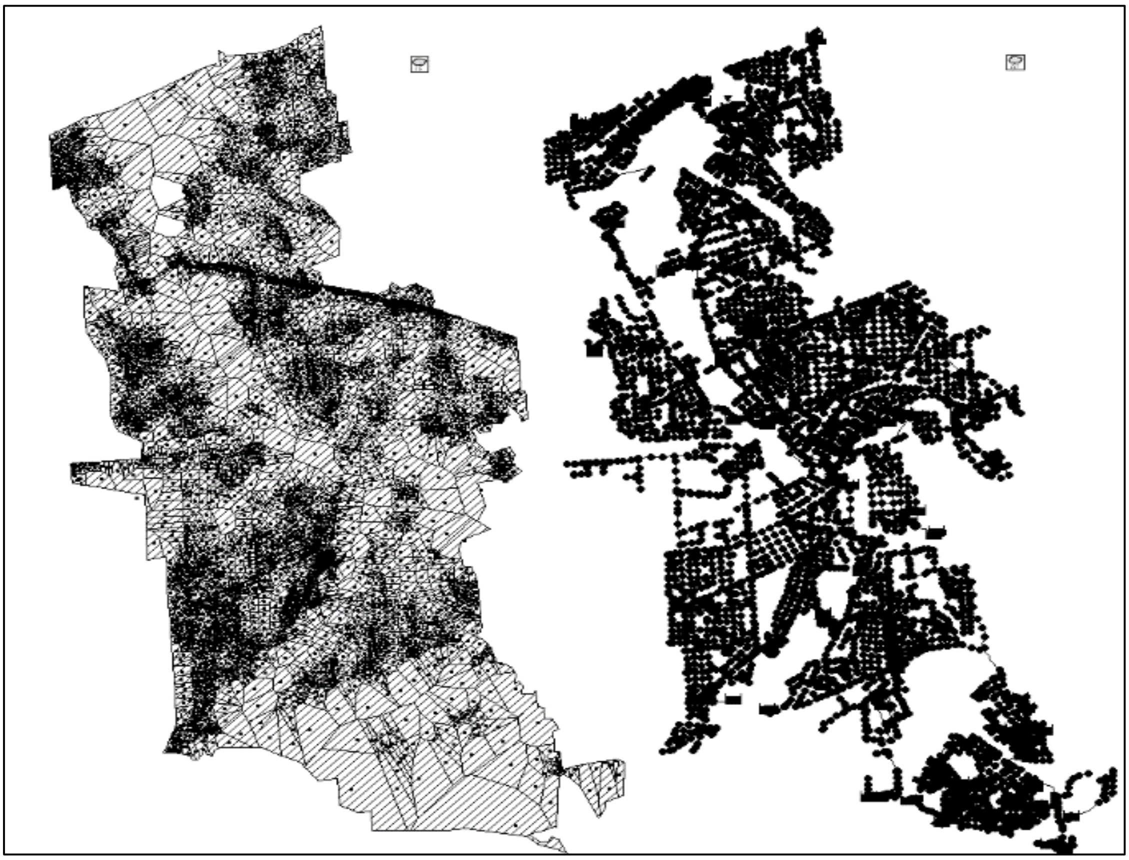

Figure 5.3 Representation of the network and catchments in SWMM.

5.2.6 RCM outputs downscaling

The regional climate models' (RCMs') outputs are downscaled using the quantile mapping technique (QM). The QM method consists of remapping the probability density function (PDF) of the uncorrected RCM series in combination with the probability of the observed data series. The following formula produces the corrected RCM to CDF:

$$X_{Corrected}=F^{-1}{}_{Observed}\,(F_{RCM}(X_{RCM})) \qquad \text{Eq (5.1)}$$

where $\boldsymbol{X_{RCM}}$ adds to the RCM data before projection. In practice, Equation (4.1) is replaced by the following mapping function between GCM outputs and observations:

$$\begin{bmatrix} (X_{observation})_{sorted,1} & (X_{RCM})_{sorted,1} \\ (X_{observation})_{sorted,2} & (X_{RCM})_{sorted,2} \\ . & \\ . & \\ . & \\ (X_{observation})_{sorted,N} & (X_{RCM})_{sorted,N} \end{bmatrix} \qquad \text{Eq (5.2)}$$

The limitation of this approach is that it cannot predict the values beyond the range of historical data. The reference period is split into validation and calibration. Equation (5.2) is fitted on the calibration period and applied to the validation and future periods. To avoid any bias resulting from oscillations in the observed precipitation time series, the calibration period of the data set contains all data series from 1976 to 1991, and the validation period covers the data series from 1992 to 2005.

5.2.7 Temporal disaggregation techniques

The SWMM model requires time series of precipitation and temperatures at a sub-daily (1h) time step. Two temporal downscaling techniques are considered: the KNN disaggregation technique and the Fahad-Ousmane (FO) model.

5.2.7.1 The k-nearest neighbour disaggregation model

KNN is a particular case of the fragment (MF) method, a nonparametric approach commonly used by researchers. The fragment is selected from historical hourly precipitation in a sample of neighbours with similar precipitation amounts. The general formulation of the MF is given in Equations (5.3) and (5.4). Equation (5.3) contains w_i as the weight that will be computed, hi is the data from the series selected to produce fragments, and n is the number of data points in the series (24 hours).

$$w_i = \frac{h_i}{\sum_{i=1}^{n} h_i} \qquad \text{Eq (5.3)}$$

Then, each fragment is multiplied by daily data d in Equation (5.4) to obtain the new hourly data or disaggregated values.

$$h_i' = w_i \times d \qquad \text{Eq (5.4)}$$

The hourly series of data used to estimate fragments could be chosen randomly; however, this would lead to inadequacy in the most critical statistic properties (Srikanthan and McMahon, 1982). Therefore, the best choice is to compare the total disaggregated daily precipitation with close total daily precipitation before the disaggregation process (Wey, 2006).

The neighbours are selected in a temporal window to preserve the seasonal characteristics of precipitation. Note that the sliding window is based on the Julian calendar and spans all years in the data. The KNN with the most negligible difference in precipitation amount is selected. One neighbour is then sampled from the set and used to calculate the fragment. The probability of sampling neighbour ***j*** is:

$$p(j) = \frac{{}^{1}/_{|P(j)-P(t)|}}{\sum_{i=1}^{k}(|P(i)-P(t)|)} \qquad \text{Eq (5.5)}$$

where ***p(j)*** is the precipitation amount of neighbour j and ***P(s)*** is the precipitation amount on the simulation day.

5.2.7.2 The Fahad-Ousmane disaggregation model

The Fahad-Ousmane (FO) model is a steady-state stochastic disaggregation model that applies analog signs of precipitation events and hourly scale series. The binormal distribution estimates the probability of dry or wet event occurrence for disaggregation. Intensity during a wet day is simulated using the exponential distribution. The model generates wet hours (hours with precipitation above 1 mm) using a binomial distribution with parameter *p*, and for each wet hour, precipitation intensity using an exponential distribution with parameter α. The parameters are fitted month by month using observed data in the calibration period as follows:

a) Estimate all hourly precipitation for month M.
b) Estimate p as the ratio of hours with precipitation higher than 1 mm to the total number of hours.
c) Create a time series of hours with precipitation above 1 mm.
d) Fit the exponential distribution to the above time series to obtain α.

The generation of hourly precipitation for a day with precipitation amount p_{day} is calculated as follows:

a) If p=0, set all hourly values to 0.
b) If p>0,
    a. Generate a series of 0 (dry hours) and 1 (wet hours); repeat until you obtain at least one non-zero value.
    b. For each wet hour *h*, is a sample from the exponential distribution with the parameter α to obtain $p_{\text{hour(h)}}$; set $p_{\text{hour(h)}}$ to 0 for dry hours.

The final precipitation for each hour of the day is set to:

$$p_{day} = \frac{P_{hour}(h)}{\sum_{i=0}^{24} P_{hour}(i)} \qquad \text{Eq (5.6)}$$

5.3 Results

5.3.1 Validation of the simulated hourly time series

The model validation procedures are very similar to what was applied in [21]. The KS test compares the distribution of the disaggregated time series to that of the observed time series at time steps going from 1h to 24h. Table 3 displays the p-values resulting from KS-test when comparing disaggregated time series to observations for the 1h and 24h time steps. The null hypothesis is accepted for almost all disaggregation techniques and all-time steps except the FO model of validation period the null is rejected, therefore, meaning that the distribution of the disaggregated time series is similar to that of observations.

Table 5.3 Results of Calibration and validation of temporal disaggregation models.

Model and period	1-h	24-h
FO, Calibration Period	Accepted (p=0. 6)	Accepted (p=0.6)
FO, Validation Period	Rejected (p=0.001)	Accepted (p=0.6)
KNN(5), Calibration Period	Accepted (p=0.5)	Accepted (p=0.8)
KNN(5), Validation Period	Accepted (p=0.5)	Accepted (p=0.7)
KNN(15), Calibration Period	Accepted (p=0. 9)	Accepted (p=0.9)
KNN(15), Validation Period	Accepted (p=0.3)	Accepted (p=0.3)
KNN(30), Calibration Period	Accepted (p=0.9)	Accepted (p=1)
KNN(30), Validation Period	Accepted (p=0.6)	Accepted (p=0.9)

5.3.2 Water Quality Modelling

The advantage of the SWMM software is the ability to model water quality for particular urban watershed areas depending on the wastewater components and land used. In the simulation, the initial concentration values of wastewater effluent characterization are essential to simulate the expected values in the future climate period. Tables 4, 5, and 6 display the initial buildup and wash off values of pollutants such as TP, TBOD and CBOD (Tavakol-Davani, 2016); because these values will be applied in the land uses configuration. Furthermore the configuration includes a commercial and residential development with both functions Exponential and "Event mean concentrations (EMC) used in models for predicting wastewater chemical concentration from stormwater runoff and stormwater treatment practices or pollution prevention practices." Moreover, they are used in observation and future climate change scenarios.

Table 5.4 Initial effluent values for water quality modelling, commercial and residential development (Tavakol-Davani, 2016).

Pollutants name	Unit	Inflow&Infiltration concentration	Initial concentration	Decay Coefficient
Total Phosphorus (TP.)	MG/L	4	4	0.41
Total Biological Oxygen Demand (TBOD)				
Carbonaceous Biochemical Oxygen Demand (CBOD)				

Table 5.5 Initial buildup values of effluent for water quality modelling commercial and residential development (Tavakol-Davani, 2016).

Pollutants name	Function	Max buildup	Rate constant	normalizer
Total Phosphorus (TP.)	Exponential function	0.13	0.2	Area
Total Biological Oxygen Demand (TBOD)				
Carbonaceous Biochemical Oxygen Demand (CBOD)				

Table 5.6 Initial washoff values of effluent for water quality modelling, commercial and residential development(Tavakol-Davani, 2016).

Pollutants name	Function	Coefficient	Exponent
Total Phosphorus (TP.)	Event Mean Concentration (EMC)	180	0
Total Biological Oxygen Demand (TBOD)			
Carbonaceous Biochemical Oxygen Demand (CBOD)			

5.3.3 SWMM Model validation

Storm and sanitary models have been calibrated the by changing the parameters of subcatchaments configuration, such as impervious percentage and slope, using trial and error. Bypass volume has been simulated to be 85.9 ML in 2016, which is very close to the observed volume of 85.5 ML. Given the complexity of the model, they only simulated the events that led to an overflow in the system.

5.3.4 SWMM Model performance under historical and future climate scenario

The outputs of the CRCM of the location of Port Dalhousie in the city of St. Catharines, ON, were statistically downscaled using quantile mapping on the historical (1976-2005), short term (2011-2040), medium term (2041-2070) and long-term future climate period (2071-2100). The resulting daily time series were temporally disaggregated to one hour time step using KNN (30) and FO models. The SWMM model was run using the observed climate and the disaggregated time series. Table 7 presents a comparison of effluent discharge volumes obtained using the observed climate and the disaggregated time series. All disaggregated time series lead to an underestimation of the frequency of effluent discharge to natural water bodies (1.9% when the observed climate is used, 0.2% to 0.5% with disaggregated time series are used). However, the total volume of untreated water is in the same range (187.5/Year ML when using observations, 201.01 ML/year to 220.9 ML/year using disaggregated time series, with FO leading to the volume which is closest to observations). The volumes of treated water are also consistent (10380.1 ML/year when using observations, 10482 ML/Year to 14617.7 ML/Year using disaggregated time series, with FO leading to the volume which is closed to observations). These results indicate that the model reasonably captures the combined sewer overflow volume in the study area.

The model was used to estimate the WWTP effluent discharge in the future using the disaggregated time series, and the results are presented in tables 7 and 9. Apart from KNN (30), where the frequency of combined sewer overflow (CSO) showed an unexpected uptick (0.5% to 3.22% from the historical to the short term period, before decreasing to 0.9% in the medium-term period and 1.1% in the short term period), all simulations show a steady increase in CSO frequency and volumes in the future. Table 10 shows that severe water quality degradation is expected. Table 10 presents the percentage of changes in water quality level. The percentage is assumed to be potentially increased in all future climate periods. For KNN(30) model, as the frequency percentage decreased in each future climate period, the percentage of the change decreased from short (60% of TP and TBOD) to long periods (70% TP and TBOD).

Table 5.7 Summary of effluent discharge at Outfall Loading under historical climate scenario of each temporal downscaling model KNN(5, 15 and 30) and (FO).

Historical period (observed climate)		
Outfall Node	WWTP untreated	WWTP treated
Flow Frequency Percentage	1.93	99.99
Average Flow m^3/s	1.7	2.03
Maximum Flow m^3/s	9.4	6.9
Total Volume 10^6 litre	5,623.4	311,411.6
Volume per year 10^6 litre/year	187.5	10,380.4
Historical period (disaggregated time series)		
FO		
Outfall Node	WWTP untreated	WWTP treated
Flow Frequency Percentage	0.5	100
Average Flow m^3/s	2.3	2.04
Maximum Flow m^3/s	4.53	4.6
Total Volume 10^6 litre	6030.23	314,460.2
Volume per year 10^6 litre/year	210.02	10,482.01
KNN(5)		
Outfall Node	WWTP untreated	WWTP treated
Flow Frequency Percentage	0.65	100
Average Flow m^3/s	1.1	4.5
Maximum Flow m^3/s	8.75	11.6
Total Volume 10^6 liter	6067.2	423,676.2
Volume per year 10^6 liter /year	215.34	14,122.5
KNN(15)		
Outfall Node	WWTP untreated	WWTP treated
Flow Frequency Percentage	0.2	99
Average Flow m^3/s	2.6	1.4
Maximum Flow m^3/s	7.83	6.45
Total Volume 10^6 liter	6125.4	438,530.6
Volume per year 10^6 liter/year	217.63	14,617.7
KNN(30)		
Outfall Node	WWTP untreated	WWTP treated
Flow Frequency Percentage	0.3	100
Average Flow m^3/s	2.9	1.5
Maximum Flow m^3/s	0.9	3.48
Total Volume 10^6 liter	6235.2	438,170.1
Volume per year 10^6 liter/year	230.16	14,604.7

Table 5.8 Summary of effluent discharge at Outfall Loading under historical and future climate scenarios,

KNN (30) model	Short-term period		Medium-term period		Long-term period	
Outfall Node	WWTP untreated	WWTP treated	WWTP untreated	WWTP treated	WWTP untreated	WWTP treated
Flow Frequency Percentage	3.22	100	0.9	100	1.1	100
Average Flow m^3/s	0.1	0.6	0.1	0.8	0.9	0.8
Maximum Flow m^3/s	0.5	1.1	1.7	1.3	0.9	1.2
Total Volume 10^6 liter	384.7	257,300.1	471.1	263,999.6	1508.9	265,124.3
Volume per year liter /year	38.5	25,730.01	47.1	26,399.9	150.9	26,512.4
KNN (15) model	**Short-term period**		**Medium-term period**		**Long-term period**	
Outfall Node	WWTP untreated	WWTP treated	WWTP untreated	WWTP treated	WWTP untreated	WWTP treated
Flow Frequency Percentage	0.9	100	2.4	100	2.5	100
Average Flow m^3/s	0.2	0.8	0.2	0.8	0.2	0.8
Maximum Flow m^3/s	0.9	1.2	0.9	1.2	0.9	1.2
Total Volume 10^6 liter	529.7	239,540.9	1,469.8	259,519.7	2106.5	270,729.9
Volume per year liter /year	52.9	23,954.1	146.98	25,951.9	210.6	27,072.9
KNN (5) model	**Short-term period**		**Medium-term period**		**Long-term period**	
Outfall Node	WWTP untreated	WWTP treated	WWTP untreated	WWTP treated	WWTP untreated	WWTP treated
Flow Frequency Percentage	0.5	100	3.6	99.9	2.5	100
Average Flow m^3/s	0.2	0.6	0.2	0.9	0.2	0.8
Maximum Flow m^3/s	0.1	1.2	1.1	1.2	0.8	1.2
Total Volume 10^6 liter	355.6	211,042.3	1469.8	270,729.9	3013.3	299,267.7
Volume per year liter /year	35.6	21,104.2	146.9	27,072.99	301.3	29,926.8
FO model	**Short-term period**		**Medium-term period**		**Long-term period**	
Outfall Node	WWTP untreated	WWTP treated	WWTP untreated	WWTP treated	WWTP untreated	WWTP treated
Flow Frequency Percentage	2.63	100	2.82	100	3.21	100
Average Flow m^3/s	0.11	0.8	0.1	0.9	0.2	0.8
Maximum Flow m^3/s	0.9	1.2	1.1	1. 2	0.9	1.2
Total Volume 10^6 liter	1,316.2	279,040.84	1,431.77	293,836.67	1,764.72	387,964.21
Volume per year liter /year	131.6	27,904.8	143.2	29,383.4	176.5	38,796.4

Table 5.9 Summary of effluent discharge at Outfall Loading under Historical and Future climate scenarios, KNN (5, 15 and 30) and FO models.

KNN (5)	**Historical period**		**Short term period**		**Medium term period**		**Long term period**	
Outfall Node	WWTP untreated	WWTP treated	WWTP untreated	WWTP treated	WWTP untreated	WWTP treated	WWTP untreated	WWTP treated
Total TP kg	18.1	20196.7	31.8	20971.3	131.5	25902.7	269.6	29738.3
Total TBOD kg	57.8	29209.2	101.6	43649.2	419.9	55994.2	860.99	61896.6
Total CBOD kg	9.2	975.7	3.4	1454.9	561.2	1866.9	21.6	2063.3
KNN (15)	**Historical period**		**Short term period**		**Medium term period**		**Long term period**	
Outfall Node	WWTP untreated	WWTP treated	WWTP untreated	WWTP treated	WWTP untreated	WWTP treated	WWTP untreated	WWTP treated
Total TP kg	3.32	22947.7	47.4	23803.2	133.5	26788.9	18843.5	26902.5
Total TBOD kg	10.49	30233.2	151.4	49543.5	425.6	53675.9	601.9	55994.2
Total CBOD kg	15.36	1007.8	5.03	1651.3	13.9	1789.4	28.32	1866.6
KNN (30)	**Historical period**		**Short term period**		**Medium term period**		**Long term period**	
Outfall Node	WWTP untreated	WWTP treated	WWTP untreated	WWTP treated	WWTP untreated	WWTP treated	WWTP untreated	WWTP treated
Total TP kg	3.85	22955.9	45.499	50545.972	54.22	57706.9	158.934	584420.2
Total TBOD kg	15.19	30208.4	145.14	66236.3	173.23	75109.7	507.6	123161.5
Total CBOD kg	1.4	1009.63	4.839	2207.96	5.78	2325.71	16.92	4105.53
FO Model	**Historical period**		**Short term period**		**Medium term period**		**Long term period**	
Outfall Node	WWTP untreated	WWTP treated	WWTP untreated	WWTP treated	WWTP untreated	WWTP treated	WWTP untreated	WWTP treated
Total TP kg	46.6	141.21	152.12	209.8	157.42	63419.73	775.58	64366.67
Total TBOD kg	9.6	517.65	485.8	1016.81	471.37	82882.59	669.85	83883.44
Total CBOD kg	10.32	184.03	16.19	338.25	15.71	2762.86	22.33	2796.21

Table 5.10 water quality changes the percentage.

Outfall Node		WWTP untreated				WWTP treated			
future climate periods	total effluent (kg)	KNN5	KNN15	KNN30	FO	KNN5	KNN15	KNN30	FO
Short term period	TP kg	57%	57%	54%	55%	39%	34%	16%	3%
	TBOD kg	57%	57%	54%	55%	25%	22%	16%	9%
	CBOD kg	0%	57%	54%	55%	25%	22%	16%	95%
Medium term period	TP kg	64%	63%	65%	53%	31%	30%	14%	13%
	TBOD kg	64%	63%	65%	57%	19%	20%	14%	13%
	CBOD kg	64%	64%	65%	57%	19%	20%	15%	13%
Long term period	TP kg	31%	0%	53%	11%	27%	30%	1%	13%
	TBOD kg	31%	44%	53%	40%	17%	19%	9%	13%
	CBOD kg	41%	31%	53%	40%	17%	19%	9%	13%

5.4 Discussion

This study confirms at the local level the increasing trend in extreme precipitation that have been reported by multiple authors and highlighted the vulnerability of the water system in the municipality. While the SWMM model has some limitations, the simulations suggest that if adaptation measures are not quickly implemented, the municipality is likely to see increased rainfall-related flooding and a deterioration of the quality of receiving water bodies. Other municipalities in the province may be in a similar or even worse situation, but only more studies like this one can tell if a particular city is at risk or not. Changes in rainfall patterns will affect the adequacy of current infrastructure to carry future flood loads and consequently adaptation-related decision making for stormwater systems should be considered. Adaptation measures that can mitigate the impacts of increased rainfall intensity may include improvements to the drainage network following the Delay-Store-Discharge principles. Measures to delay runoff (e.g., green roofs and parks) and measures to store runoff (e.g., basins, wetlands) may be combined with current and potential public spaces and urban agriculture uses. Options include a range of structural (e.g., retention and storage, protection embankments, diversion weirs, flood drainage canals, bypasses, dredging, etc.) and non-structural (early warning, resettlement, land-use zoning, etc.) risk mitigation measures. Nature-based solutions (e.g., space for the river, recovery of degraded land, increased soil infiltration, etc.) may be considered as well. Not all of these solutions are applicable to St. Catharine and not all of them are cost-effective. Possible follow-ups to this study may include a) the development of more accurate rainfall-runoff model of the study area; b) the evaluation of the benefits of various adaptation measures on combined sewers-overflow combined with a cost-benefits analysis; c) an estimation of the ecological impacts of CSO.

5.5 Conclusions

Climate change can severely affect the performance of stormwater drainage systems, especially those with combined sewer systems as the frequency and severity of overflows may worsen in the future. In this paper, a model of the urban water system of the Port Dalhousie watershed has been developed using SWMM and simulated under the current and future climate conditions. Different temporal disaggregation methods were utilized to investigate the impact of climate change on water quantity (treated and untreated wastewater volumes) and quality (total phosphorus, total biochemical oxygen demand, and carbonaceous biochemical oxygen demand). Results show that total bypass flow volume and maximum flow values gradually increase in climate periods from short to long periods. Moreover, the pollution levels have increased and are likely to increase in the future severely. These increases would lead to considerable pressure on the wastewater treatment procedures, and the municipality would establish a future expansion plan for the wastewater treatment plant.

5.6 References

Alamdari, N., & Hogue, T. S. (2022). Assessing the effects of climate change on urban watersheds: A review and call for future research. *Environmental Reviews*, *30*(1), 61–71.

Alamdari, N., Sample, D., Steinberg, P., Ross, A., & Easton, Z. (2017). Assessing the Effects of Climate Change on Water Quantity and Quality in an Urban Watershed Using a Calibrated Stormwater Model. *Water*, *9*(7), 464.

Andimuthu, R., Kandasamy, P., Mudgal, B. V., Jeganathan, A., Balu, A., & Sankar, G. (2019). Performance of urban storm drainage network under changing climate scenarios: Flood mitigation in Indian coastal city. *Scientific Reports*, *9*(1), 7783.

Bach, P. M., Deletic, A., Urich, C., Sitzenfrei, R., Kleidorfer, M., Rauch, W., & McCarthy, D. T. (2013). Modelling Interactions Between Lot-Scale Decentralised Water Infrastructure and Urban Form – a Case Study on Infiltration Systems. *Water Resources Management*, *27*(14), 4845–4863.

Barco Janet, Wong Kenneth M., & Stenstrom Michael K. (2008a). Automatic Calibration of the U.S. EPA SWMM Model for a Large Urban Catchment. *Journal of Hydraulic Engineering*, *134*(4), 466–474.

Barco Janet, Wong Kenneth M., & Stenstrom Michael K. (2008b). Automatic Calibration of the U.S. EPA SWMM Model for a Large Urban Catchment. *Journal of Hydraulic Engineering*, *134*(4), 466–474.

Bhaduri Budhendra, Minner Marie, Tatalovich Susan, & Harbor Jon. (2001). Long-Term Hydrologic Impact of Urbanization: A Tale of Two Models. *Journal of Water Resources Planning and Management*, *127*(1), 13–19.

Burge, K., Browne, D., Breen, P., & Wingad, J. (2012). Water sensitive urban design in a changing climate: Estimating the performance of WSUD treatment measures under various climate change scenarios. 119–126.

Chen, J., Brissette, F. P., Chaumont, D., & Braun, M. (2013). Finding appropriate bias correction methods in downscaling precipitation for hydrologic impact studies over North America. *Water Resources Research*, *49*(7), 4187–4205.

Decent, D., & Blair, F. (2018). DANA DECENT AND DR. BLAIR FELTMATE | INTACT CENTRE ON CLIMATE ADAPTATION | JUNE 2018. https://www.preventionweb.net/publication/after-flood-impact-climate-change-mental-health-and-lost-time-work

Erickson, A. J., Weiss, P. T., & Gulliver, J. S. (2013). Optimizing Stormwater Treatment Practices. Springer New York.

Fortier Claudine & Mailhot Alain. (2015). Climate Change Impact on Combined Sewer Overflows. *Journal of Water Resources Planning and Management*, *141*(5), 04014073.

Hatt, B. E., Fletcher, T. D., Walsh, C. J., & Taylor, S. L. (2004). The Influence of Urban Density and Drainage Infrastructure on the Concentrations and Loads of Pollutants in Small Streams. *Environmental Management*, *34*(1), 112–124.

Hussain, S. N., Zwain, H. M., & Nile, B. K. (2021). Modeling the effects of land-use and climate change on the performance of stormwater sewer system using SWMM simulation: Case study. *Journal of Water and Climate Change*, *13*(1), 125–138.

Kändler, N., Annus, I., Vassiljev, A., & Puust, R. (2020). Peak flow reduction from small catchments using smart inlets. *Urban Water Journal*, *17*(7), 577–586.

Kaushal, S. S., & Belt, K. T. (2012). The urban watershed continuum: Evolving spatial and temporal dimensions. *Urban Ecosystems*, *15*(2), 409–435.

Krieger, K., Kuchenbecker, A., Hüffmeyer, N., & Verworn, H.-R. (2013). Local effects of global climate change on the urban drainage system of Hamburg. *Water Science and Technology*, *68*(5), 1107–1113.

Luan, Q., Fu, X., Song, C., Wang, H., Liu, J., & Wang, Y. (2017). Runoff Effect Evaluation of LID through SWMM in Typical Mountainous, Low-Lying Urban Areas: A Case Study in China. *Water*, *9*(6), 439.

Menzel, L., & Bürger, G. (2002). Climate change scenarios and runoff response in the Mulde catchment (Southern Elbe, Germany). *Journal of Hydrology*, *267*(1–2), 53–64.

Moghadas Shahab, Leonhardt Günther, Marsalek Jiri, & Viklander Maria. (2018). Modeling Urban Runoff from Rain-on-Snow Events with the U.S. EPA SWMM Model for Current and Future Climate Scenarios. *Journal of Cold Regions Engineering*, *32*(1), 04017021.

Moglen Glenn E. & Rios Vidal Geil E. (2014). Climate Change and Storm Water Infrastructure in the Mid-Atlantic Region: Design Mismatch Coming? *Journal of Hydrologic Engineering*, *19*(11), 04014026.

Mohammed, M. H., Zwain, H. M., & Hassan, W. H. (2021). Modeling the impacts of climate change and flooding on sanitary sewage system using SWMM simulation: A case study. *Results in Engineering*, *12*, 100307.

Niagara Falls Water Treatment Plant—2021 Annual Water Quality Report—Niagara Region, Ontario. (n.d.). Retrieved March 14, 2023, from https://www.niagararegion.ca/living/water/water-quality-reports/niagarafalls/annual-report-2021.aspx

O'Hara, J. K., & Georgakakos, K. P. (2008). Quantifying the Urban Water Supply Impacts of Climate Change. *Water Resources Management*, *22*(10), 1477–1497.

Patel, H. D., Jain, G. V., & Shah, S. D. (2023). Urban flood vulnerability assessment of Vadodara city using rainfall–run-off simula-tions. *Current Science*, *124*(1), 79.

Semadeni-Davies, A., Hernebring, C., Svensson, G., & Gustafsson, L.-G. (2008). The impacts of climate change and urbanisation on drainage in Helsingborg, Sweden: Suburban stormwater. *Journal of Hydrology*, *350*(1), 114–125.

Sharma, A., Pezzaniti, D., Myers, B., Cook, S., Tjandraatmadja, G., Chacko, P., Chavoshi, S., Kemp, D., Leonard, R., Koth, B., & Walton, A. (2016). Water Sensitive Urban Design: An Investigation of Current Systems, Implementation Drivers, Community Perceptions and Potential to Supplement Urban Water Services. *Water*, *8*(7), 272.

Tavakol-Davani, H. (2016). *Watershed-scale life cycle assessment of rainwater harvesting systems to control combined sewer overflows*.

Wang, M., Zhang, D. Q., Su, J., Trzcinski, A. P., Dong, J. W., & Tan, S. K. (2017). Future Scenarios Modeling of Urban Stormwater Management Response to Impacts of Climate Change and Urbanization. *CLEAN – Soil, Air, Water*, *45*(10), 1700111.

Warwick J. J. & Tadepalli P. (1991). Efficacy of SWMM Application. *Journal of Water Resources Planning and Management*, *117*(3), 352–366.

Water Environment Association of Ontario. (n.d.). Retrieved March 14, 2023, from https://weao.org/

Wey, K. M. (2006). Temporal Disaggregation of Daily Precipitation Data in a Changing Climate. 178.

Zahmatkesh Zahra, Karamouz Mohammad, Goharian Erfan, & Burian Steven J. (2015). Analysis of the Effects of Climate Change on Urban Storm Water Runoff Using Statistically Downscaled Precipitation Data and a Change Factor Approach. *Journal of Hydrologic Engineering*, *20*(7), 05014022.

Zhang, K., Manuelpillai, D., Raut, B., Deletic, A., & Bach, P. M. (2019). Evaluating the reliability of stormwater treatment systems under various future climate conditions. *Journal of Hydrology*, *568*, 57–66.

Chapter 6

Conclusions and Recommendations

6.1 Conclusions

Adaptation to climate change has a high priority for Canada, and any failure to take that into account can cost Canadians their safety and economic prosperity. An essential input to adaptation decisions is an accurate estimation of how the risk and performance of vital infrastructure will change in the future. This thesis focuses on urban water systems, for which risk and performance are estimated using IDF curves or sub-daily precipitation time series. Three critical contributions to knowledge were made, each in the form of a scientific paper.

In the first paper, the accuracy of the two IDF generation algorithms used in the web-based IDF_CC tool (EQMo and QDMo) was assessed and areas for improvement were identified. A critical flaw was found in the EQMo method, which prevents it from accurately accounting for changes in the climate change signal. The performance of the EQMo, QDMo, EQMm, and QDMm was assessed by testing the similarity of the annual maxima generated by each method in the historical periods. The four methods were applied to four stations in Eastern Ontario, and the results were compared for the historical period (1976 –2006), the short-term (2011–2040), the medium-term (2041–2070), and the long-term (2071–2100). The best method was the QDMm, while the QDMo fared poorly regarding the similarity of distributions and the EQMo could not capture the climate change signal. It was also shown that the modified versions (EQMm and QDMm) are more consistent with each other in future periods compared to the original versions. These findings should be beneficial for incorporating projected changes in derived climate information (IDF curves) as the basis for planning, design, and management in various water engineering applications.

In the second paper, the impact of the choice of the temporal disaggregation technique (used to convert projected daily precipitation time series into sub-daily precipitation time series was assessed). Temporal disaggregation techniques have different levels of complexity and unequal performances, and the generated time series may not have the same statistical characteristics. A simple steady-state stochastic disaggregation model that generates wet/dry day occurrence using a binomial distribution and precipitation intensity using an exponential distribution is proposed and compared to widely used temporal disaggregation methods: the multiplicative random cascade model (MRC), the Hurst-Kolmogorov process (HKP), and three versions of the K-nearest neighbour model (KNN) using the nonparametric KS test. Daily time series of future precipitation is generated by temporally downscaling the outputs of four RCMs using the quantile mapping (QM) method. The annual maximum time series generated using MRC systematically failed the KS test comparing them to observations, while HKP had low (20% to 70%) acceptance rates. FO and KNN (30) had acceptance rates close to 100%, and led to the most realistic annual maximum time series at subdaily and IDF curves, suggesting that complexity does not necessarily yield the best results.. This study highlights the importance of carefully selecting the method used to generate future IDF curves, as two different methods can yield wildly different results. The future resilience of urban infrastructure, public safety, and global economic prosperity are at stake, and the blind use of a particular method can lead to maladaptation and costly infrastructure failure.

In the third paper, the performance of the Port-Dalhousie sewer system and treatment plant under a changing climate is examined in this chapter using a SWMM (Stormwater Management Model) model. The model was forced with downscaled and temporally disaggregated precipitation outputs of the Canadian Regional Climate Model at the Port Dalhousie station, simulated under emission scenario RCP8.5. The temporal disaggregation was done using the Fahad-Ousmane and the KNN (30) methods developed in the previous chapter. The impact of climate change on the frequency, volume, and quality of combined sewer overflows and other hydraulic parameters is examined. Results show that total bypass flow volume and maximum flow values gradually increase in climate periods such as historical, short, medium, and long. Moreover, the increased pollution levels will likely severely increase in the future. This increase would lead to considerable pressure on the wastewater treatment procedures, and the municipality would establish a future expansion plan for the wastewater treatment plant.

In summary, the following are the main highlights of the thesis:

- Considering the potential implications of changing extreme precipitation patterns, all results generated using the original algorithms used IDF-CC tool should be interpreted with caution.
- The resilience of urban infrastructure in a changing climate is at stake and the blind use of a particular temporal disaggregation method can lead to maladaptation and costly infrastructure failure.

- Water quantity and quality in stormwater drainage systems under climate change may cause considerable pressure on the current wastewater treatment procedures and a better understanding of such changes is warranted.

6.2 Recommendations

While the above results are essential in terms of methodology and knowledge about the study area, several recommendations can be great value. The obtained results are site-dependent and hence cannot be arbitrary generalized. Therefore, potential future work would involve a Canadian (or even global) study where more locations preferably with different climate regimes and more temporal disaggregation techniques would be analyzed, and maybe geographical patterns could be found. Another potential avenue for future work would be developing a better rainfall-runoff model (with the exact information of pipe slopes) and simulation of climate change adaptation strategies to support the decision-making process, particularly for professionals, engineers, and stakeholders. Finally, this study is based on climate change scenarios developed for the 5th IPCC report, and the results could be updated to reflect the recently-released models used in the 6th phase.

Appendix A

Assessment and Improvement of IDF Generation Algorithms Used in the IDF_CC Tool

A1.1 Suppelmentary Materials

Section 1. Case study and data availability

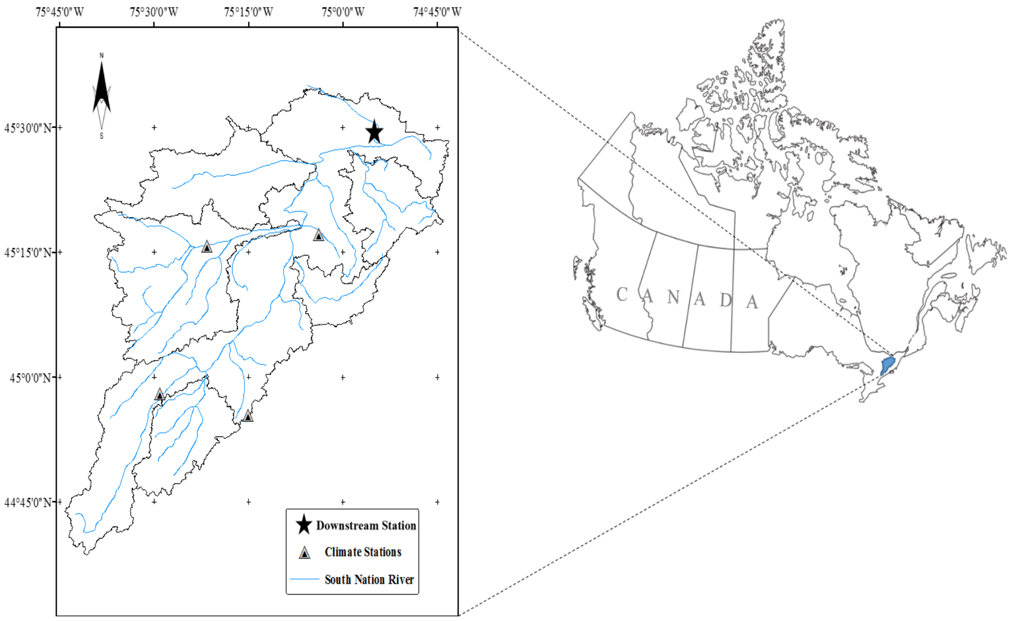

Figure A1. The meteorological stations in the South Nation watershed (Alodah and Seidou 2019).

Table A1. Weather stations used.

Station name	Climate Identifier	Latitude (N)	Longitude (W)	Elevation (m)	Daily Precipitation (mm)	
					Mean	Standard Deviation
St. Albert	6107276	45° 17' 14"	75° 03' 49"	80	2.77	6.06
South Mountain	6107955	44° 58' 00"	75° 29' 00"	84.7	2.64	6.07
Morrisburg	6105460	44° 55' 25"	75° 11' 18"	81.7	2.77	6.17
Russell	6107247	45° 15' 46"	75° 21' 34"	76.2	2.63	5.97

- **Climate change models**

Sub-daily data was extracted from four regional climate models (RCMs), part of the North American domain of the Coordinated Regional Climate Downscaling Experiment (NA-CORDEX), according to the Coupled Model Inter-comparison Project Phase 5 (CMIP5) experiment, and utilized to examine the developed algorithms (Table 2). The horizontal resolution was NAM-44 (0.44^{o}) which corresponds to roughly 50 km. Comparisons were conducted for the future period, which includes the short- (2011-2039), medium- (2041-2069), and long-term (2071-2100) periods.

Table A2. List of regional climate models used in the study with two AR5 scenarios RCP4.5 and RCP8.5: the Canadian Regional Climate Model (CanRCM4), the Danish Climate Centre model (HIRHAM5), the Rossby Centre Regional Atmospheric Climate Model (RCA4), and the Regional Climate Model (RegCM4.3).

Global Circulation Model (GCM)	Regional Climate Model (RCM)	Spatial Resolution	(RCPs)		Variables
CanESM2	CanRCM4	44i	RCP 8.5		Precipitation (pr) of different durations (1h, 2h, 3h,…, 24h)
EC-EARTH	HIRHAM5	44i	RCP 4.5	RCP 8.5	
	RCA4	44i	RCP 4.5	RCP 8.5	
GFDL	RegCM4	44i	RCP 8.5		
	WRF	44i	RCP 8.5		
MPI-ESM-LR	RegCM4	44i	RCP 8.5		
	WRF	44i	RCP 8.5		
Met Office Hadley Centre (HadGEM2-ES)	RegCM4	44i	RCP 8.5		
	WRF	44i	RCP 8.5		

Section 2. EQM and QDM algorithms

Part 1: Original IDF_CC algorithms

2.1 The equidistant quantile mapping (EQM) algorithm

The original EQM algorithm (Srivastav *et al.,* 2014) was used in ICF_CC versions up to 3.5 and consists of the following steps:

1. Extract the daily maximum precipitation of the historical run from GCM model

$$X_{max}^{GCM}=\begin{bmatrix} X_{1,max}^{GCM} \\ X_{2,max}^{GCM} \\ X_{3,max}^{GCM} \\ \vdots \\ X_{N,max}^{GCM} \end{bmatrix} \quad \text{(S1)}$$

for years 1 through *N*.

2. Extract the annual maximum sub-daily precipitation, $X_{i,max}^{STN,j}$, at location *STN*, duration *j* (*j*= 1, 2, 6, 12, or 24 h), and year *i,* using

$$X_{max}^{STN}=\begin{bmatrix} X_{1,max}^{STN,1hr} & X_{1,max}^{STN,2hr} & \cdots & X_{1,max}^{STN,24hr} \\ X_{2,max}^{STN,1hr} & X_{2,max}^{STN,2hr} & \cdots & X_{2,max}^{STN,24hr} \\ X_{3,max}^{STN,1hr} & X_{3,max}^{STN,2hr} & \cdots & X_{3,max}^{STN,24hr} \\ \vdots & \vdots & \vdots & \vdots \\ X_{i,max}^{STN,1hr} & X_{i,max}^{STN,2hr} & \cdots & X_{i,max}^{STN,24hr} \end{bmatrix} \quad \text{(S2)}$$

3. Extract the daily maximum precipitation from RCP 4.5 and 8.5 scenarios for the selected GCM models.

$$X_{max}^{GCM,fut}=\begin{bmatrix} X_{1,max}^{GCM,RCP45} & X_{1,max}^{GCM,RCP85} \\ X_{2,max}^{GCM,RCP45} & X_{2,max}^{GCM,RCP85} \\ X_{3,max}^{GCM,RCP45} & X_{3,max}^{GCM,RCP85} \\ \vdots & \vdots \\ X_{N_F,max}^{GCM,RCP45} & X_{N_F,max}^{GCM,RCP85} \end{bmatrix} \quad \text{(S3)}$$

where $X_{max}^{GCM,fut}$ is the selected GCM data series of the future scenario period; N_F is the total number of years of the future period.

4. Fit a probability distribution to $X_{i,max}^{GCM}$, X_{max}^{STN}, and $X_{max}^{GCM,fut}$. The probability distribution should fit each annual maximum precipitation for the different durations at each station. Therefore, an EV type 1 distribution fits all data extracted from the different models as recommended by Environment Canada.

5. Following the quantile mapping approach, a statistical relationship between annual GCM maximum and observed maximum sub-daily precipitation is established to derive the GCM sub-daily series $Y_{max,j}^{GCM}$, i.e., the GCM data is spatially downscaled to the observed sub-daily maxima. By obtaining the cumulative density function CDF of the GCM daily maximum, including the baseline period and observed sub-daily maxima, and then inverting them, the statistically downscaled $Y_{max,j}^{GCM}$ is obtained for duration *j* from:

$$Y_{max,j}^{STN}=CDF((invCDF(\frac{X_{max}^{GCM}}{\theta^{GCM}}))/\theta^{STN,j}) \quad \text{(S4)}$$

where θ is the parameter of the fitted distribution.

6. GCM future data can be temporally downscaled to control daily maximum by establishing a statistical relationship similar to quantile-mapping, thereby modelling the changes between the control and future GCM maxima. The following equation shows the temporal downscaling from projected data:

$$Y_{max}^{GCM,Fut}=CDF((invCDF(\frac{X_{max}^{GCM}}{\theta^{GCM}}))/\theta^{GCM,Fut}) \quad \text{(S5)}$$

where $Y_{max}^{GCM,Fut}$ is the output of the linear relation function. This is called quantile matching between the control and the future periods.

7. Find the proper relationship between $Y_{max,j}^{STN}$ and X_{max}^{GCM}. The linear relationship is suitable in most cases (see Piani *et al.*, 2010), hence the linear equation becomes:

$$Y^{STN}_{max,j}=f(X^{GCM}_{max}) \tag{S6}$$

$$Y^{STN}_{max,j}=a_1 \times X^{GCM}_{max} + b_1 \tag{S7}$$

8. Similarly to Step 7, we apply the following linear equations:

$$Y^{GCM,Fut}_{max}=f(X^{GCM}_{max}) \tag{S8}$$

$$Y^{GCM,Fut}_{max}=a_2 \times X^{GCM}_{max} + b_2 \tag{S9}$$

9. Generate the future maximum sub-daily data. Combine the linear equations from Steps 7 and 8 by substituting X^{GCM}_{max} by $X^{GCM,Fut}_{max}$

$$X^{STN,Fut}_{max,j}=a_1 \times \left[\frac{X^{GCM,Fut}_{max}-b_2}{a_2}\right] + b_1 \tag{S10}$$

The final step is to generate IDF values and plot them for each station, return period, and event duration (see below).

Part 2: The quantile delta mapping (QDM) algorithm

The quantile delta mapping (QDM) algorithm (Schardong *et al.*, 2020) is used in the latest version of the IDF_CC tool to temporally downscale precipitation data. The method uses the Generalized extreme value (GEV) to estimate the quantile of both periods. The following notation is used below: x denotes the annual maximum precipitation, j the sub-daily durations (1, 2, 6, 12, or 24h), o the *in situ* data, h the historical simulation data, m the model (downscaled GCM), f the future projection data, F the cumulative density function (CDF) of the fitted GEV distribution, and F^{-1} the inverse CDF. The following procedure is used:

1. Extract $x_{j,o,h}$
2. Extract $x_{m,h}$ from a given GCM.
3. Fit the GEV distribution to each extracted time series to obtain $F_{j,o,h}$ and $F_{m,h}$.
4. Generate random numbers between 0 and 1 to represent the non-occurrence probability (see Hassanzadeh *et al.,* 2014). A statistical relationship is then established based on the quantiles extracted from the GEV fit to each pair $F_{j,o,h}$ and $F_{m,h}$ using the following equation:

$$\hat{x}_{j,o,h}=\frac{a_j+x_{m,h}}{b_j+c_j x_{m,h}}+\frac{d_j}{x_{m,h}} \tag{S11}$$

   where $\hat{x}_{j,o,h}$ corresponds to the annual maximum precipitation (AMP) quantiles at the station scale, and a_j, b_j, c_j, and d_j are the adjusted coefficients which are determined through a differential evolution (DE) optimization algorithm.
5. Daily maxima from the RCP 4.5 and 8.5 scenarios, $x_{m,f}$, are extracted.
6. The GEV probability distribution is fitted to $x_{m,f}$ for each future scenario to yield $F_{m,f}$.
7. The non-occurrence probability, $\tau_{m,f}$, is calculated for $F_{m,f}$. Then, the corresponding quantile ($\hat{x}_{m,h}$) at the GCM control period is estimated by entering the value of $\tau_{m,f}$ in the inverse CDF to yield $F^{-1}{}_{m,h}$. This scaling step

is used to integrate the future projections in the projected IDF and applies basic concepts of quantile delta mapping. The relative change, Δ_m, is estimated using Equation (S14):

$$\tau_{m,f}=F_{m,f}(x_{m,f}) \tag{S12}$$

$$\hat{x}_{m,h}=F^{-1}_{m,h}(\tau_{m,f}) \tag{S13}$$

$$\Delta_m=\frac{x_{m,f}}{\hat{x}_{m,h}} \tag{S14}$$

8. Step 1 is applied again by replacing $x_{m,h}$ with $\hat{x}_{m,h}$ and multiplying by Δ_m to construct the updated future maximum sub-daily series at the station level:

$$x^{f}_{j,o,h}=\Delta_m.\ \hat{x}_{j,o,h} \tag{S15}$$

9. Finally, IDF curves are constructed for the future sub-daily data and compared with the historical observed IDF curves to detect projected changes in intensities.

Section 3. Flaws in QDM

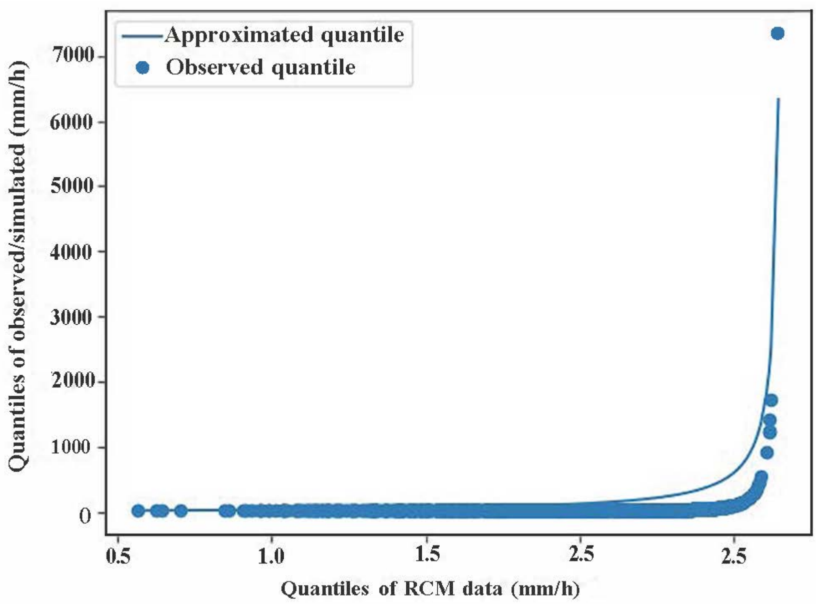

Figure A2. Unsuccessful fit of equation (S11) using quantiles of precipitation simulated with EC-EARTH.HIRAM5, RCP 8.5, and quantiles of observation.

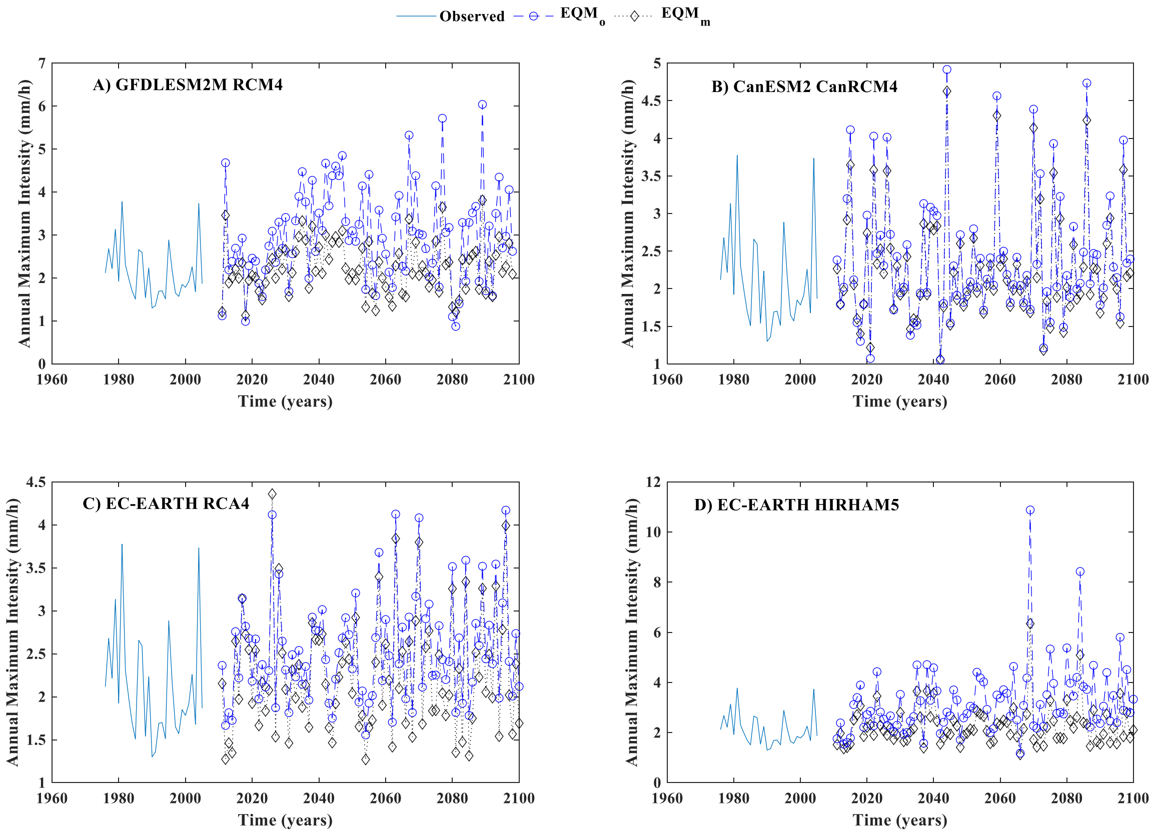

Figure A3. Differences between EQM_o and EQM_m at Russell station for the 24h precipitation datasets using different climate models forced with scenario RCP 8.5: A) GFDLESM2M RCM4, B) CanESM2 CanRCM4, C) EC-EARTH RCA4, and D) EC-EARTH HIRHAM5.

Section 4. Model evaluation

Table A3. Percentage of non-dissimilarity between downscaled annual maxima for each station and period.

Period	Method	Morrisburg				Russell				South Mountain				St. Albert			
		EQM_m	**QDM_m**	**EQM_o**	**QDM_o**	**EQM_m**	**QDM_m**	**EQM_o**	**QDM_o**	**EQM_m**	**QDM_m**	**EQM_o**	**QDM_o**	**EQM_m**	**QDM_m**	**EQM_o**	**QDM_o**
Calibration	EQM_m	100%	100%	100%	**0%**	100%	100%	100%	100%	100%	100%	100%	100%	100%	100%	100%	100%
	QDM_m	100%	100%	100%	**0%**	100%	100%	100%	100%	100%	100%	100%	100%	100%	100%	100%	100%
	EQM_o	100%	100%	100%	**0%**	100%	100%	100%	100%	100%	100%	100%	100%	100%	100%	100%	100%
	QDM_o	**0%**	**0%**	**0%**	100%	100%	100%	100%	100%	100%	100%	100%	100%	100%	100%	100%	100%
Validation	EQM_m	100%	100%	100%	**0%**	100%	100%	100%	100%	100%	100%	100%	100%	100%	100%	100%	100%
	QDM_m	100%	100%	100%	**0%**	100%	100%	100%	100%	100%	100%	100%	100%	100%	100%	100%	100%
	EQM_o	100%	100%	100%	**0%**	100%	100%	100%	100%	100%	100%	100%	100%	100%	100%	100%	100%
	QDM_o	**0%**	**0%**	**0%**	100%	100%	100%	100%	100%	100%	100%	100%	100%	100%	100%	100%	100%
Short term	EQM_m	100%	100%	100%	**0%**	100%	100%	100%	**0%**	100%	100%	100%	100%	100%	100%	100%	100%
	QDM_m	100%	100%	100%	**0%**	100%	100%	100%	100%	100%	100%	100%	100%	100%	100%	100%	100%
	EQM_o	100%	100%	100%	**0%**	100%	100%	100%	**0%**	100%	100%	100%	100%	100%	100%	100%	100%
	QDM_o	**0%**	**0%**	**0%**	100%	**0%**	100%	**0%**	100%	100%	100%	100%	100%	100%	100%	100%	100%
Medium term	EQM_m	100%	100%	**0%**	**0%**	100%	100%	100%	**0%**	100%	100%	100%	100%	100%	100%	100%	100%
	QDM_m	100%	100%	**0%**	**0%**	100%	100%	100%	**0%**	100%	100%	100%	100%	100%	100%	100%	100%
	EQM_o	**0%**	**0%**	100%	**0%**	100%	100%	100%	**0%**	100%	100%	100%	100%	100%	100%	100%	100%
	QDM_o	**0%**	**0%**	**0%**	100%	**0%**	**0%**	**0%**	100%	100%	100%	100%	100%	100%	100%	100%	100%
Long term	EQM_m	100%	100%	**0%**	**0%**	100%	100%	**0%**	**0%**	100%	100%	**0%**	100%	100%	100%	**0%**	100%
	QDM_m	100%	100%	**0%**	**0%**	100%	100%	100%	**0%**	100%	100%	**0%**	100%	100%	100%	100%	100%
	EQM_o	**0%**	**0%**	100%	**0%**	**0%**	100%	100%	**0%**	**0%**	**0%**	100%	**0%**	**0%**	100%	100%	**0%**
	QDM_o	**0%**	**0%**	**0%**	100%	**0%**	**0%**	**0%**	100%	100%	100%	**0%**	100%	100%	100%	**0%**	100%

Section 5. Comparing IDF curves obtained with different methods

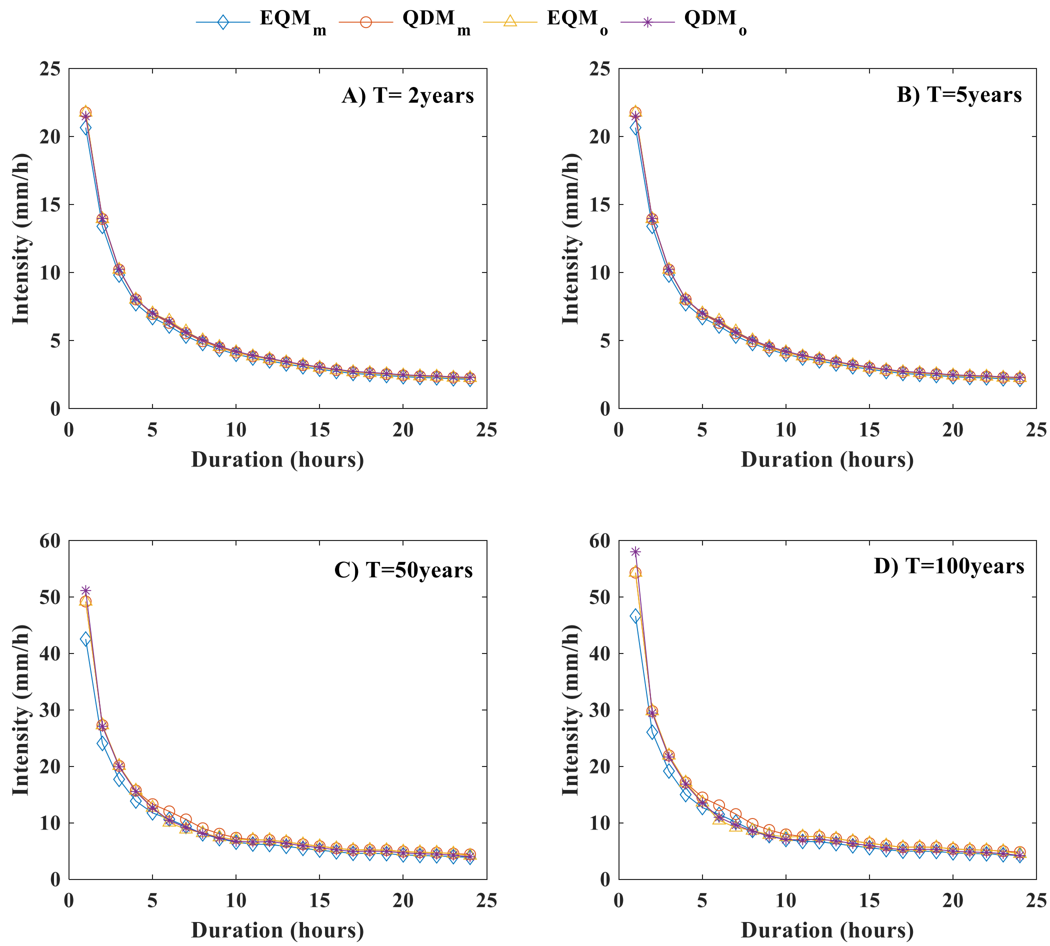

Figure A4. IDF curves generated for the period 2011-2040 at Russel station using model CanESM2 RCP8.5 and return periods of A) T=2years, B) T=5 years, C) T=50years, and D) T=100years.

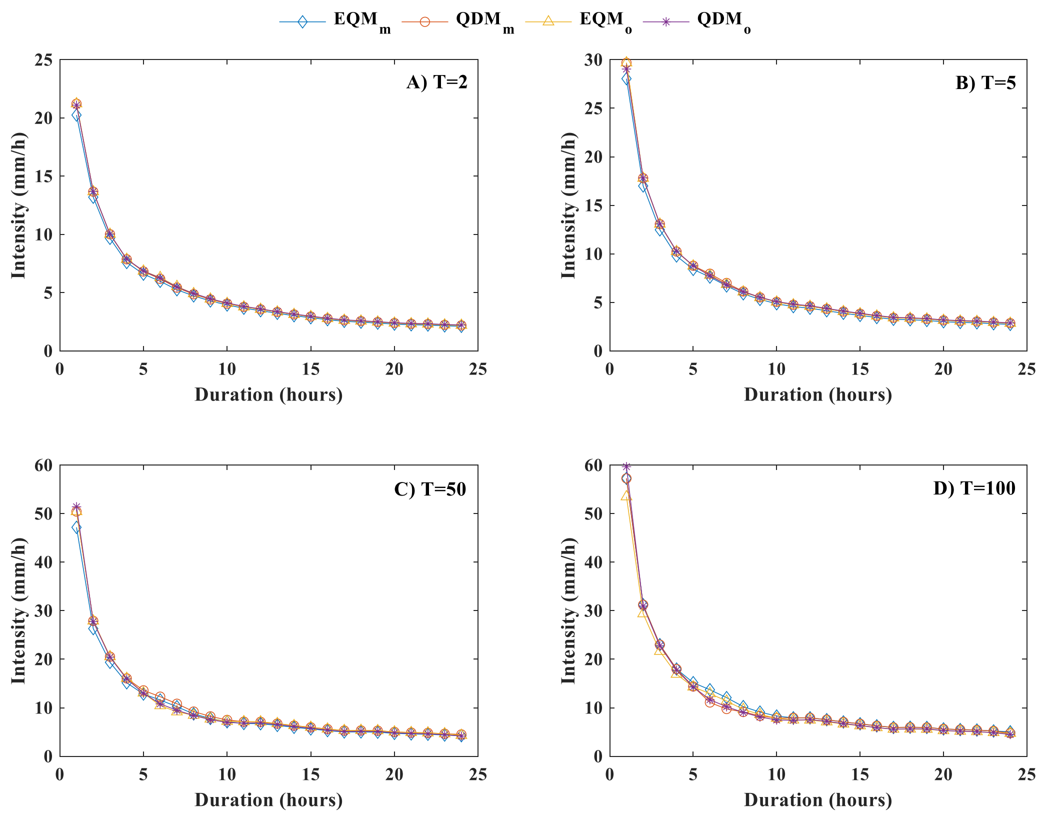

Figure A5. IDF curves generated for the period 2041-2070 at Russel station using model CanESM2 RCP8.5 and return periods of A) T=2years, B) T=5years, C) T=50years, and D) T=100years.

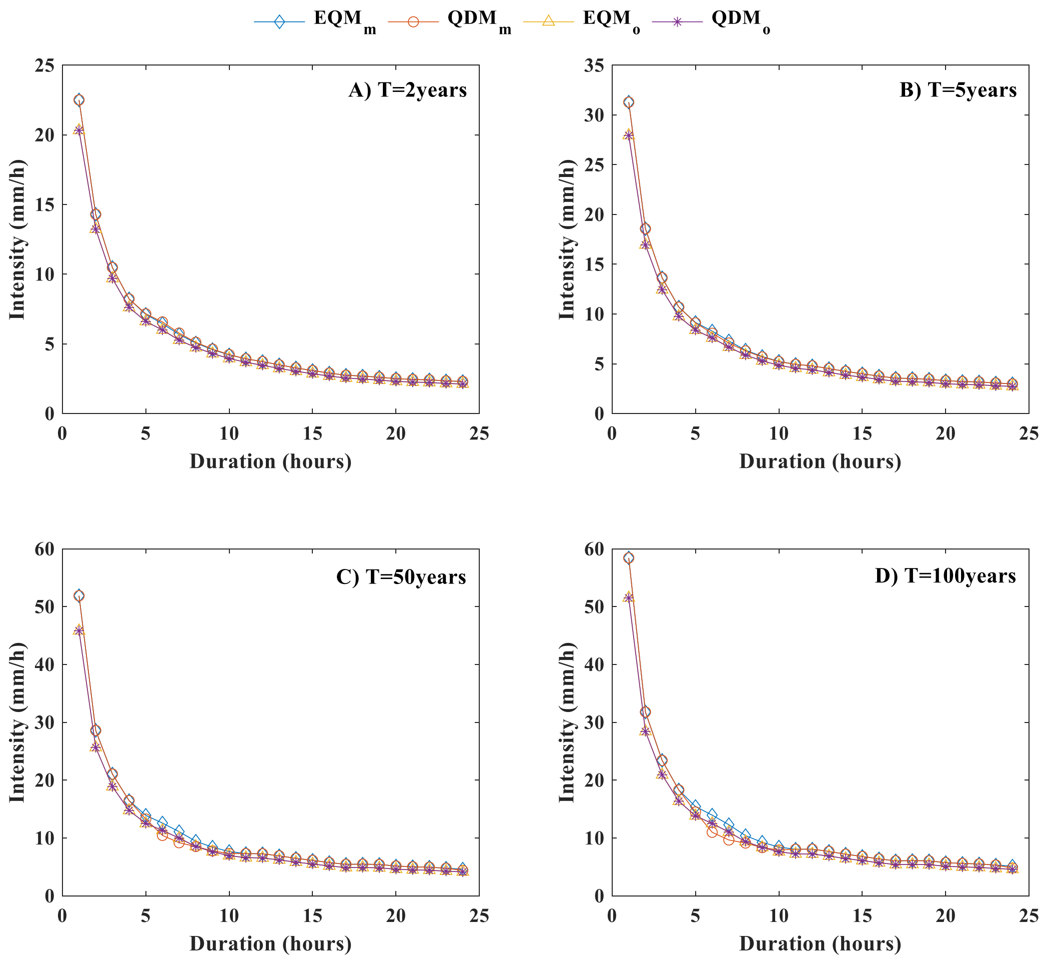

Figure A6. Comparison of IDF curve generation for the period 2071-2100 for Russel station using model CanESM2 RCP8.5 and return periods (T) of A) T=2years, B) T=5years, C) T=50years, and D) T=100years.

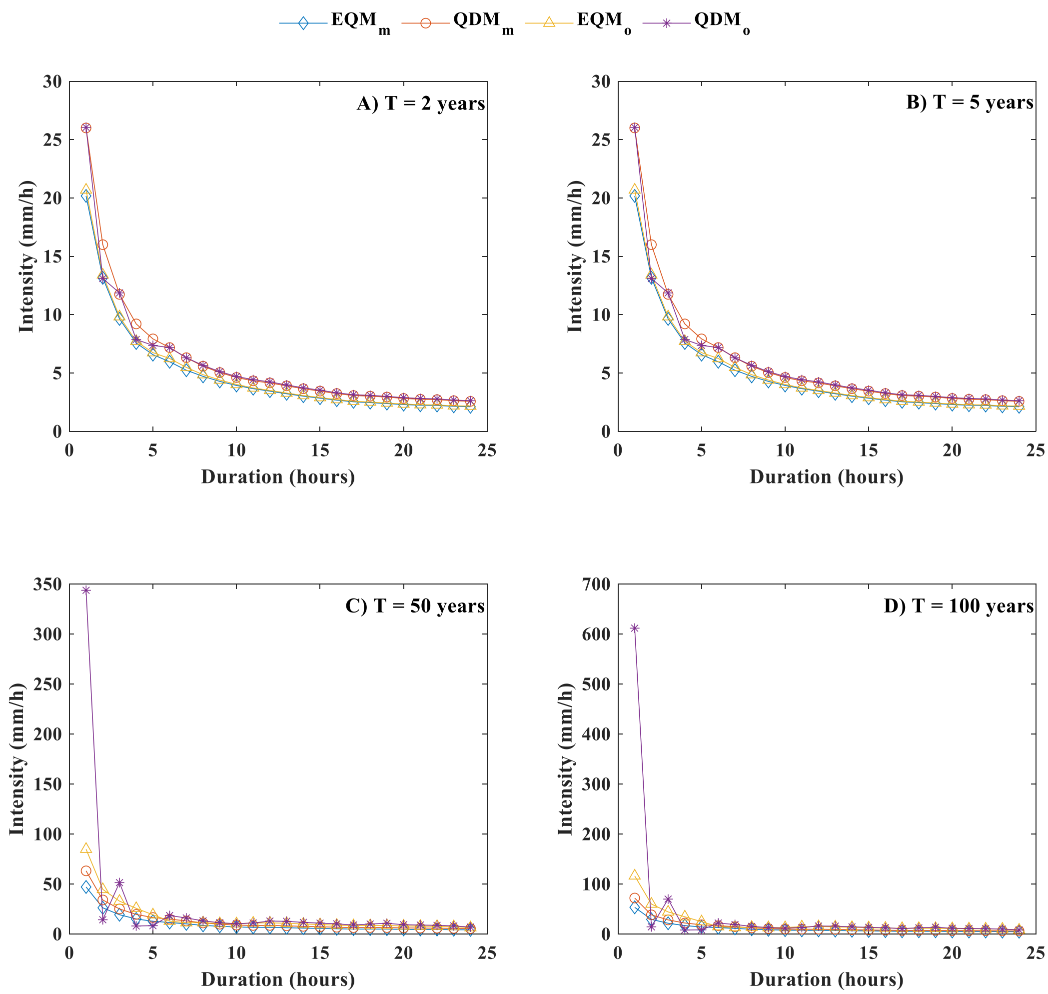

Figure A7. IDF curves generated for the period 2011-2040 at Russel station using model EC-EARTH HIRHAM 5 RCP8.5 and return periods of A) T=2years, B) T=5years, C) T=50years, and D) T=100years.

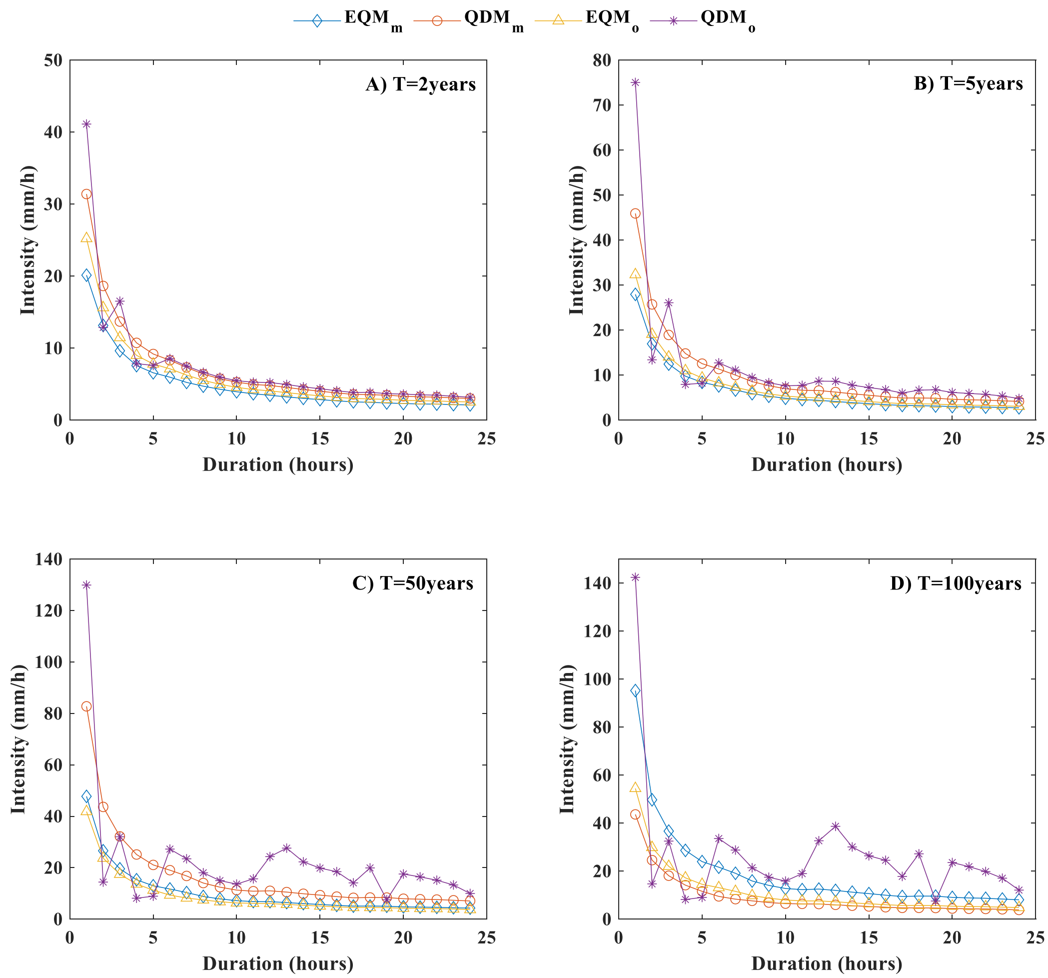

Figure A8. IDF curves generated for the period 2041-2070 at Russel station using model ECEARTH HIRHAM 5 RCP8.5 and return periods of A) T=2 years, B) T=5 years, C) T=50 years, and D) T=100 years.

References

Alodah, A.; Seidou, O. Assessment of Climate Change Impacts on Extreme High and Low Flows: An Improved Bottom-Up Ap-proach. Water 2019, 11 (6).

Srivastav, R. K.; Schardong, A.; Simonovic, S. P. Equidistance Quantile Matching Method for Updating IDF Curves under Climate Change. Water Resources Management 2014, 28 (9), 2539–2562.

Schardong, A.; Simonovic, S. P.; Gaur, A.; Sandink, D. Web-Based Tool for the Development of Intensity Duration Frequency Curves under Changing Climate at Gauged and Ungauged Locations. Water 2020, 12 (5).

Hassanzadeh, E., Nazemi, A., & Elshorbagy, A. Quantile-based downscaling of precipitation using genetic programming: Application to IDF curves in Saskatoon. Journal of Hydrologic Engineering, 2014, 19(5), 943-955.

Appendix B

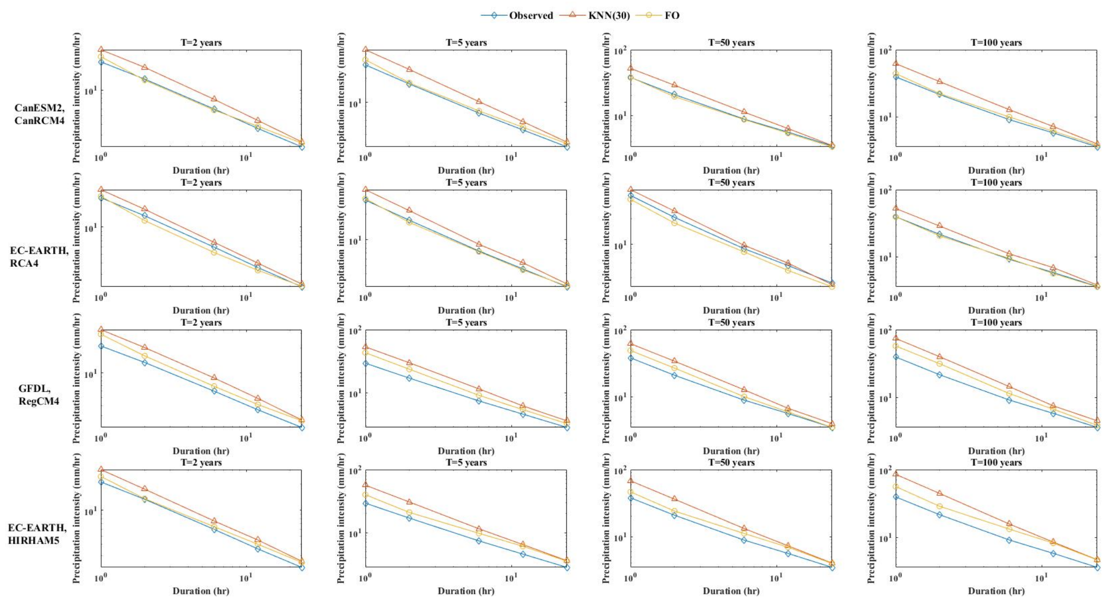

Figure B1. IDF of Russel Station curves resulting from KNN30 and FO disaggregation methods, short period (all climate change models); for different return periods T=2, 5, 50 and 100 years.

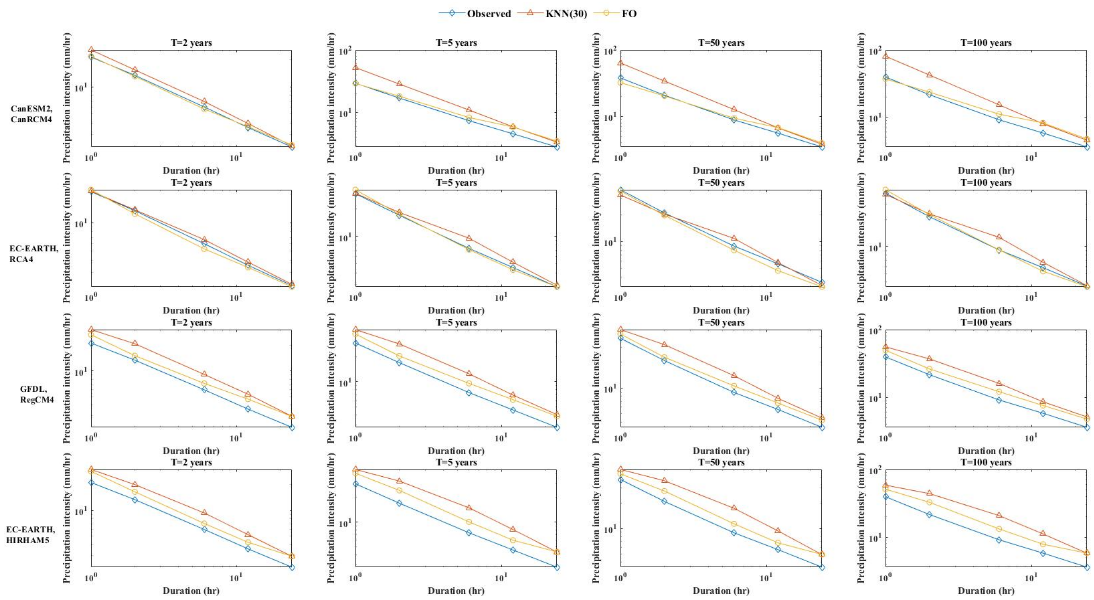

Figure B2. IDF of Russel Station curves resulting from KNN30 and FO all disaggregation methods, medium period (all climate change models); for different return periods T=2, 5, 50 and 100 years.